The Chemical Heterogeneity of Lower Crustal Xenoliths from the Hualalai 1800 Kaupulehu flow

By Camille Adele Rose Lecoeuche

Under the supervision of Johan Lissenberg, Matthew Gleeson and Marc-Alban Millet

For the award of MPhil

September 2022

Abstract

Historically, geochemists have studied radiogenic isotope signatures of mantle-derived basalts, like erupted ocean island basalts (OIBs) or mid-ocean ridge basalts (MORBs), to analyse mantle composition and heterogeneity. Lambart et al.'s (2019) study of the heterogeneity of the depleted upper mantle, found that the isotopic composition of minerals of lower crustal cumulates preserved significantly greater heterogeneity than locally erupted MORBs. Hence the lavas underestimated the true heterogeneity of the original upper mantle source. This project applies Lambart et al.'s (2019) approach to study the heterogeneity of the mantle plume beneath Hualalai, Hawaii. The major element, trace element and isotopic data of lower crustal xenoliths brought to the surface by the 1800 Hualalai eruption were analysed to test whether Hawaiian lower crustal cumulates reveal greater chemical heterogeneity than their corresponding lavas.

These samples record primary sample- and crystal-scale compositional variation, revealing greater trace element and isotopic heterogeneity than corresponding basaltic lavas. In line with the theory of Lambart et al. (2019) for cumulates from mid-ocean ridge (MOR) settings, it is hypothesised that this greater heterogeneity is expressed in lower crustal Hawaiian cumulates because the melts from which they formed experience less magma mixing and homogenisation of trace element and isotopic signatures than corresponding lavas. This implies that homogenisation from magma mixing in the crust occurs at both MOR and OIB settings – at least under Hualalai. As a result, new data suggests that previous studies on the Hawaiian mantle plume beneath Hualalai, based on basaltic lavas, may have underestimated its true heterogeneity. These findings, however, show that sampled regions with the most heterogeneous isotopic values do not correspond to regions with the most heterogeneous trace element values, suggesting that the isotopic $^{87}Sr/^{86}Sr$ heterogeneity is a subtle heterogeneity that is not detectable in the trace element signatures.

Contents

List of Figures

Acknowledgements

I would like to thank my supervisors Johan Lissenberg, Matthew Gleeson and Marc-Alban Millet for their unwavering support and patience in answering my many questions. I would also like to thank Matthew Gleeson and Edward Inglis for their help with the use of lab equipment. I would like to thank Maximiliaan Jansen for his help with calculating partition coefficients. I would also like to thank Jordan Lubbers for his informative answers to my questions regarding how to use his software LaserTRAM-DB. Last but certainly not least, I would like to extend my thanks to Sarah Lambart for kindly donating her samples, and to the Harker Petrology Collection at the Sedgwick Museum, Cambridge, for lending me some of their samples for this research.

1. Introduction

1.1 Context

Most volcanism globally derives from melting of the Earth's mantle. The mantle lies beneath the crust and is the thickest structural layer of the Earth, forming the largest geochemical reservoir of this planet. In order to gain a better understanding of the mantle, it is crucial to uncover the details of its composition.

By understanding the geochemical composition and heterogeneity (including its magnitude and length-scale) of the source regions of volcanism in the mantle, geochemists can gain insight into the processes of geochemical recycling of material from subducted crust, lithosphere and sediments from plate tectonics. This allows scientists to create more accurate models for mantle dynamics involving convection and plate tectonics, and ultimately planetary evolution (Hart, 1988; Hofmann, 1997; Weis *et al.*, 2011; Lambart *et al.*, 2019).

Geochemical studies of erupted oceanic basalts have revealed that the mantle is both chemically and isotopically heterogeneous on a range of scales, from centimetres to thousands of kilometres (Allegre *et al.*, 1980; Zindler and Hart, 1986; Hart, 1988). This compositional heterogeneity derives from early planetary differentiation and recycling of crustal and lithospheric material (particularly oceanic material), which has not been homogenised by mantle convection (Hart, 1988; Hofmann, 1997; Lambart *et al.*, 2019).

Greater understanding of mantle geochemistry can be gained through the study of deep mantle plumes. Mantle plumes are large volumes of magma which rise through the mantle. Seismic studies and mantle flow models (Montelli *et al.*, 2004; Thorne, Garnero and Grand, 2004; Burke *et al.*, 2008) suggest that some originate from a thermal boundary layer at the base of the mantle, near the core-mantle boundary (CMB) (see fig. 1) (Morgan, 1971; Whitehead and Luther, 1975). This includes the Hawaiian mantle plume, whose negative seismic anomaly (indicating higher temperatures) reaches a depth of at least 2350km (Montelli *et al.*, 2004).

The CMB is a thermal boundary layer. The heat released from the core causes material at the CMB to heat up, reach lower density, destabilise and rise through the mantle as a plume

(Whitehead and Luther, 1975; Davies, 1988; Sleep, 1990; Hofmann, 1997; Campbell, 2007). As plume material rises to shallower depths, reduced ambient pressure results in adiabatic decompression melting at shallow depths (Morgan, 1971; White, 2010) and the production of a large volume of magma; when melts deriving from the plume first surface, this sometimes expresses itself on the surface as a large igneous province (LIP), thought to represent the 'plume head', followed then by a chain of oceanic volcanic islands of increasing age, representing the trailing 'plume tail', as seen in Hawaiian chain (Morgan, 1972; Whitehead and Luther, 1975; Campbell, Griffiths and Hill, 1989; Richards, Duncan and Courtillot, 1989; Campbell and Griffiths, 1990; Griffiths and Campbell, 1990; Olson, 1990; Hofmann, 1997).

Despite previous studies demonstrating a head and trailing tail plume morphology, which best reflects thermal plumes, more recent research suggests that this model alone cannot explain the complexity of plumes and hotspots, and that plumes may also differ in chemical composition relative to surrounding mantle (Farnetani and Samuel, 2005; Lin and Van Keken, 2005; Samuel and Bercovici, 2006; Kumagai *et al.*, 2008). This thermochemical nature of plumes results in plumes possibly forming a diverse range of shapes and sizes throughout their evolution (Farnetani and Samuel, 2005; Kumagai *et al.*, 2008).

Deep mantle plumes bring material from the deep mantle to the surface, extruded as basaltic lavas (Hofmann, 1997). As mantle plumes rooted in the deep mantle also display chemical heterogeneity on a range of scales (e.g., Tatsumoto, 1978; Hauri, 1996) due to the preservation of their deep mantle source's geochemical composition and heterogeneity (e.g., Weis *et al.*, 2011) as they rise towards the surface, plumes can be used to gauge a better understanding of deep mantle heterogeneity (Campbell, 2007). Geochemists have used plumes as messengers from the deep mantle (Hofmann, 1997) to understand more about deep mantle composition.

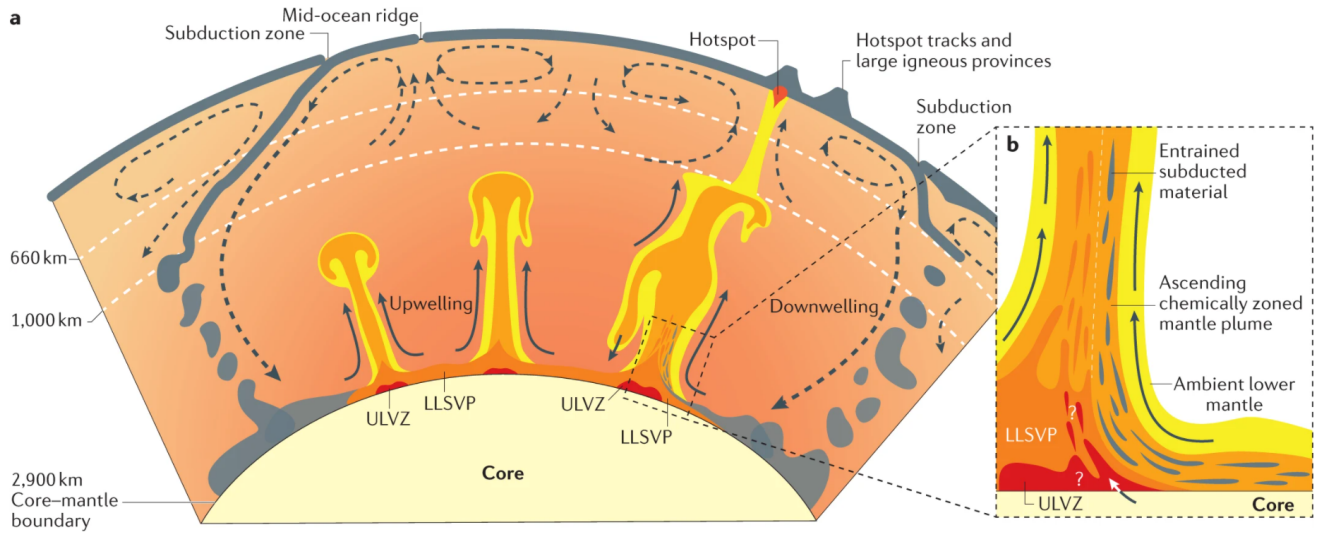

Figure 1: A schematic diagram from Koppers et al. (2021) (showing the dynamic processes involved in whole mantle convection. a) A schematic cross section of the Earth from the surface to the core featuring the subduction and recycling of lithospheric material and Large Low-Shear Velocity Provinces (LLSVPs) at the Core-Mantle boundary (CMB) which may contain Ultra-Low Velocity Zones (ULVZs). Chemically heterogeneous deep mantle plumes, like the Hawaiian plume, may form along the edges of these LLSVPs (e.g., Burke et al., 2008; Weis et al., 2011) and incorporate entrained material from the lower mantle, including recycled material, and form hotspots on the surface which produce LIPs and hotspot tracks. b) Shows the schematic cross section of the base of a plume forming on the edge of an LLSVP, with entrained material from subducted material, ULVZs, LLSVPs, ambient mantle.

Studies have suggested that the material sampled by plumes in the deep mantle could include material from subducted slabs from tectonic plate recycling and mantle convection, including oceanic crust (Hofmann and White, 1982), subcontinental lithospheric mantle (McKenzie and O'Nions, 1983), recycled sediments (Eisele *et al.*, 2002), continental crust (Eisele *et al.*, 2002; Willbold and Stracke, 2010) and oceanic lithosphere (Willbold and Stracke, 2006, 2010) or plume signatures could derive from core-mantle interactions (Brandon and Walker, 2005), or residue from the differentiation of the early Earth (Giuliani *et al.*, 2020). However, despite a multitude of theories, the origin of the geochemical composition in mantle plumes remains debated (White, 2010).

Historically, geochemists have sought to study the geochemistry of mantle using radiogenic isotope signatures of mantle-derived basalts, like erupted OIBs or MORBs, and use this

information to draw conclusions about the nature of mantle composition and heterogeneity (e.g., Allegre *et al.*, 1980; Hart, 1988; Willbold and Stracke, 2010). This is done under the assumption that the basalts are a direct reflection of their source mantle. However, Lambart et al. in 2019, studying the heterogeneity of the depleted upper mantle, found that the isotopic composition of minerals of lower crustal cumulates preserved significantly greater degrees of heterogeneity than locally erupted mid ocean ridge basalts (MORBs) (see fig. 2). Hence, at least in the northern area on the Mid-Atlantic Ridge (30° N) studied by Lambart et al. (2019), the lavas grossly underestimated the true heterogeneity of the original upper mantle source. This was hypothesized to result from magma mixing in crustal magma chambers, meaning the true heterogeneity of the source is homogenised (Cipriani et al., 2004**;** Dungan and Rhodes, 1978; Rhodes *et al.*, 1979; Batiza, 1984). Crystal scale Nd and Sr isotopic analysis of primitive cumulate crystals from the lower crust, however, showed greater heterogeneity than their associated lavas, which indicates that they are a better reflection of the true composition of the mantle source (Lambart *et al.*, 2019).

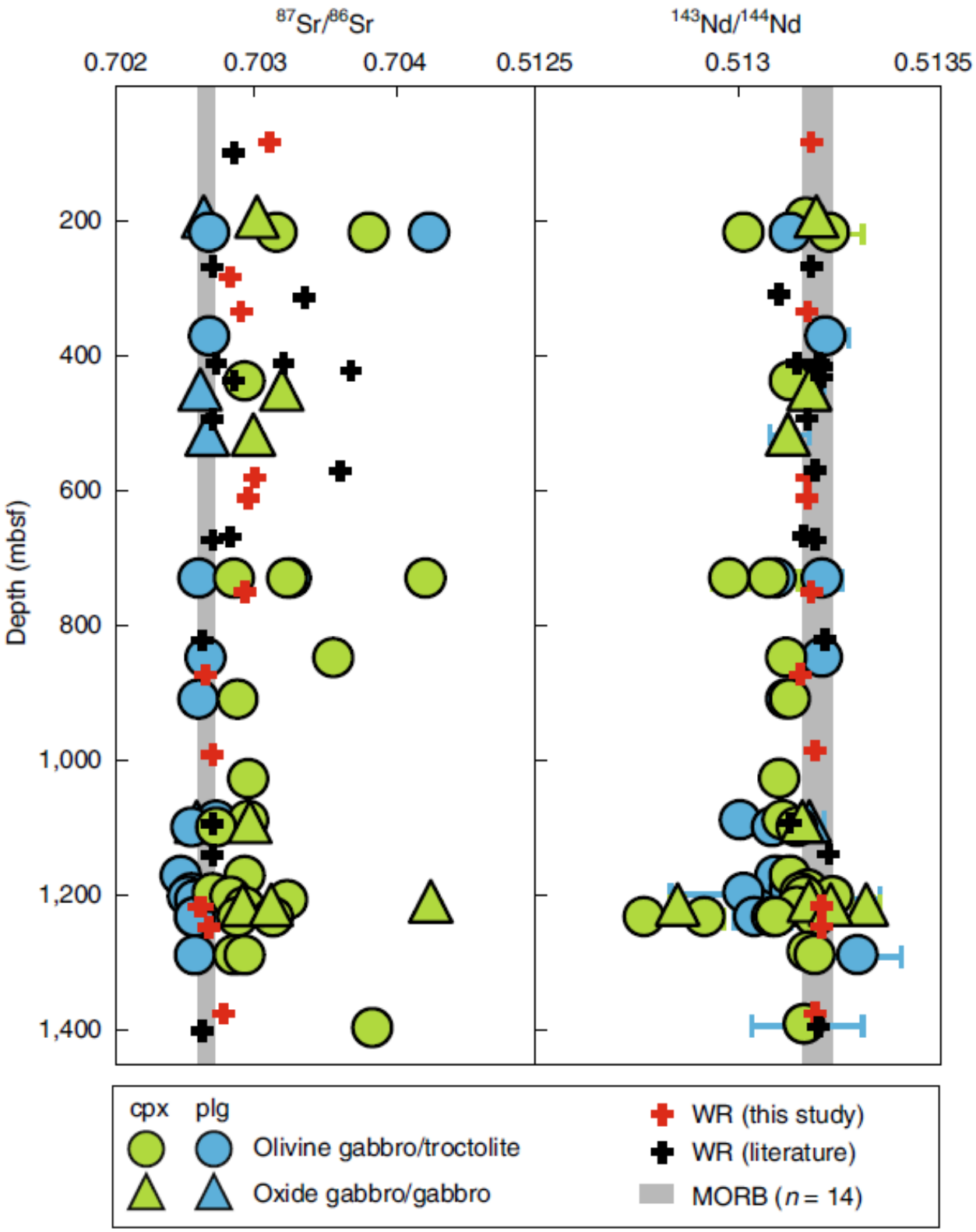

Figure 2: A figure from Lambart et al. (2019) showing clinopyroxene (cpx) and plagioclase (plg) core $^{87}Sr/^{86}Sr$ and $^{143}Nd/^{144}Nd$ isotopic ratios from Atlantis Massif cumulate gabbroic rocks (from IODP hole U1309D), alongside whole rock (WR) isotopic analyses of gabbroic

rocks. The grey band, representing MORB compositional variability for the same latitude, demonstrates that the cumulates show a far greater range of isotopic variability than the MORB lavas. mbsf denotes metres below seafloor, and error bars represent 2 SE (standard error of the mean).

The implications of the findings of Lambart et al. (2019) are profound. Geochemists have used MORB to study the composition of the Earth's mantle since the 1960s (e.g., Ringwood, 1962; Schilling, 1973). If basalts underestimate source heterogeneity, then there may be ~60 years of data which provide only a partial picture of the details of the geochemical composition and geochemical heterogeneity of the depleted mantle. Furthermore, it is possible that OIBs also underestimate the heterogeneity preserved in their mantle plume sources.

Extrapolating the findings of Lambart et al. (2019), it may be possible to place better constraints on the heterogeneity of the plume mantle through the crystal-scale analysis of cumulate minerals preserved in ocean island basalts. This study is the first project to apply this approach to the study of plumes by using similar methods to study the mantle plume beneath Hawaii by using lower crustal xenoliths brought to the surface by the 1800 Hualalai eruption. Using this approach, this study aims to provide insight into the sub-volcanic system and test whether Hawaiian lower crustal cumulates reveal greater chemical heterogeneity in the mantle plume than their corresponding lavas. The hypothesis of this study is that this will be the case as magma mixing in crustal magma chambers can compromise/mask the heterogeneity recorded in erupted lavas, but lower-crustal rocks may have managed to avoid extensive mixing and homogenisation prior to crystallisation, enabling more accurate constraints on short length-scale isotopic heterogeneity of the Hawaiian plume to be found.

1.2 Geological setting: The Hawaiian Mantle Plume

The Hawaiian mantle plume is the hottest and most productive plume on Earth (Weis *et al.*, 2011). Seismic studies reveal that this plume is rooted in the deep mantle, with negative seismic anomalies (indicating higher temperatures relative to surrounding mantle) detected

vertically from 1000km to the CMB, beneath Hawaii (Cottaar and Romanowicz, 2012; French and Romanowicz, 2015).

The Hawaiian-Emperor seamount chain has formed over 80 million years (Keller et al., 1995) and extends over 6100km, with a bend in the chain at 55-45Ma (Sharp and Clague, 2006; Clague and Sherrod, 2014). The Hawaiian-Emperor seamount chain is the type example of intra-plate volcanism. These seamounts and islands, including Hawaii, form a line of age progressive hotspot volcanism resulting from the motion of the Pacific plate to the north-west over the Hawaiian mantle plume at a rate of ~9-10cm per year (for volcanoes of the Hawaiian chain), with younger volcanoes therefore to the south-east (Clague and Dalrymple, 1987; Garcia et al., 1987).

The average lifetime of Hawaiian volcanoes is hypothesised to last ~1.4Ma (Guillou *et al.*, 1997). A progression for the evolution of Hawaiian volcanoes over their lifetime was first proposed by Stearns (1946). This lifecycle has since been refined to suggest that Hawaiian volcanoes gradationally transition through 4 stages, pre-shield, shield, post-shield and rejuvenation stages, each with different eruptive volumes and compositions (Stearns, 1946; Clague and Dalrymple, 1987; Clague, 1987; Peterson and Moore, 1987; Clague and Sherrod, 2014). These stages have been attributed to differences in heat supply from the plume as the volcano passes over it (Wolfe and Morris, 1996). During the pre-shield stage, the volcano is on the edge of the plume, receiving less heat, resulting smaller amounts of partial melting, and the production of alkalic lava (Moore et al., 1982; Wolfe and Morris, 1996). In the shield stage volcanoes reach their peak productivity; the volcano has a robust magma supply to a shallow magma reservoir at a depth of 3-7km supporting the eruption of large quantities of tholeiitic lava (Ryan et al., 1981; Clague, 1987; Decker, 1987; Wolfe and Morris, 1996). In the post-shield stage, as the volcano drifts away from the Hawaiian plume centre, decreased melting and magma supply results in a reduced volume of erupted lava of alkalic composition (Clague, 1987; Frey *et al.*, 1990). In this stage, the reduced heat supply is no-longer able to support a shallow magma reservoir, which solidifies, resulting in the formation of a smaller reservoir at a depth of ~20km, at the base of the crust at Hawaii (Bohrson and Clague, 1988; Frey *et al.*, 1990). The rejuvenated stage describes a period of renewed activity, involving a small volume of alkalic lava extrusion after a period of

inactivity, though this hiatus may vary significantly between volcanoes and the transition into this stage may remain unclear (Clague, 1987; Clague and Sherrod, 2014).

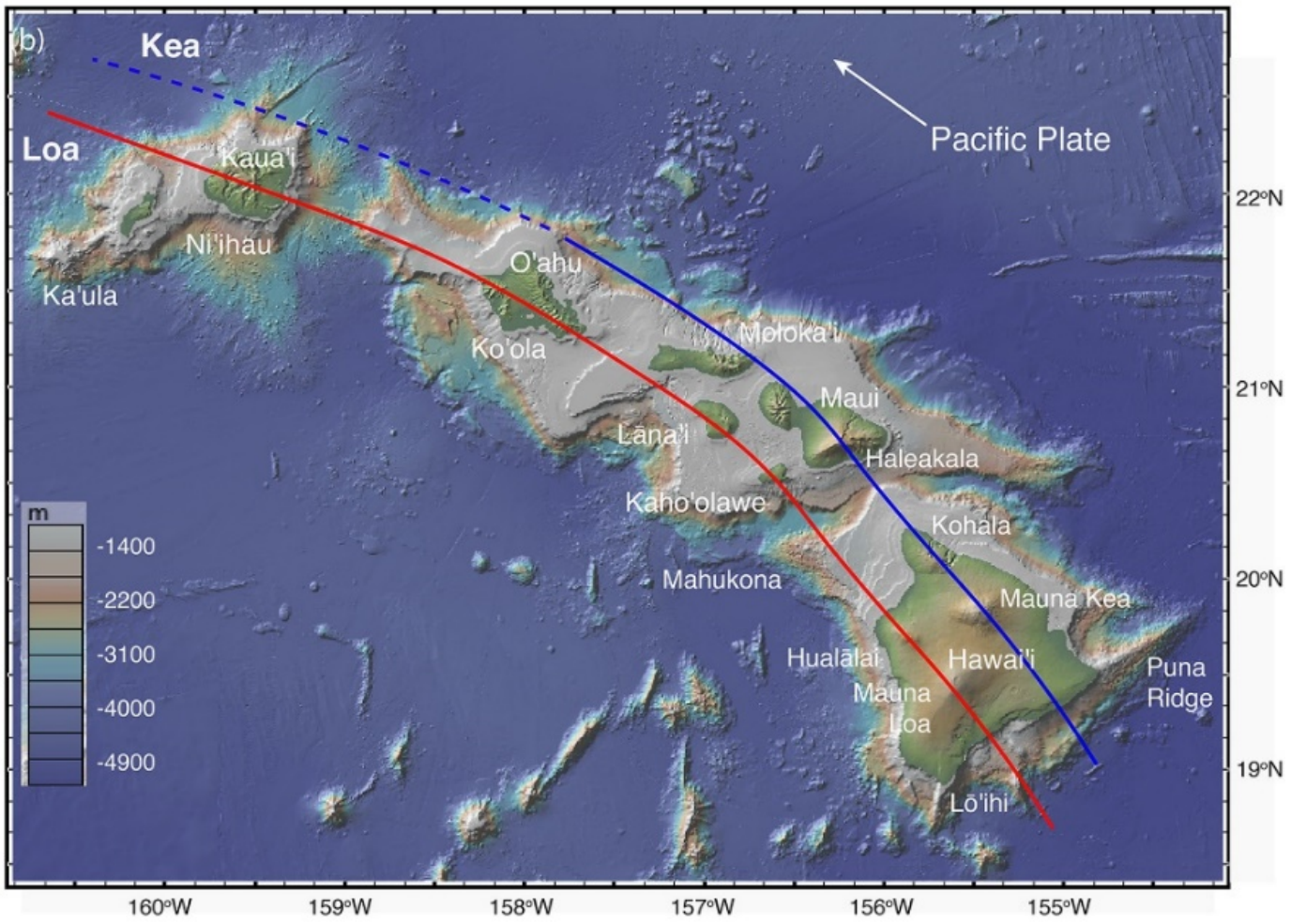

Figure 3: A map of the Hawaii Archipelago from Harpp and Weis (2020) showing the chain of volcanoes aligned with the movement of the Pacific plate, forming 2 subparallel trends, Loa (the red line) and Kea (the blue line), of geochemically distinct volcanoes (e.g., Jackson et al., 1975; Tatsumoto, 1978) which represent largescale geochemical heterogeneity in the Hawaiian plume (e.g., Abouchami et al., 2005; Weis et al., 2011).

Hawaii's chain of age-progressive volcanoes forms two subparallel chains marked by distinct isotopic differences (see fig. 3) (Jackson *et al.*, 1975; Tatsumoto, 1978). This large-scale geochemical heterogeneity is thought to be the surface expression of a bilaterally asymmetrical Hawaiian plume (Abouchami *et al.*, 2005; Weis *et al.*, 2011) which seismic data has shown to be rooted near the core-mantle boundary (CMB) and straddling the border between ambient Pacific mantle and the Pacific Large Low Shear Velocity Province (LLSVP)

(see fig. 4) (Burke *et al.*, 2008; Weis *et al.*, 2011), an anomalously dense region at the CMB with low seismic shear-wave velocity, and bounded by steep velocity gradients, thought to represent a thermochemical pile (e.g., Ishii and Tromp, 1999; Garnero et al., 2016). The geochemical composition of the two trends, Loa and Kea, reflect enriched Pacific LLSVP and depleted ambient Pacific mantle sources, respectively, due to the preferential sampling of these different deep mantle sources by the Hawaiian plume (Weis *et al.*, 2011) (see fig. 5). The minimal internal mixing within the Hawaiian mantle plume postulated by Weis *et al.* (2011) suggests that the surface expression of the plume reflects the geochemical nature of the deep mantle source (Weis *et al.*, 2011).

This compositional boundary trends NW-SE, with depleted Pacific lower mantle to the NE, and enriched more heterogeneous Pacific LLSVP to the SW (Weis *et al.*, 2011).

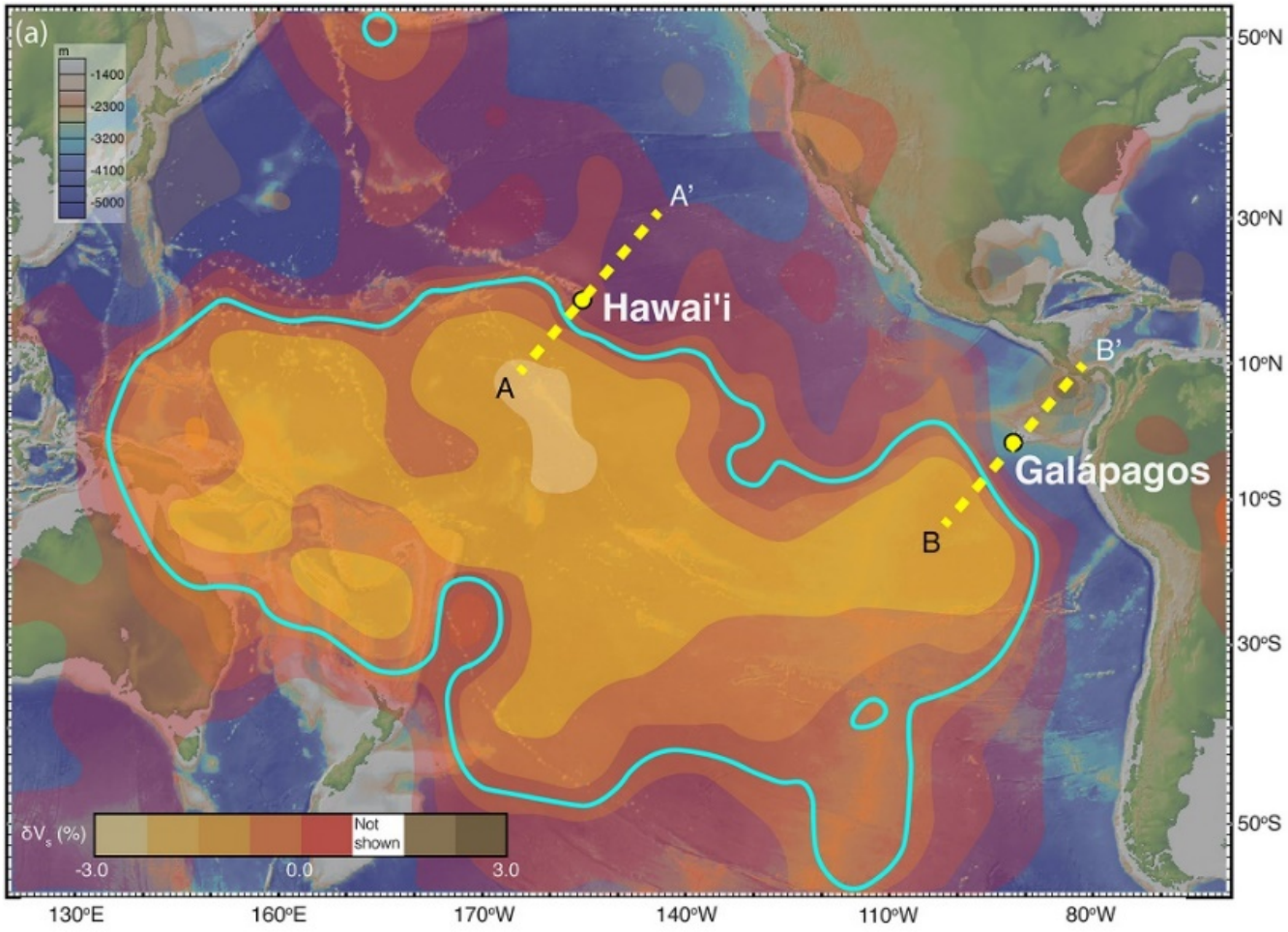

Figure 4: A map from (Harpp and Weis, 2020) showing the positions of both Hawaii and the Galapagos relative to the Pacific Large Low-Shear Velocity Province (LLSVP). Lines A-A' and B-B' are cross-sections across the LLSVP boundary, with A-A' reflecting the transition from

the Loa trend to the Kea trend in Hawaii. The velocity contours shown in the figure are from the SMEAN2 composite tomography model and adapted from figure 1 in Jackson et al. (2018), with the blue line highlighting 75% of the RMS velocity contour for the model at a depth of 2,875km.

The Pacific LLSVP, feeding Loa trend volcanoes, is compositionally heterogeneous and enriched due to contributions from recycled and near primordial material (Ballmer et al., 2016; Harpp and Weis, 2020; Williams et al., 2019), including Enriched Mantle-1 (EM1) (Zindler and Hart, 1986; Weis *et al.*, 2011), Enriched Makapuu (EMK) (which could contain recycled crust and sediment (Hauri, 1996; Huang and Frey, 2005; Huang *et al.*, 2005; Tanaka and Nakamura, 2005; Tanaka et al., 2008)) and Depleted Makapuu (DMK) components (Tanaka et al., 2002; Tanaka et al., 2008). Fine-scale heterogeneity in the Loa trend could also be derived from an Ultra-Low Velocity Zone (ULVZ), a thin region, commonly 5-20km, of strongly reduced S- and P- wave velocities, likely due to partial melt, underlying the plume on the edge of the Pacific LLSVP (Williams and Garnero, 1996; Williams et al., 1998; Garnero and McNamara, 2008; McNamara et al., 2010; Weis *et al.*, 2011; Cottaar and Romanowicz, 2012; Garnero et al., 2016). The ambient Pacific mantle source for Kea, however, has a composition similar to that defined by the Common component (C) (Hanan and Graham, 1996; Nobre Silva et al., 2013), Focus Zone (FOZO) (Hart *et al.*, 1992; Harpp and Weis, 2020) and Prevalent Mantle component (PREMA) (Zindler and Hart, 1986; Weis *et al.*, 2011).

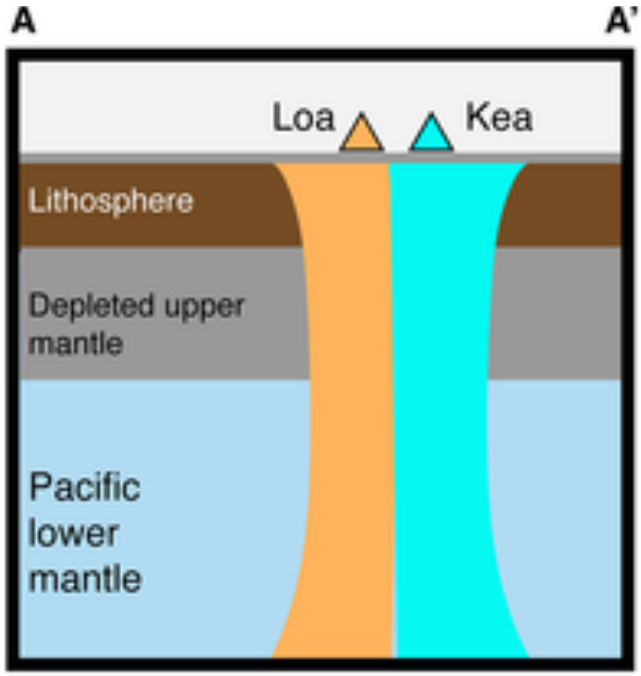

(a)

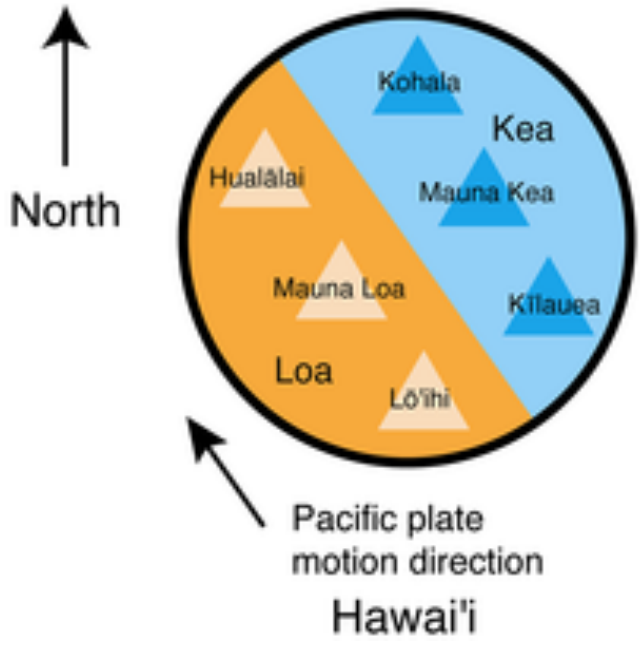

(b)

Figure 5: A schematic diagram from Harpp and Weis (2020) showing the mechanism for the formation of broad length scale heterogeneity at Hawaii. a) A simplified schematic of a bilaterally asymmetric plume beneath Hawaii rising from the Core-Mantle boundary (CMB) with bright blue representing the depleted Pacific lower mantle (the source for Kea trend volcanoes in Hawaii), and orange representing more enriched material derived from the Pacific Large Low-Shear Velocity Province (LLSVP) (the source for Loa trend volcanoes in

Hawaii) (e.g., Weis et al., 2011). (b) A depiction of how the present-day motion of the Pacific plate (from Williamson et al. (2019)) interacts with the bilaterally asymmetric Hawaiian plume (enriched-depleted boundary of the plume based on Williamson et al. (2019) and tomographic models like in Jackson, Becker and Konter (2018)) to generate the Loa (orange) and Kea (blue) trends expressed at the surface.

Hualalai is one of the five volcanoes on the Island of Hawaii, on the western side of the island and forming part of the Loa trend of volcanoes (see fig. 3). It is the third youngest volcano on the island of Hawaii and has been in the post shield stage for ~120Ka (Bohrson and Clague, 1988). Hualalai most recently erupted in 1800-1801, with the formation of the 1800 Kaupulehu and 1801 Huehue alkalic basalt flows (see fig. 6). Both flows contain xenoliths that were deposited in beds after being entrained by the host magma; the Huehue flow has mafic and ultramafic xenoliths at the base of the flow, whereas the Kaupulehu flow contains more abundant and larger (<1-35cm) xenoliths (Bohrson and Clague, 1988). The cumulate xenoliths of the Kaupulehu flow are most commonly of dunitic, wehrlitic and olivine clinopyronxenitic composition, with some cumulates ranging between those compositions, including minor troctolites, gabbros, websterites and anorthosites (Jackson et al., 1981; Chen et al., 1992). These xenoliths are mid- to deep crustal cumulates, with some gabbros reflecting ocean crust gabbro in rare instances (Clague, 1987; Clague and Sherrod, 2014).

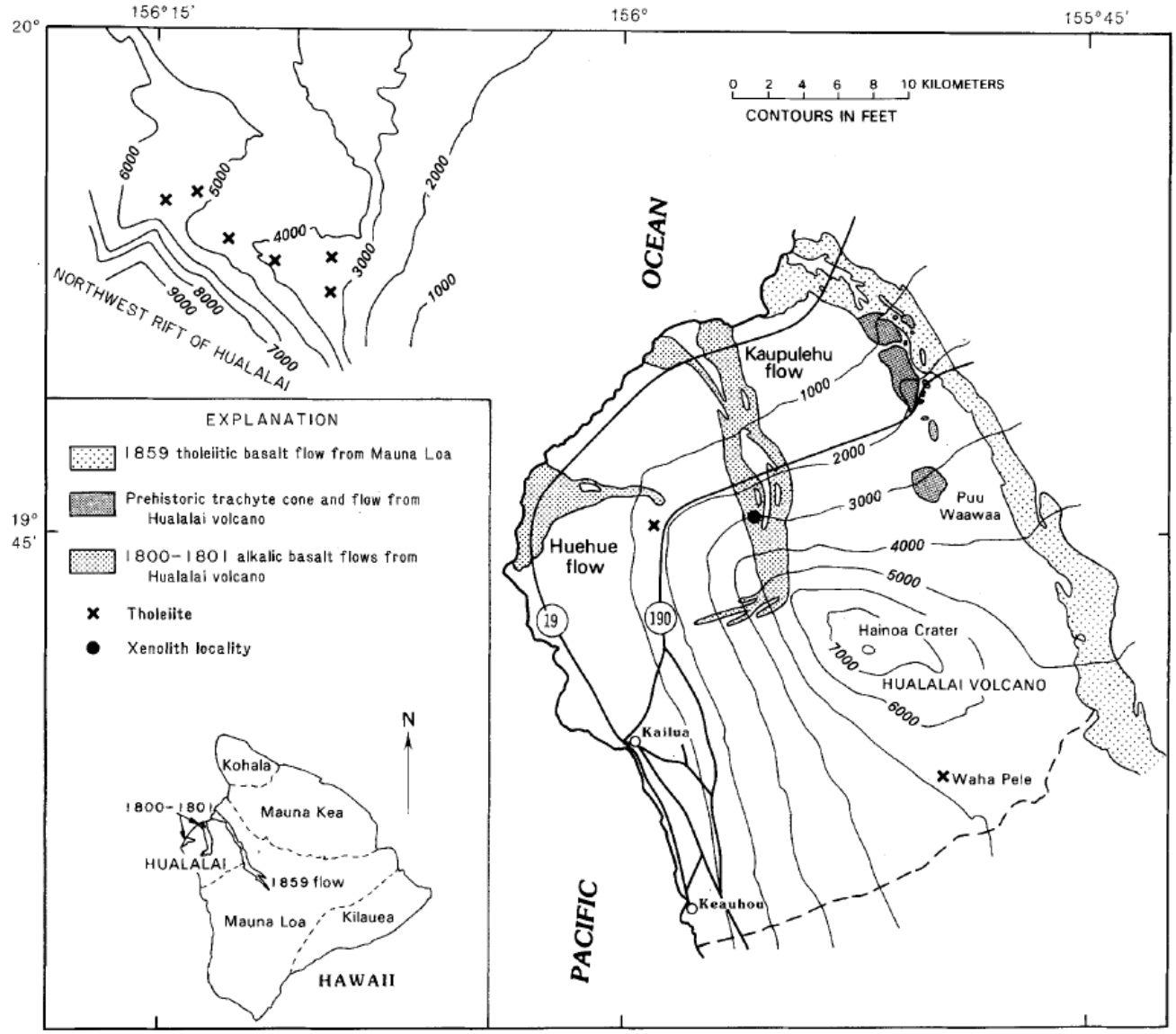

Figure 6: A figure from Bohrson and Clague (1988), adapted from (Moore *et al.*, 1987) *showing the Hualalai volcano alongside part of the submarine northwest rift, and the locations of the 1800-1801 Huehue and Kaupulehu lava flows. The dashed line in the main figure image shows the approximate location of the southern edge of Hualalai. The location of Hualalai relative to the rest of the island of Hawaii is shown in the bottom left. Bathymetry was used from Campbell and Erlandson (1979).*

2. Analytical Methods

2.1 SEM analysis

During this project, plutonic xenolith samples 101870 (wehrlite) and 81862 (wehrlite), from Hualalai volcano Hawaii were mapped (see methodology below). Element maps of samples H1, H3, H7, 106426, 101863, 81869 and 81874 were produced by Dr Matthew Gleeson and studied during this project.

Lower crustal xenolith fragments were studied using EDS and WDS analysis on the Zeiss Sigma HD Field Emission Gun Analytical SEM fitted with two Oxford Instruments 150 mm^2 energy dispersive X-ray spectrometers (EDS) and an Oxford Instruments Wave wavelength dispersive X-ray spectrometer (WDS) at Cardiff University to identify compositional crystal domains using element mapping, and for mineral major element quantitative spot analysis. Qualitative element maps were made using EDS to assess any potential variations in mineral compositions across the sample and any chemical domains within individual crystals. This enabled the identification of areas that showed potential to record the full chemical heterogeneity across the sample, which were then targeted by spot analysis. Samples were mapped using a 120µm aperture, 20kv accelerating voltage, 8.9µm working distance, 20,000µs dwell time, 128*98 pixels per frame, 120x magnification, 18µm spatial resolution, and signal process time set to the AZtec preset value 1. After analysis, the EDS maps were converted into 'TruMaps' using the AZtec software, which provides a background correction to the EDS spectra and allows the true count rate for each element to be determined. Initially, element and multi-element maps were constructed in the AZtec software, with the brightness and contrast values for each element adjusted to highlight chemical variations. In addition, the background corrected count rates for each element were also exported as .csv files. These files were further examined and used to assess the primary mineral compositions for the samples via cluster analysis (to separate mineral phases) using the open-source software 'QACD-quack' © 2019 by Matthew Loocke downloaded from *https://mloocke.wixsite.com/qacd-quack* on 20 June 2022 (Loocke, 2016).

Clinopyroxene, plagioclase and olivine major- and minor element compositions for samples H1, H7, H3, 101870, 81862, 106426, 101863, 81874 and 81869 were determined by spot analysis using the two 150 mm2 X-Max EDS detectors. Analysis was done using a 60µm aperture, ~1.1 nA beam current, and signal process time set to the AZtec preset value 3 (increased process time relative to the map collection allows erroneous voltage jumps to be identified and discarded, lowering background count rates), 20kv accelerating voltage and 10s count time. Spot analysis was performed by rastering the beam over an area ~10um by 10um.

Plagioclase major element compositions for samples 81869, 106426, 81874 and 101863 were determined by spot analysis using the WDS detector for low concentration Mg and K analysis, and using the EDS detector for all other elements. EDS analysis (for high concentration elements) was done using 60µm aperture, ~1.1 nA beam current, and signal process time set to the AZtec preset value 3, 20kv accelerating voltage and 10s count time. Spot analysis was performed by rastering the beam over an area ~10um by 10um. WDS analysis (for K and Mg) was done using a 300µm aperture, ~20nA beam current, signal process time set to the AZtec preset value 3 and 20kv accelerating voltage. Background count times were 30s for Mg and 20s for K, and peak times were 60s and 40s for Mg and K respectively. Mg counts were collected on the TAP crystal, and K counts were collected on the PET crystal. Spot analysis was performed by rastering the beam over an area ~10um by 10um.

Analytical uncertainty was tracked through the analysis of appropriate Astimex Microanalysis Standards. Precision and accuracy values (averaged across all runs) for all elements analysed in the Astimex Diopside and Plagioclase standards are shown in the appendix.

2.2 Laser Ablation

The locations of apparent clinopyroxene and plagioclase cores and rims (as seen on the 2-dimensional element maps) of 3 wehrlite (101870, H3 and H1) and 4 gabbro (101863, 81896, 106426 and 81874) samples studied on the SEM were targeted for laser ablation

inductively coupled plasma mass spectrometry (LA-ICP-MS) using a ASI RESolution 193 nm ArF excimer laser ablation system coupled to an Agilent 8900 QQQ-ICP-MS in the Cardiff University Celtic Labs to collect trace element concentrations. Analyses were collected in spot mode using a 5Hz repetition rate, 4.5J/cm² fluence, and 80µm spot size. Laser ablation data reduction was carried out in LaserTRAM-DB (Lubbers, Kent and Russo, 2021) using ^{43}Ca (from EDS analysis) as the internal reference standard, and USGS glass standard BCR-2G (Jochum *et al.*, 2010) as the standard reference material for clinopyroxene data and NIST SRM 612 (Jochum *et al.*, 2011) as the standard reference material for plagioclase data.

Analytical uncertainty was tracked using USGS glass standards GSD-1G (Jochum *et al.*, 2011), BHVO-2G and BCR-2G (Jochum *et al.*, 2010), MPI-DING reference glasses KL2-G, StHs6/80-G, T1-G, and ATHO-G (Jochum *et al.*, 2011) and NIST SRM glasses NIST SRM 610 and NIST SRM 612 (Jochum *et al.*, 2011). NIST SRM glass NIST SRM 612 was the main standard used to track analytical uncertainty after data reduction using ^{43}Ca (from EDS analysis) as the internal reference standard, and USGS glass standard BCR-2G as the standard reference material (for clinopyroxene data). USGS glass standard BCR-2G was the main standard used to track analytical uncertainty after data reduction using ^{43}Ca (from EDS analysis) as the internal reference standard, and NIST SRM 612 as the standard reference material (for plagioclase data).

Analytical accuracy and precision for standards NIST SRM 612 (Jochum et al., 2011) and BCR-2G (Jochum et al., 2010) can be found in the appendix.

Trace element data from laser ablation was normalised to the primitive mantle using primitive mantle values given by McDonough and Sun (1995). This follows the convention set out by recent papers on similar topics, including the study by Gleeson et al. (2022) on xenoliths from the Galapagos (see figure 4 in Gleeson et al. (2022)), and Yang et al. (2023) on Hawaii (see figure 3 in Yang et al. (2023)).

2.3 Micromilling

Clinopyroxene and plagioclase crystals were sampled using a micromill equipped with diamond drill tips for the extraction and isotope analysis of strontium (and neodymium for future isotopic work). Crystals targeted for drilling were selected based on major- and trace element data and element maps; areas were drilled that displayed the greatest variation in major- and trace element composition, so showed the greatest potential for heterogeneity across crystals and across the sample. The areas were also selected if they were able to provide a minimum of 10ng of Nd from the material drilled based on Nd concentrations from LA ICP-MS data. The raster spacing used was 250. The resulting powder was transferred to 16ml Teflon beakers by adding Milli-Q water to the powder and a pipette to collect the resulting material held in suspension. The drill bit was cleaned after each milling step using an ultrasonic bath of Milli-Q water and by being wiped with ethanol. The sample surface was cleaned after each milling step by rinsing with Milli-Q water and wiping with ethanol, and pipette tips were replaced after each milling step.

2.4 Sample digestion

Rock powder samples were prepared using one digestion method. Samples were placed in 16ml Teflon beakers and dissolved using 300µl 16M HNO_3 and 500µl 28M HF and left to reflux on a hot plate at 120°C for 16 hours. Following dissolution, samples were dried down and brought into solution in 600µl of 16M HNO_3 and refluxed on a hot plate at 120°C for 16 hours 3 times.

2.5 Sr column chemistry

Samples were then dried down again and brought into solution for Sr column chemistry in 1ml 8M HNO_3 and refluxed on a hotplate at 120°C.

Strontium was separated using Sr ion exchange chemistry techniques (Horwitz et al., 1992) using Sr-spec resin in homemade pipette tip columns that were fritted with PTFE frit material. Strontium was separated from the sample matrix using homemade pipette tip

columns filled with 200µl Triskem Sr-Spec resin. First the empty columns were prepared by filling them with 200µl of resin and cleaning the resin with 3ml 6M HCl, 6ml Milli-Q water, 3ml 10M HCl and another 6ml Milli-Q water, loaded 1ml at a time.

For the first step of the Sr column chemistry, the resin was cleaned with 3ml 6M HCl, 6ml Milli-Q water, another 3ml 6M HCl and 6ml Milli-Q water, loaded 1ml at a time. The resin was then preconditioned with 200µl 8M HNO_3 3 times. A set of 16ml Teflon beakers were placed below the columns in order to collect samples for future Nd column chemistry, apart from the blank, where the same beaker was rinsed with Milli-Q water and re-used to collect the sample after it was loaded into the column. Separate pipette tips for each sample, rinsed in 8M HNO_3, were used to load the samples which were brought into solution in 1ml 8M HNO_3 in 500µl increments. The matrix was then eluted with 8M HNO_3 in steps of 50µl, 100µl, 150µl, 200µl, 400µl, and another 400µl. Sr was eluted with 3 loads of 0.5ml 0.05M HNO_3 and collected in the original sample beakers for Sr chemistry after cleaning (using 1ml 16M HNO_3 and refluxed on a hot plate, then rinsed with Milli-Q water). The Sr beakers were then dried down on a hotplate. Columns were rinsed twice with 1ml Milli-Q water. This Sr chemistry process was repeated a second time.

Sr ion exchange chemistry: Day 1	
Cleaning the resin	1ml 6M HCl x3
	1ml Milli-Q water x6
	1ml 6M HCl x3
	1ml Milli-Q water x6
Preconditioning the resin	200µl 8M HNO_3 x3
Load the sample brought into a solution with 1ml 8M HNO_3	Load in 500µl increments
Elute matrix	50µl 8M HNO_3
	100µl 8M HNO_3
	150µl 8M HNO_3
	200µl 8M HNO_3
	400µl 8M HNO_3
	400µl 8M HNO_3
Elute Sr	0.5ml 0.05M HNO_3 x3
Clean the resin	1ml Milli-Q x2

Sr ion exchange chemistry: Day 2	
Cleaning the resin	1ml 6M HCl x3
	1ml Milli-Q water x6
	1ml 6M HCl x3
	1ml Milli-Q water x6
Preconditioning the resin	200µl 8M HNO_3 x3
Load the sample brought into a solution with 1ml 8M HNO_3	Load in 500µl increments
Elute matrix	50µl 8M HNO_3
	100µl 8M HNO_3
	150µl 8M HNO_3
	200µl 8M HNO_3
	400µl 8M HNO_3
	400µl 8M HNO_3
Elute Sr	0.5ml 0.05M HNO_3 x3
Clean the resin	1ml Milli-Q x2

Table 1: A summary of the methodology for Sr ion exchange chemistry (Horwitz, Chiarizia and Dietz, 1992).

Strontium samples were then brought into solution with 200µl H_2O_2 and refluxed on a hotplate. The samples were then dried down, and brought into solution with 1ml concentrated HNO_3 to reflux on a hotplate. The samples were then dried down and brought into solution in 1ml 2% HNO3 to reflux on a hotplate.

2.6 ICP-MS

$^{87}Sr/^{86}Sr$ isotopic data alongside the internal precision for each data point (2se) was measured using the Nu Plasma 2 multi collector ICPMS instrument at Cardiff University. The samples were uptaken at a dilution of 50ppb and instrudiced to the instrument as a dry aerosol using a Cetac Aridus 2 desolvation system. The acquisition was performed in static

mode, with all the isotopes of Sr being measured. The signal intensity was equilivant to ~20v on Sr88. The Rb interference correction on mass 87 was done according to a $^{87}Rb/^{85}Rb$ ratio of 0.3857. Similarly, the Kr interference correction on mass 86 was done on the basis of a $^{86}Kr/^{84}Kr$ of 0.30353. The $^{87}Sr/^{86}Sr$ isotopic data was normalised to an $^{88}Sr/^{86}Sr$ of 8.3752. As the primary standard NBS987 (Zhang and Hu, 2020) typically runs slightly high after the first normalisation, a secondary normalisation was conducted to the reference value of the NBS987 standard of 0.710248 (Zhang and Hu, 2020).

The average value of the in-house EC-5 standard run alongside the samples was 0.709156 +/- 0.000012 (2sd) and the long-term average of the standard is 0.709162 +/- 0.000017 (2sd, n=124). The values for the EC-5 standard were therefore within analytical uncertainty of the long-term value, and the precision (2sd) of the standard was 0.000012.

3. Modelling

3.1 MELTS Major Element Model

The LLD (liquid line of descent) and SLD (solid line of descent) were modelled to represent the path of fractional crystallisation of major and trace element data.

In order to model the effects of fractional crystallisation on the evolution of the Hualalai samples' compositions, a model for the expected path of fractional crystallisation of basaltic melts was creating using the MELTS software, version v.1.2.x (Gualda *et al.*, 2012). This model was compared to the samples' array trends and core-rim trends to see if these trends could be explained by crystal fractionation, or whether primary signatures may have been overprinted or altered, and mechanisms like diffusion and alteration must be invoked to explain these trends.

Published post-shield volcanic whole rock data downloaded from the GEOROC database (https://georoc.eu/) on 6 October 2021, using the following parameters: geographical location = Hualalai; Hawaii: rock type = volcanic. The post-shield data found on GEOROC was compiled from published data (Washington, 1923; Washington and Keyes, 1928; Piggot,

1931; Lessing et al., 1963; Lessing and Catanzero, 1964; Powell et al., 1965; Hamilton, 1965; Somayajulu et al., 1966; Tatsumoto, 1966; Macdonald, 1968; Funkhouser et al., 1968; Schilling and Winchester, 1969; O'Nions et al., 1977; Anonymous, 1980; Clague et al., 1980; Moore and Clague, 1987; Moore *et al.*, 1987; Clague, 1987; Clague and Bohrson, 1991; Sobolev and Nikogosian, 1994; Sims *et al.*, 1995; Pickett and Murrell, 1997; Sims and Depaolo, 1997; Sims *et al.*, 1999; Stracke et al., 1999; Cousens et al., 2003; Hanano *et al.*, 2010; Shea *et al.*, 2017), and falls into two categories; basalt and trachyte. After having plotted major element (wt%) vs MgO (wt%), it was established that some of the samples labelled as trachyte on the GEOROC database sat within the basaltic array. These graphs revealed that these 'trachytes' would not have a sufficient alkali content to conform to the formal definition of a trachyte. Therefore these samples have been reclassified as basalts, and plotted as such, for the rest of this thesis (including previous and subsequent graphs in this thesis involving data downloaded from the GEOROC database (https://georoc.eu/) on 6 October 2021, using the following parameters: geographical location = Hualalai; Hawaii: rock type = volcanic containing these basalts labelled as 'trachytes').

The following samples were reclassified from their original description of trachyte in the GEOROC database to basalt:

- Sample 67-101 (R. Moore *et al.*, 1987)
- Samples 67-101, 67-103, 67-114 and 67-102 (Clague, Jackson and Wright, 1980)

These samples are highlighted blue in the following Major Element vs MgO graphs:

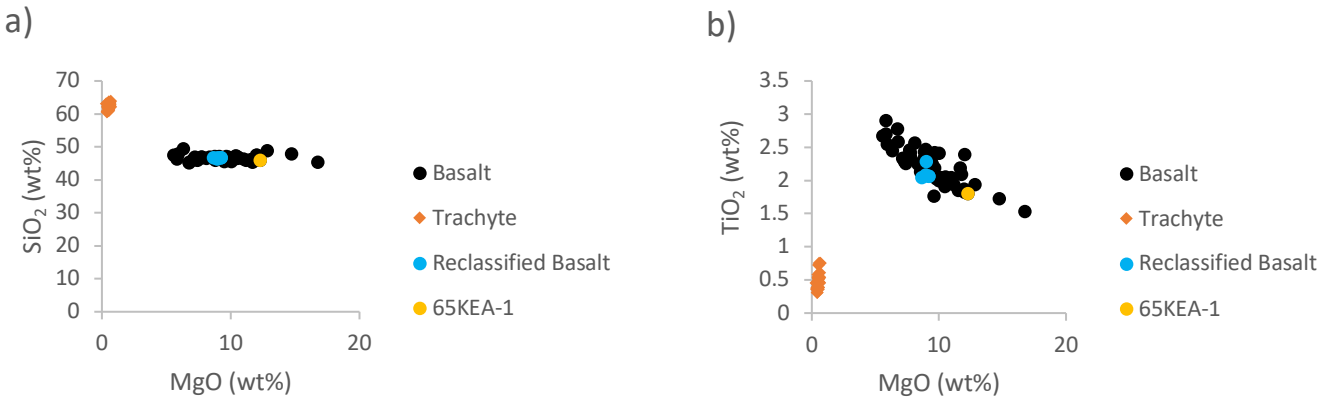

c)

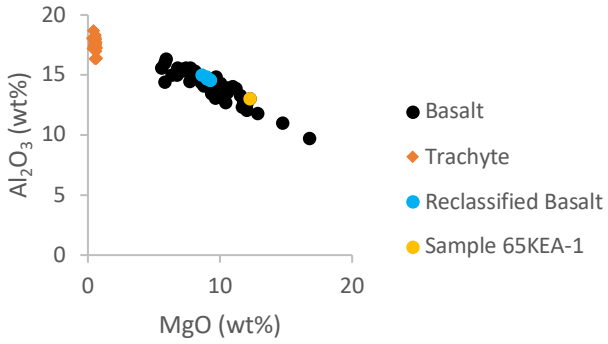
20
15
10
5
0
0
10
20
Al2O3 (wt%)
MgO (wt%)
Basalt
Trachyte
Reclassified Basalt
Sample 65KEA-1

d)

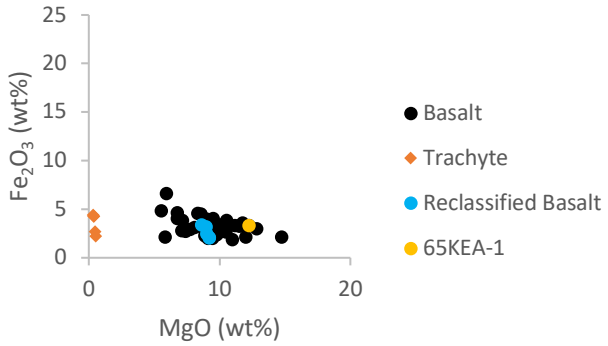
25
20
15
10
5
0
0
10
20
Fe2O3 (wt%)
MgO (wt%)
Basalt
Trachyte
Reclassified Basalt
65KEA-1

e)

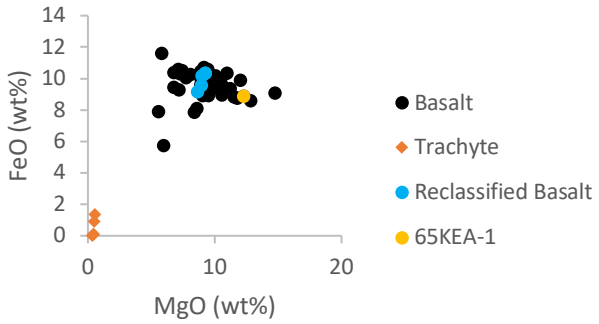
14
12
10
8
6
4
2
0
0
10
20
FeO (wt%)
MgO (wt%)
Basalt
Trachyte
Reclassified Basalt
65KEA-1

f)

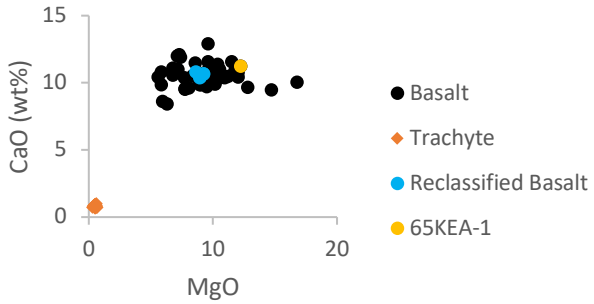
15
10
5
0
0
10
20
CaO (wt%)
MgO
Basalt
Trachyte
Reclassified Basalt
65KEA-1

g)

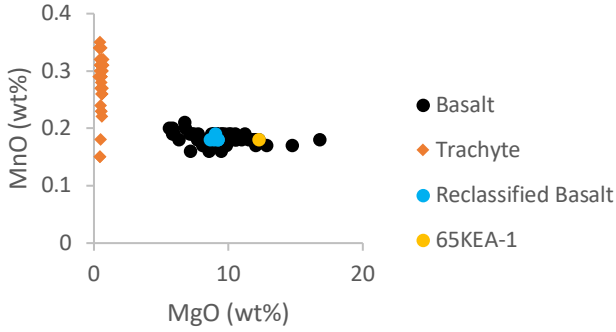
0.4
0.3
0.2
0.1
0
0
10
20
MnO (wt%)
MgO (wt%)
Basalt
Trachyte
Reclassified Basalt
65KEA-1

h)

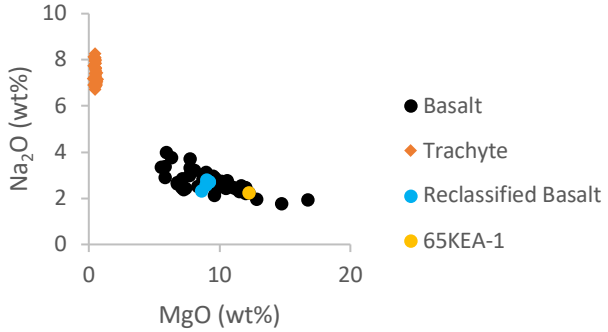
10
8
6
4
2
0
0
10
20
Na2O (wt%)
MgO (wt%)
Basalt
Trachyte
Reclassified Basalt
65KEA-1

i)

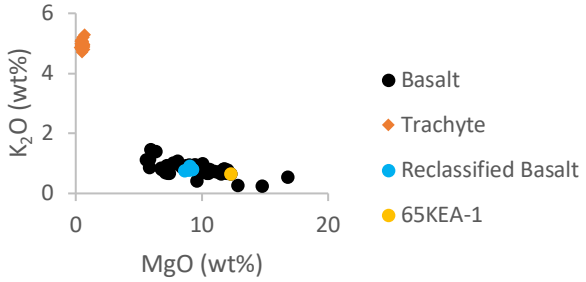
6
4
2
0
0
10
20
K2O (wt%)
MgO (wt%)
Basalt
Trachyte
Reclassified Basalt
65KEA-1

j)

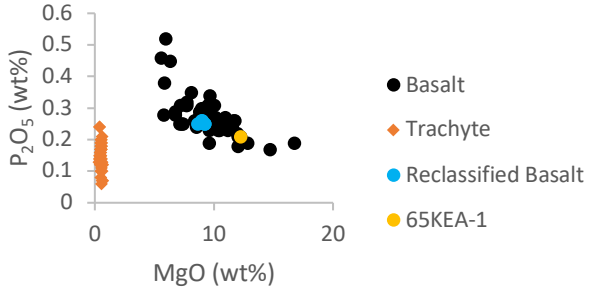
0.6
0.5
0.4
0.3
0.2
0.1
0
0
10
20
P2O5 (wt%)
MgO (wt%)
Basalt
Trachyte
Reclassified Basalt
65KEA-1

Figure 7: Graphs showing major element data (wt%) against MgO (wt%) for published Hualalai post-shield lavas. Plot a) shows SiO_2 (wt%) against MgO (wt%), b) shows TiO_2 (wt%) against MgO (wt%), c) shows Al_2O_3 (wt%) against MgO (wt%), d) shows Fe_2O_3 (wt%) against MgO (wt%), e) shows FeO (wt%) against MgO (wt%), f) shows CaO (wt%) against MgO (wt%), g) shows MnO (wt%) against MgO (wt%), h) shows Na_2O (wt%) against MgO (wt%), i) shows K_2O (wt%) against MgO (wt%), j) shows P_2O_5 (wt%) against MgO (wt%). The post-shield volcanic whole rock data was downloaded from the GEOROC database (see full references from page 21). Black circles represent published data for basaltic post-shield lavas, orange diamonds represent published data for trachytic post-shield lavas, blue circles represent the data classified as post-shield trachytic lava on GEOROC, but which were reclassified as a basaltic lava in this thesis, and the yellow circle represents the post-shield basaltic lava chosen to represent the parental melt composition for the modelled major element path of fractional crystallisation (sample 65KEA-1 from Clague et al. (1980)).

For the MELTS model (Gualda *et al.*, 2012), an initial melt composition was selected from the published basaltic post-shield volcanic whole rock (VWR) data downloaded from the GEOROC database (https://georoc.eu/) on 6 October 2021, using the following parameters: geographical location = Hualalai; Hawaii: rock type = volcanic. The post-shield basaltic data found on GEOROC was compiled from published data (Macdonald, 1968; Schilling and Winchester, 1969; O'Nions et al., 1977; Anonymous, 1980; Clague et al., 1980; Clague, 1987; Moore and Clague, 1987; Moore *et al.*, 1987; Sobolev and Nikogosian, 1994; Sims *et al.*, 1995; Sims and Depaolo, 1997; Pickett and Murrell, 1997; Sims *et al.*, 1999; Stracke et al., 1999; Hanano *et al.*, 2010). The sample selected to represent the initial melt was required to be as primitive as possible, whilst still fitting the basaltic array from data downloaded from the GEOROC database from the published data mentioned above.

The sample highlighted yellow in figure 7 (sample 65KEA-1 from Clague et al. (1980)) was selected as the initial melt composition for the major element Solid Line of Descent model. It was selected as it represented a primitive (high MgO content) composition, whilst following the trend of the basalt array. The samples with the highest MgO content in these plots were not selected, as they did not fit the trend of the basaltic array, which indicated they may only appear primitive without being so. This could occur, for example, if these samples contained olivine phenocrysts which would increase the MgO content.

The major element composition of sample 65KEA-1 (Clague et al., (1980) was input into the MELTS program (Gualda *et al.*, 2012). The model was made to fractionate solids from the liquidus temperature to 1000°C in 2°C incremental steps. The MELTS models (Gualda *et al.*, 2012) were run unbuffered for oxygen fugacity, but with an initial Fe^{3+}/Fe_{total} ratio based on the published data for sample 65KEA-1 (Clague et al., (1980). This model was run for 3 different pressures: 1kbar, 5kbar and 9kbar.

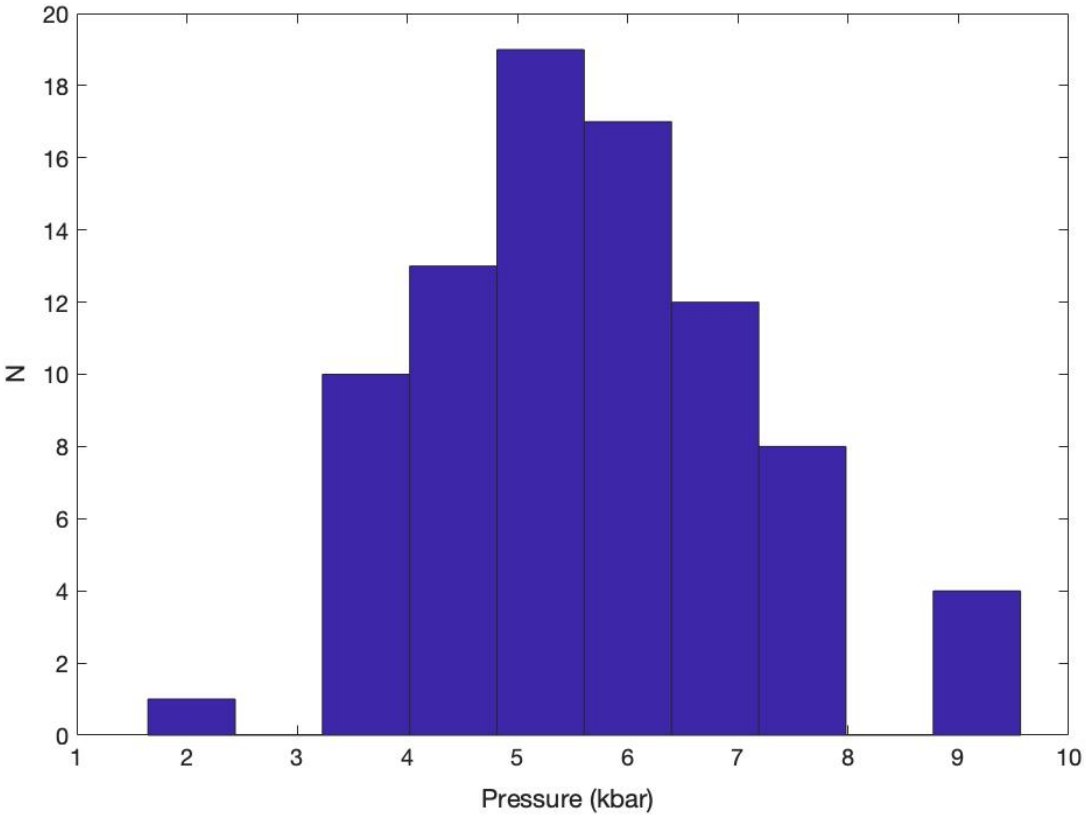

Figure 8: A histogram of the pressures of crystallisation for the locations sampled within samples H1, H3, H7, 101870, 81862, 106426, 101863, 81874 and 81869 (Gleeson et al., Unpublished Data). Pressures of clinopyroxene crystallisation were calculated by Gleeson et al. (Unpublished Data) using the clinopyroxene-only thermobarometer of Wang et al. (2021) (equation 1 was used for pressure). Calculations were performed using the Python3 package Thermobar (Wieser, Petrelli et al. 2022). This histogram shows that 5kbar is the most reasonable pressure to use in the model of the path of fractional crystallisation for a system

modelling the fractional crystallisation of the samples. Pressures of 1-2kbar and 9-10kbar are outliers.

From the histogram above, the 5kbar model was predicted to be the most appropriate for modelling the samples' path of fractional crystallisation. The 1kbar and 9kbar models (based on the highest and lowers pressures assigned to the data collected in this study) were run to test whether 5kbar model produced the best fit; the 'melts_liquid' output data for the three pressures from MELTS (Gualda *et al.*, 2012) were plotted on major element vs MgO plots alongside the published post-shield volcanic whole rock basaltic data and were compared for their ability to model this published basaltic array.

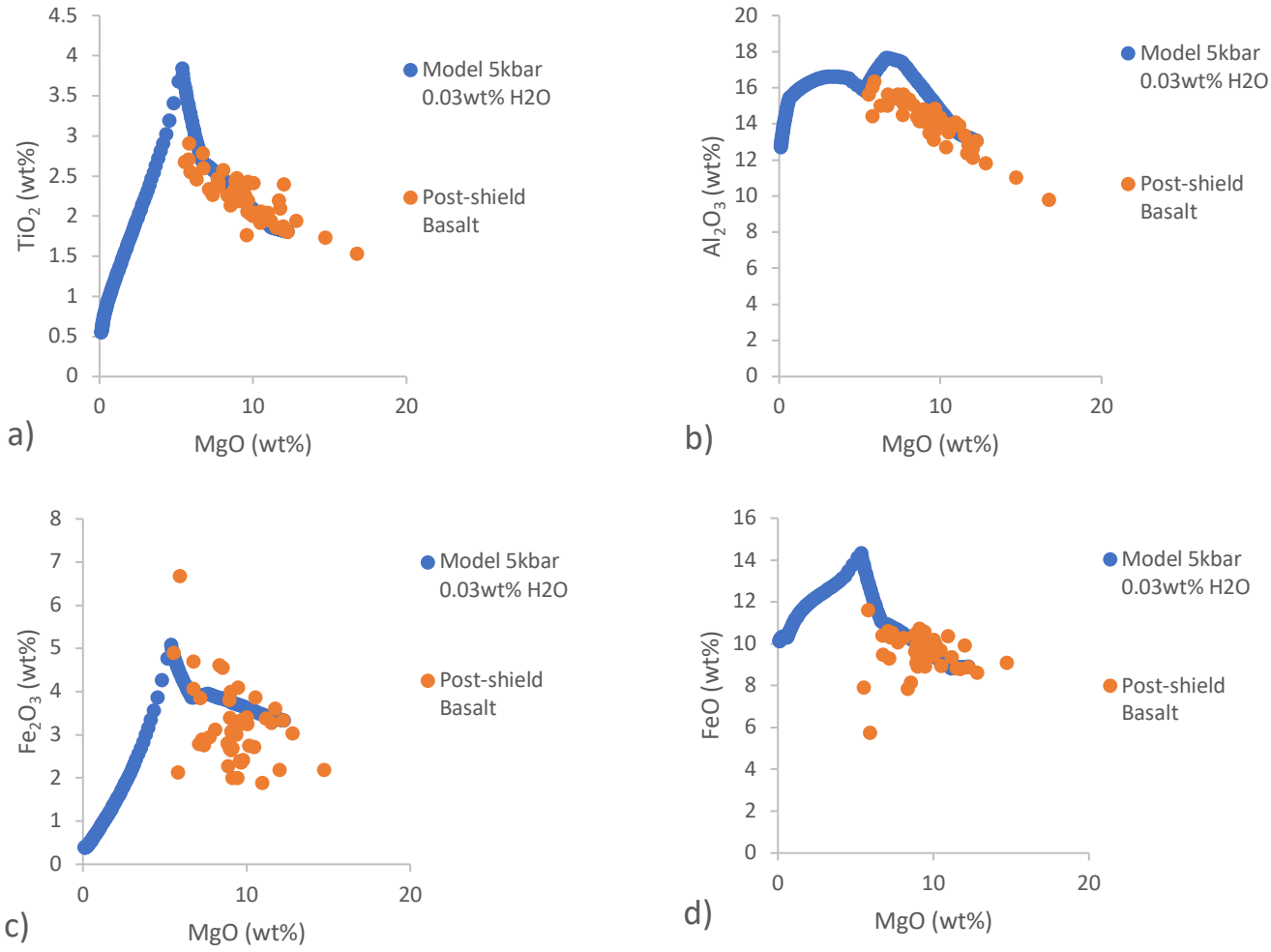

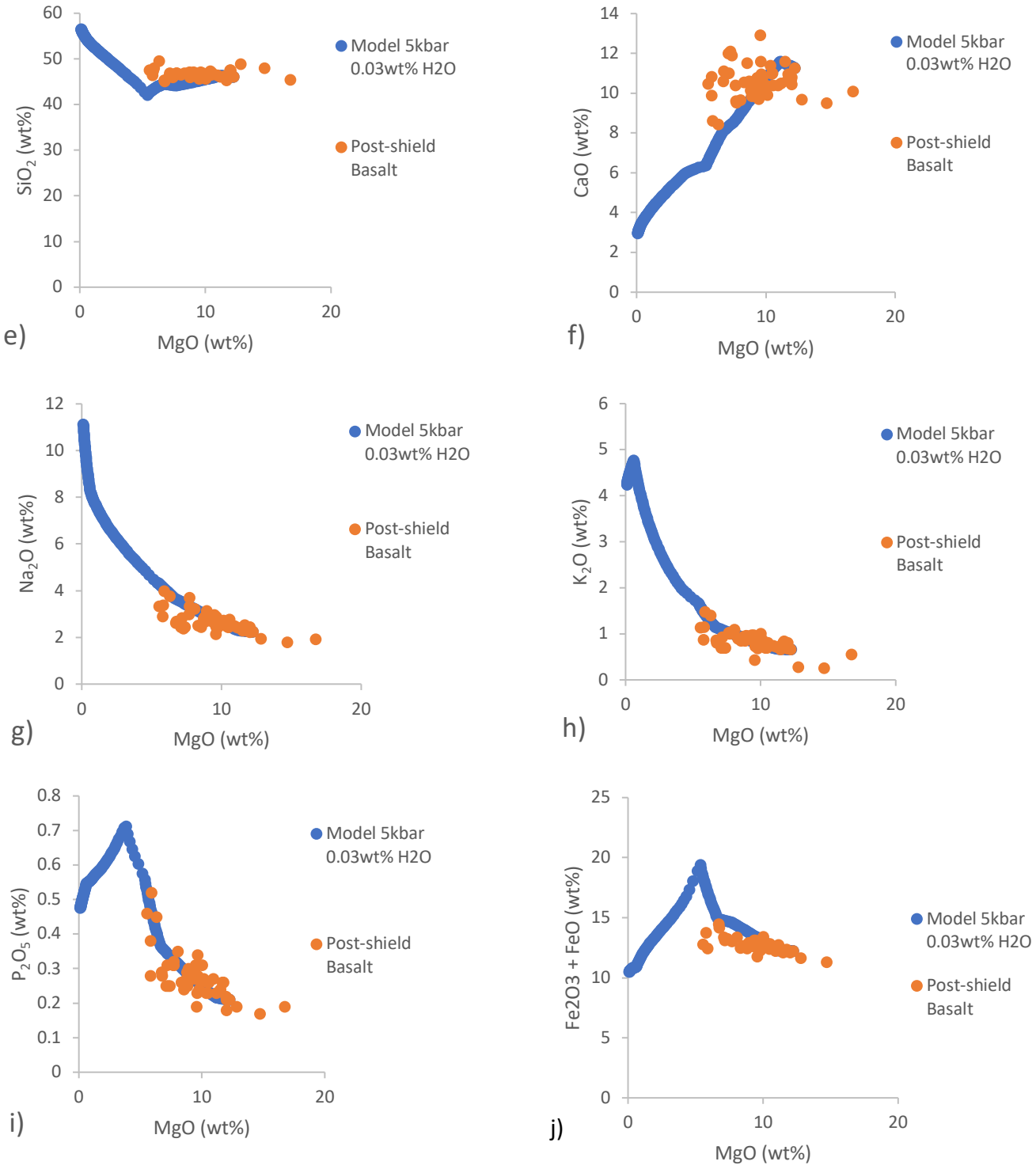

Figure 9: Plots of major elements (wt%) against MgO (wt%) showing the modelled path of crystal fractionation for a pressure of 5kbar, water content of 0.03wt% and initial melt composition given by sample 65KEA-1 (Clague et al., (1980)) produced using MELTS (Gualda et al., 2012), alongside published post-shield basaltic data downloaded from the GEOROC

database (see full references from page 24). Plot a) shows TiO_2 (wt%) against MgO (wt%), b) shows Al_2O_3 (wt%) against MgO (wt%), c) shows Fe_2O_3 (wt%) against MgO (wt%), d) shows FeO (wt%) against MgO (wt%), e) shows SiO_2 (wt%) against MgO (wt%), f) shows CaO (wt%) against MgO (wt%), g) shows Na_2O (wt%) against MgO (wt%), h) shows K_2O (wt%) against MgO (wt%), i) shows P_2O_5 (wt%) against MgO (wt%) and j) shows Fe_2O_3 + FeO (wt%) against MgO (wt%). Blue circles represent data output from the MELTs model (Gualda et al., 2012), and orange circles represent published post-shield basaltic data downloaded from GEOROC.

The output of the MELTS model (Gualda et al., 2012) at 5kbar and 0.03wt% water content are shown in table 2. Table 2 shows the temperatures that each phase crystallises at between 1316°C and 1000°C.

Crystalline Phase	Temperature crystallisation begins (°C)	Temperature crystallisation ends (°C)
Olivine	1314	1284
	1168	1166
	1156	1000
Clinopyroxene	1284	1000
Orthopyroxene	1224	1168
	1164	1156
Spinel	1220	1170
	1164	1000
Plagioclase	1208	1166
	1158	1000
Whitlockite	1150	1000
Leucite	1066	1000

Table 2: A table showing the output of the MELTS model (Gualda et al., 2012) run at a pressure of 5kbar, water content of 0.03wt% and initial melt composition given by sample

65KEA-1 (Clague et al., (1980)). The table shows the temperatures at which each phase begins to crystallise and ceases to crystallise. These phases include olivine, clinopyroxene, orthopyroxene, spinel, plagioclase, whitlockite and leucite.

Neither of the three models (at 1kbar, 5kbar and 9kbar) using sample 65KEA-1's (Clague et al., (1980) recorded H_2OM water content of 0.03 wt% produced an appropriate fit or a reasonable looking path of fractional crystallisation. A water content (H_2OM) of 0.03wt% for Hawaiian rocks, however, is unreasonably low, when considering published data on Hawaiian rocks' water content (Wieser, Edmonds et al., 2022). Published studies suggest that 0.5 wt% is a reasonable value for water content in Hawaiian rocks (Wieser, Edmonds et al., 2022). The model was therefore re-run with a water content of 0.5 wt%, but otherwise still using the major element composition of sample 65KEA-1 (Clague, Jackson and Wright, (1980).

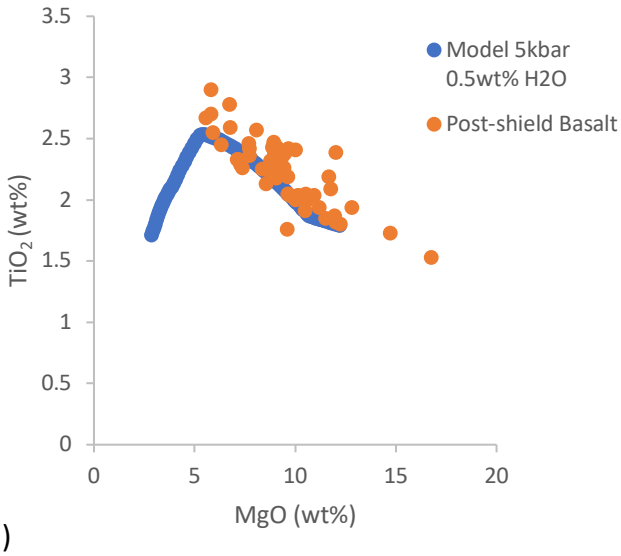

a)

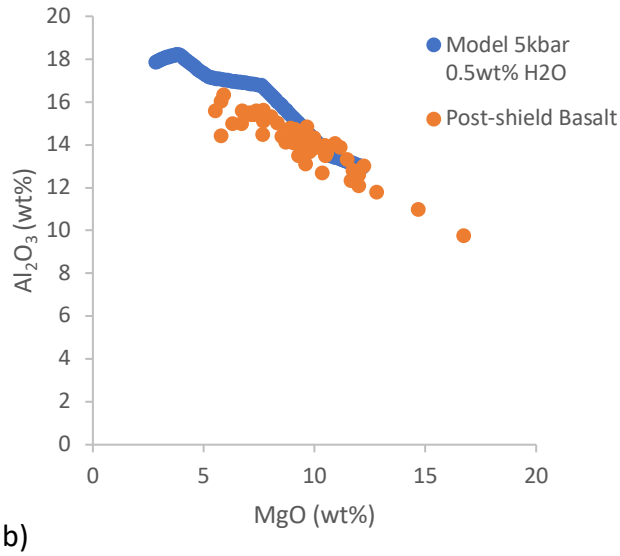

b)

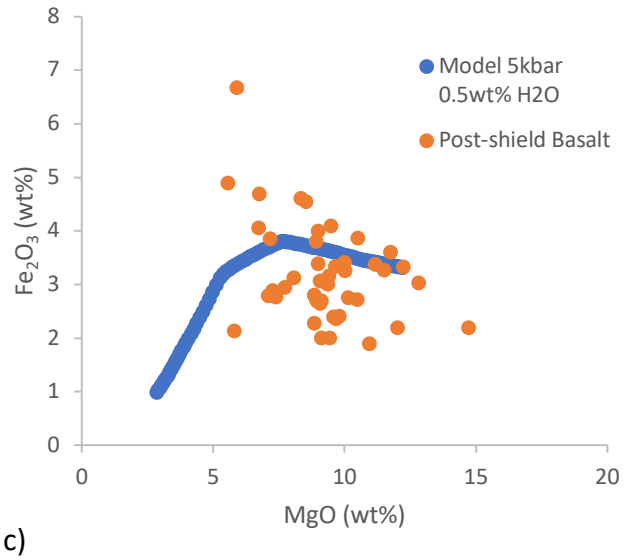
Model 5kbar
0.5wt% H2O
Post-shield Basalt
Fe2O3 (wt%)
MgO (wt%)

c)

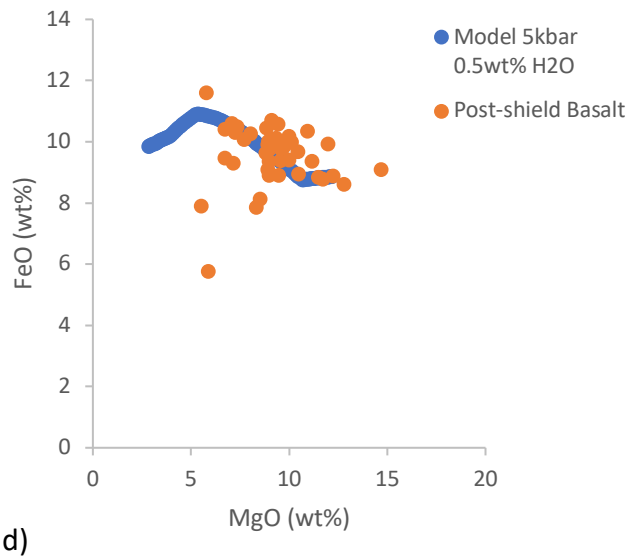
Model 5kbar
0.5wt% H2O
Post-shield Basalt
FeO (wt%)
MgO (wt%)

d)

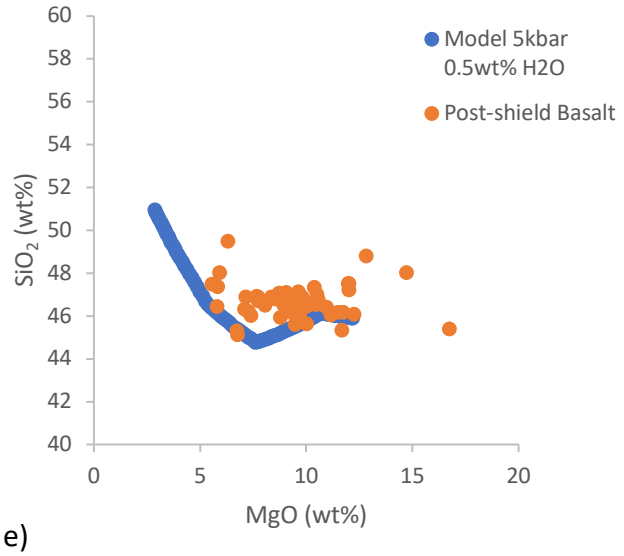
Model 5kbar
0.5wt% H2O
Post-shield Basalt
SiO2 (wt%)
MgO (wt%)

e)

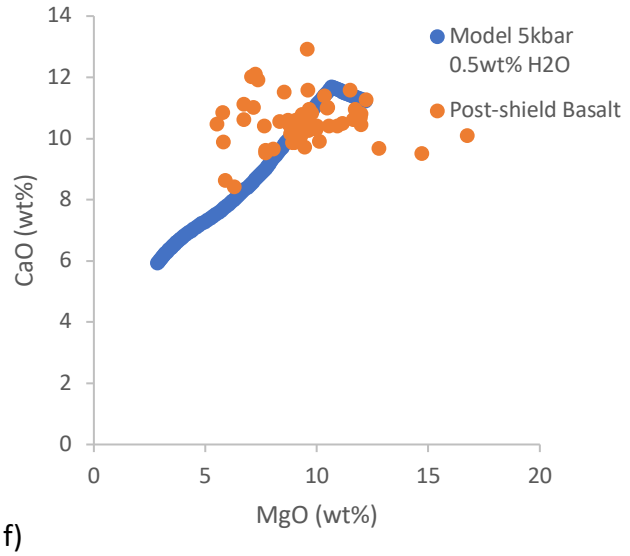
Model 5kbar
0.5wt% H2O
Post-shield Basalt
CaO (wt%)
MgO (wt%)

f)

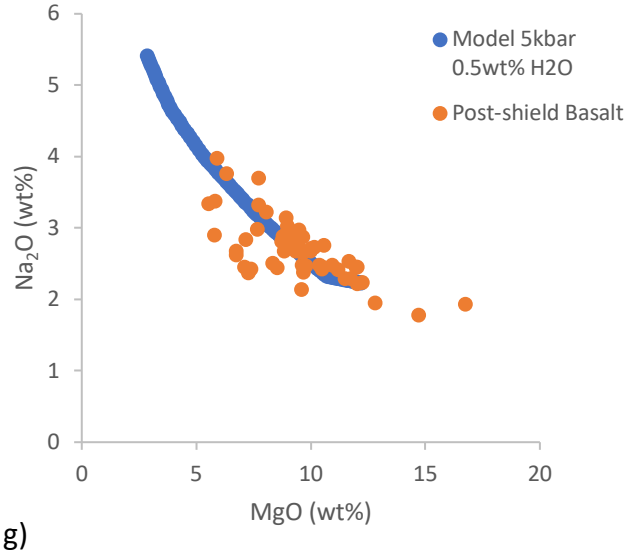
Model 5kbar
0.5wt% H2O
Post-shield Basalt
Na2O (wt%)
MgO (wt%)

g)

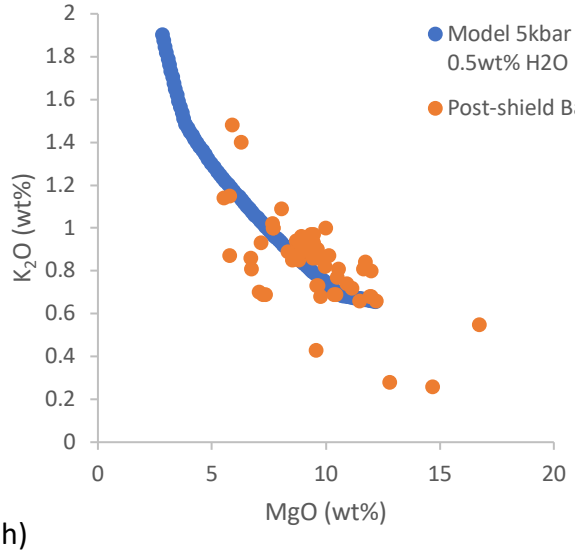
Model 5kbar
0.5wt% H2O
Post-shield Basalt
K2O (wt%)
MgO (wt%)

h)

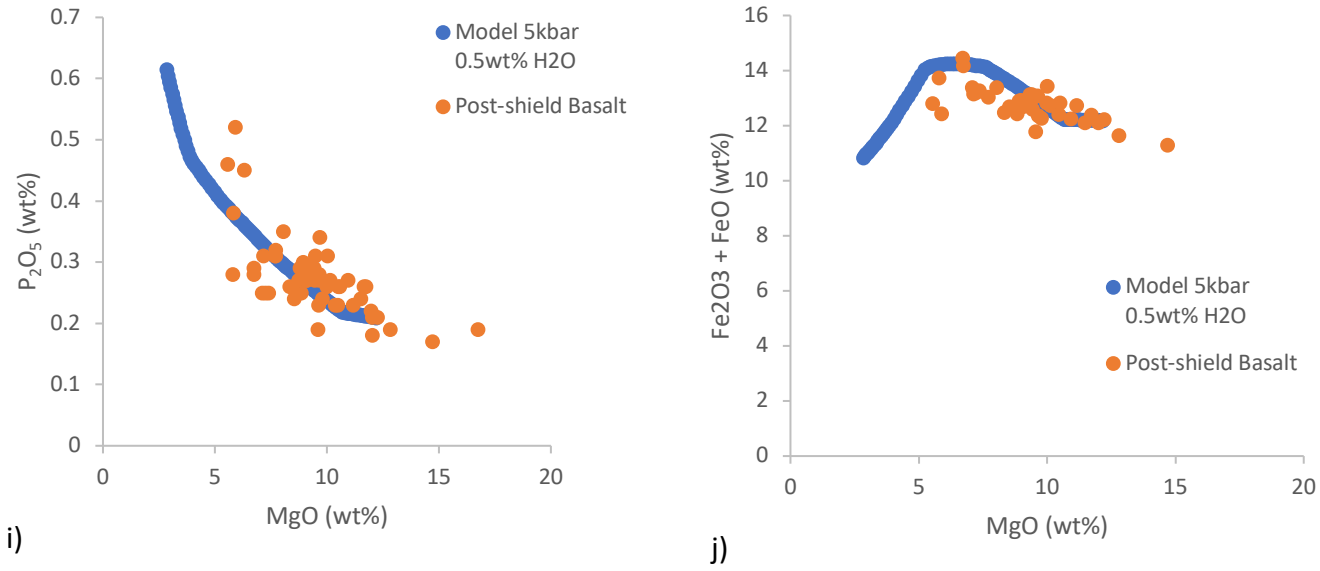

Figure 10: Plots of major elements (wt%) against MgO (wt%) showing the modelled path of crystal fractionation for a pressure of 5kbar, water content of 0.5wt% and initial melt composition given by sample 65KEA-1 (Clague, Jackson and Wright, (1980) produced using MELTS (Gualda et al., 2012), alongside published post-shield basaltic data downloaded from the GEOROC database (see full references from page 24). Plot a) shows TiO_2 (wt%) against MgO (wt%), b) shows Al_2O_3 (wt%) against MgO (wt%), c) shows Fe_2O_3 (wt%) against MgO (wt%), d) shows FeO (wt%) against MgO (wt%), e) shows SiO_2 (wt%) against MgO (wt%), f) shows CaO (wt%) against MgO (wt%), g) shows Na_2O (wt%) against MgO (wt%), h) shows K_2O (wt%) against MgO (wt%), i) shows P_2O_5 (wt%) against MgO (wt%) and j) shows Fe_2O_3 + FeO (wt%) against MgO (wt%). Blue circles represent data output from the MELTs model (Gualda et al., 2012), and orange circles represent published post-shield basaltic data downloaded from GEOROC.

The output of the MELTS model (Gualda et al., 2012) at 5kbar and 0.5wt% water content are shown in table 3. Table 3 shows the temperatures that each phase crystallises at between 1308°C and 1000°C.

Crystalline Phase	Temperature crystallisation begins (°C)	Temperature crystallisation ends (°C)
Olivine	1306	1190
	1070	1000
Clinopyroxene	1262	1070
Spinel	1190	1000
Orthopyroxene	1174	1080
Plagioclase	1130	1000
Apatite	1080	1000
Rhombohedral Oxide	1032	1000

Table 3: A table showing the output of the MELTS model (Gualda et al., 2012) run at a pressure of 5kbar, water content of 0.5wt% and initial melt composition given by sample 65KEA-1 (Clague et al., (1980)). The table shows the temperatures at which each phase begins to crystallise and ceases to crystallise. These phases include olivine, clinopyroxene, orthopyroxene, spinel, plagioclase, apatite and Rhombohedral Oxide.

This model produces a reasonable fit at 5kbar and 0.5wt% water content. The MELTS (Gualda et al., 2012) clinopyroxene output was used to plot a model of the fractional crystallisation path for clinopyroxene in figure 21.

3.2 MELTS Trace Element Model

The initial melt major element composition for the trace element fractional crystallisation model was selected from published post-shield basaltic whole rock lava data downloaded from the GEOROC database (see full references from page 24). The sample selected, sample 65KEA-1 from Clague et al. (1980), is the most primitive whilst still reflecting the trend of the basaltic array on a Y vs MgO plot (see fig. 11).

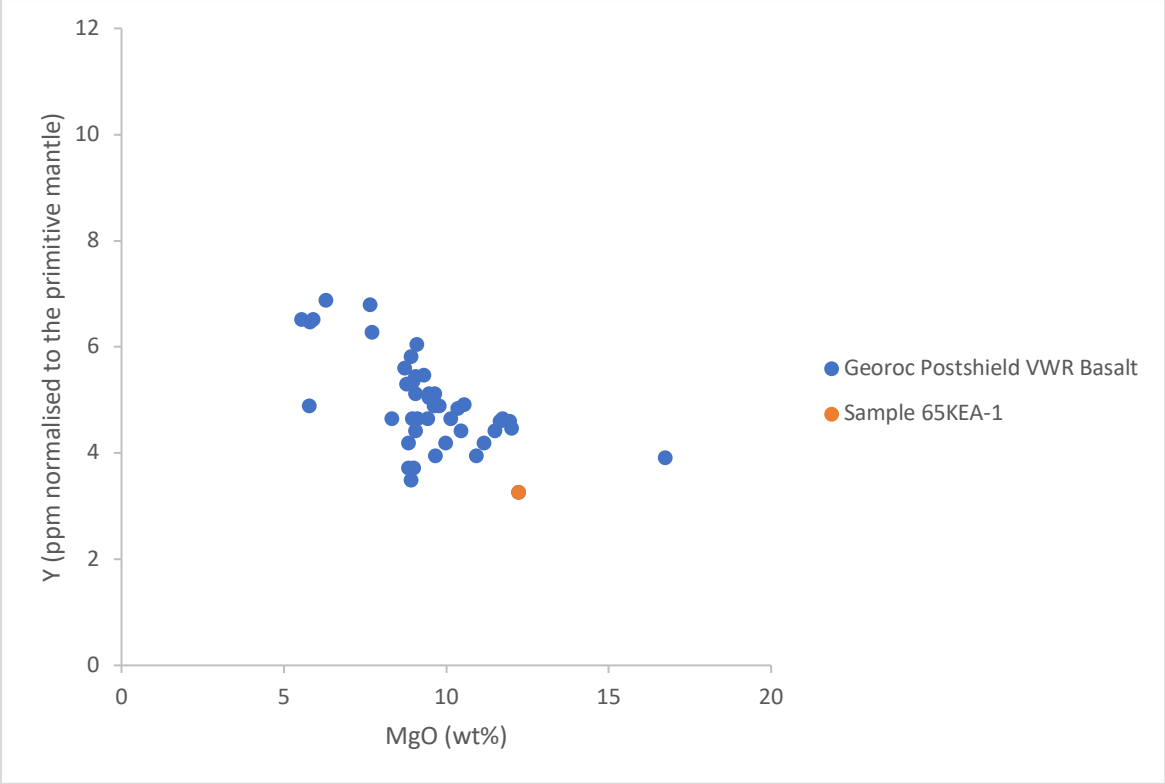

Figure 11: Graph showing the concentration of Y (ppm) against MgO (wt%) for published Hualalai post-shield basaltic lavas. The post-shield basaltic whole rock data was downloaded from the GEOROC database (see full references from page 24). Blue circles represent published data for basaltic post-shield lavas, and the orange circle represents the post-shield basaltic lava chosen to represent the parental melt composition for the modelled trace element path of fractional crystallisation (sample 65KEA-1 from Clague et al. (1980)). Trace element data was normalised to the primitive mantle using primitive mantle values given by McDonough and Sun (1995).

The major element composition of sample 65KEA-1 from Clague et al. (1980) with a water content of 0.5wt% and a pressure of 5kbar (for the reasons outlined above) was input into the MELTS software (Gualda et al., 2012) to produce a major element model for the path of fractional crystallisation. The major element output data from MELTS (Gualda et al., 2012) was then used to create a trace element path fractional crystallisation model using partition coefficients calculated based on work by Bédard (2001).

To calculate the trace element composition of crystals produced by fractional crystallisation, an initial melt trace element composition was chosen, based on the composition of sample 02AHU-4 (from Hanano *et al.* (2010)). The trace element composition of the melt phase was then tracked through fractional crystallisation using the mass fraction of melt remaining at each step and a bulk partition coefficient for each element determined using the system temperature and the proportions of the different solid phases. Calculated partition coefficients for each phase also allowed the trace element composition of each phase at each temperature interval to be determined.

The trace element data for sample 65KEA-1 from Clague et al. (1980) is limited, so the initial melt trace element composition for the trace element fractional crystallisation model was selected from published post-shield basaltic whole rock lava data downloaded from the GEOROC database (see full references from page 24). The sample selected, 02AHU-4 (from Hanano *et al.* (2010)), was chosen on the basis of being the most primitive whilst still reflecting the trend of the basaltic array on La vs MgO and Y vs MgO plots (see fig. 12).

The trace element composition for 02AHU-4 (from Hanano *et al.* (2010) was normalised to the primitive mantle and input as the initial melt trace element composition for the trace element fractional crystallisation model.

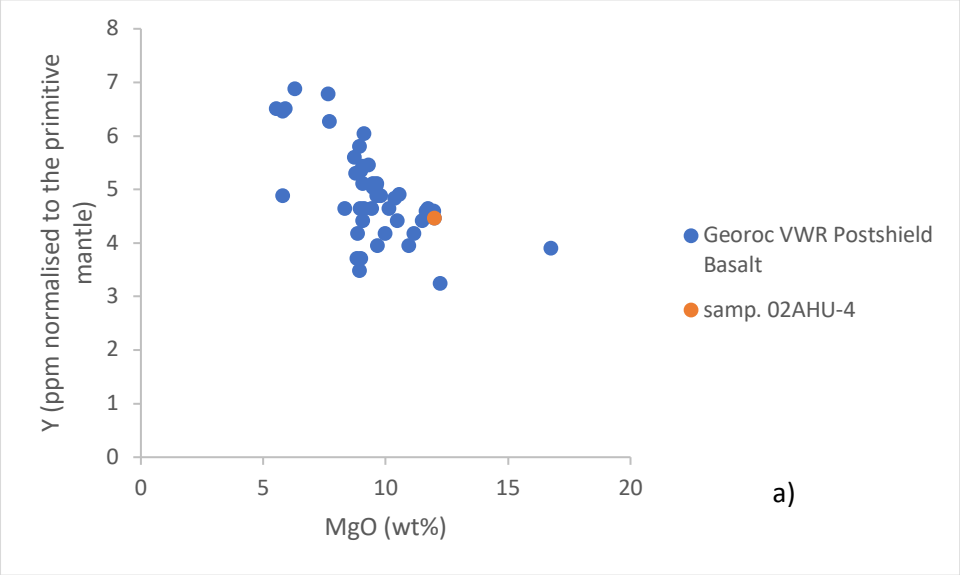

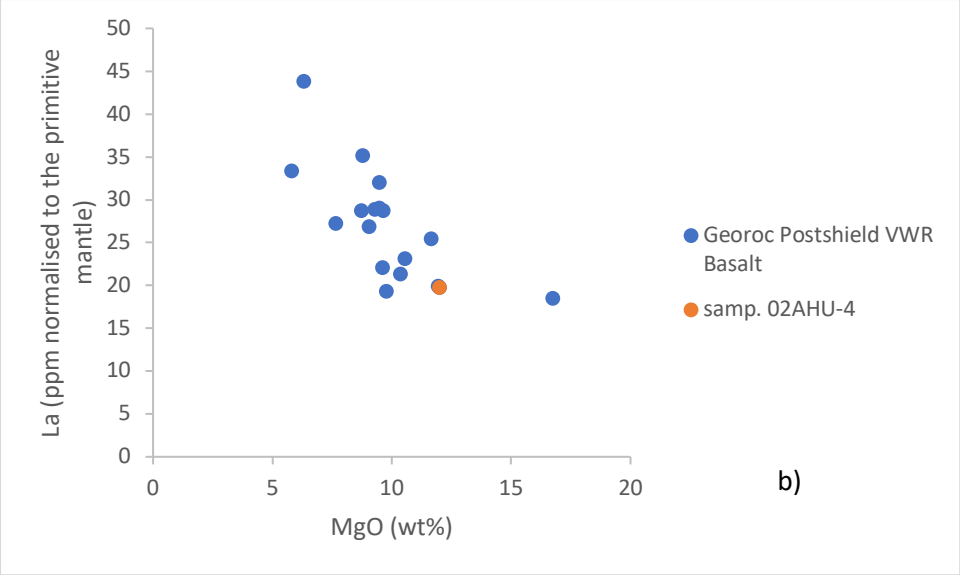

Figure 12: Graphs showing trace element concentration (ppm) against MgO (wt%) for published Hualalai post-shield basaltic lavas. Plot a) shows Y (ppm) against MgO (wt%) and b) shows La (ppm) against MgO (wt%). The post-shield basaltic whole rock data was downloaded from the GEOROC database (see full references from page 24). Blue circles represent published data for basaltic post-shield lavas, and the orange circle represents the post-shield basaltic lava chosen to represent the parental melt composition for the modelled major element path of fractional crystallisation, 02AHU-4 (from Hanano et al. (2010)) . Trace element data was normalised to the primitive mantle using primitive mantle values given by McDonough and Sun (1995).

3.3 Zone Refining Trend

The direction of crystal dissolution-reaction was modelled using a 'zone refining trend', calculated using the equation from Harris (1957):

$$\frac{C_L}{C_0} = \frac{1}{D} - \left(\frac{1}{D} - 1\right) e^{(-DI)}$$

C_L represents the concentration of an element in the liquid after zone refining, C_0 represents the initial concentration of the element in the liquid, D is the partition coefficient, and I is the number of reactive flow cycles modelled (Johan, 2016). The initial concentration of each element was taken from the trace element composition of sample 02AHU-4 (from Hanano

et al. (2010)), normalised to the primitive mantle. The D values used were the bulk partition coefficients of the total cumulate for each element at 1201°C calculated using Bedard (2001). I was varied from 0 to 2.38 in increments of 0.01. The data for this model can be found in the appendices (see appendix 8.28), and has been plotted in figure 49.

4. Results

4.1 Sample Description

The Hawaiian samples analysed in this study consist of four wehrlites (H1, H3, H7 and 101870), four gabbros (106426, 101863, 81869, 81874) and one dunite (81862). Samples 101870, 81862, 81869, 81874, 101863 and 106426 are xenoliths which were kindly loaned to Dr Matthew Gleeson from the Harker Petrology Collection at the Sedgwick Museum, Cambridge. These samples were erupted in the 1801 Kaupulehu flow of Hualalai, Hawaii, and were collected by E. Ingerson (81862, 81869 and 81874) and C. E. Tilley (101863 and 101870). The collector of sample 106426 is unrecorded. Samples H1, H3 and H7 were kindly donated by Dr Sarah Lambart from the University of Utah. These samples are xenoliths interpreted to represent magma chamber cumulates (Bohrson and Clague, 1988; Chen, Presnall and Stern, 1992) erupted from the 1801 Kaupulehu flow of Hualalai and collected from the Hualalai volcano, Big Island, Hawaii, by Dr Sarah Lambart.

From studying background corrected count rates for each element of each sample (exported from AZtec) using the open-source software 'QACD-quack' © 2019 by Matthew Loocke downloaded from *https://mloocke.wixsite.com/qacd-quack* on 20 June 2022 (Loocke, 2016), primary mineral proportions were calculated for each sample (Table 4). Wehrlitic samples ranged from 28.5% to 88.1% olivine and from 11.9% to 71.5% clinopyroxene. Gabbroic samples ranged from 4.7% to 61.6% olivine, from 5.2% to 53.5% clinopyroxene and from 28.4% to 89.1% plagioclase. The dunite sample was composed of 92.9% olivine and 7.1% clinopyroxene. Most samples also contained accessory minerals, including oxide phases (spinel and magnetite), though these accounted for <1% of the total mineralogy.

Sample	Lithology	Olivine (%)	Clinopyroxene (%)	Plagioclase (%)
H1	Wehrlite	43.2	56.8	0
H7	Wehrlite	28.5	71.5	0
H3	Wehrlite	77.4	22.5	0
101870	Wehrlite	88.1	11.9	0
81862	Dunite	92.9	7.1	0
106426	Gabbro	7.0	53.5	39.6
101863	Gabbro	5.7	5.2	89.1
81874	Gabbro	61.6	10.0	28.4
81869	Gabbro	4.7	39.0	56.3

Table 4: Mineral proportions of the primary mineral in the samples calculated via cluster analysis using the software 'QACD-quack' © 2019 by Matthew Loocke downloaded from *https://mloocke.wixsite.com/qacd-quack* on 20 June 2022 (Loocke, 2016).

Major element maps (Figures 13 to 21), produced during this project and provided by Dr Matthew Gleeson, reveal the details of the petrography and major element variability of each sample. These element maps were created in AZtec and have been edited to include the locations sampled for major element, trace element and/or isotopic analysis.

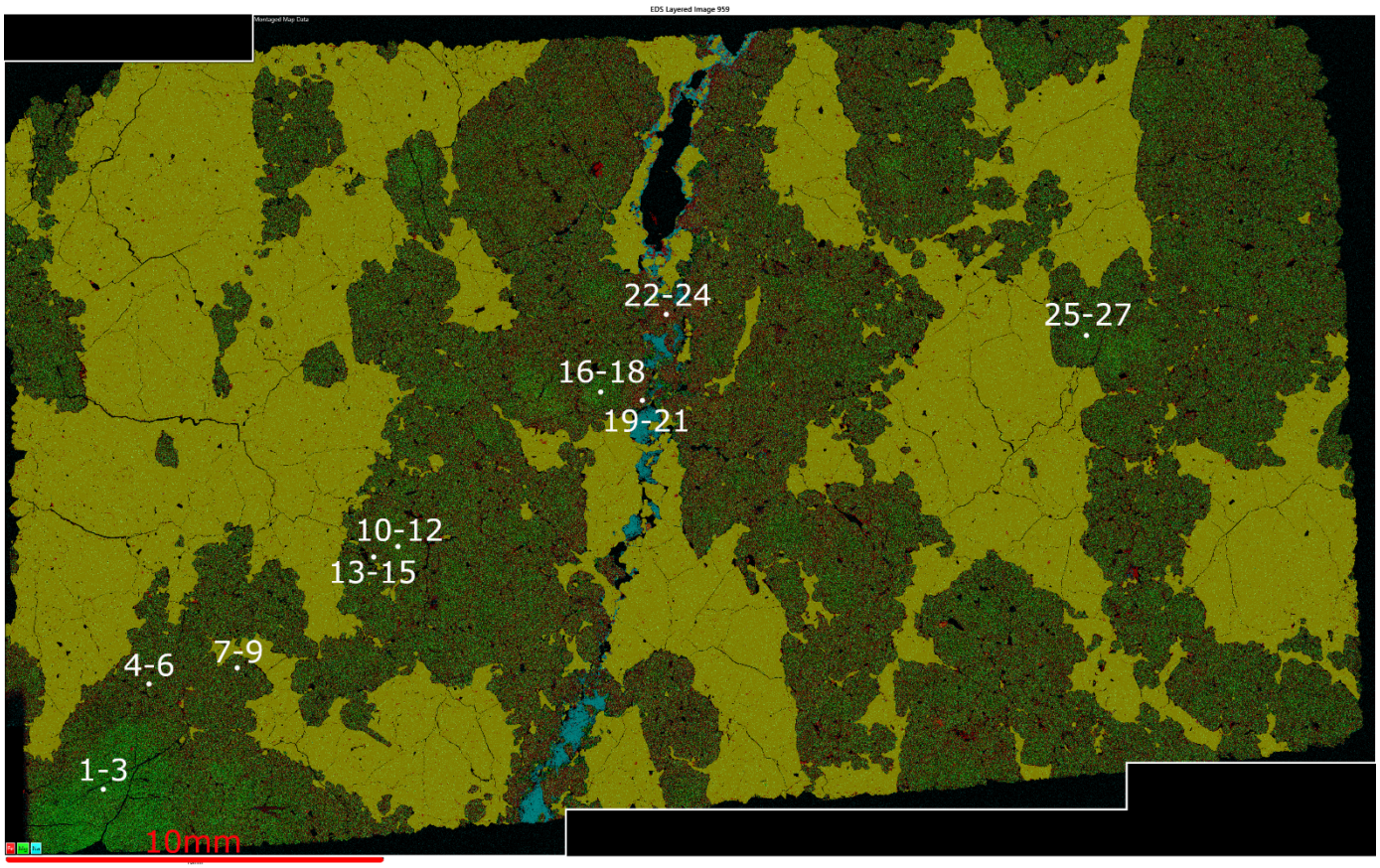

Figure 13: Major element map for sample H1 provided by Dr Matthew Gleeson. Labelled locations are the locations targeted for major element, trace element and/or isotopic analysis. The bar on the bottom left shows the scale of the map. Fe was mapped in red, Mg in green and Na in blue. Yellow regions of the map are olivine, and green/brown areas are clinopyroxene.

Sample H1 shows clear zonation within the clinopyroxene crystals. Core 1-3 (Figure 13) in particular looks distinctive relative to other regions of clinopyroxenes and other cores.

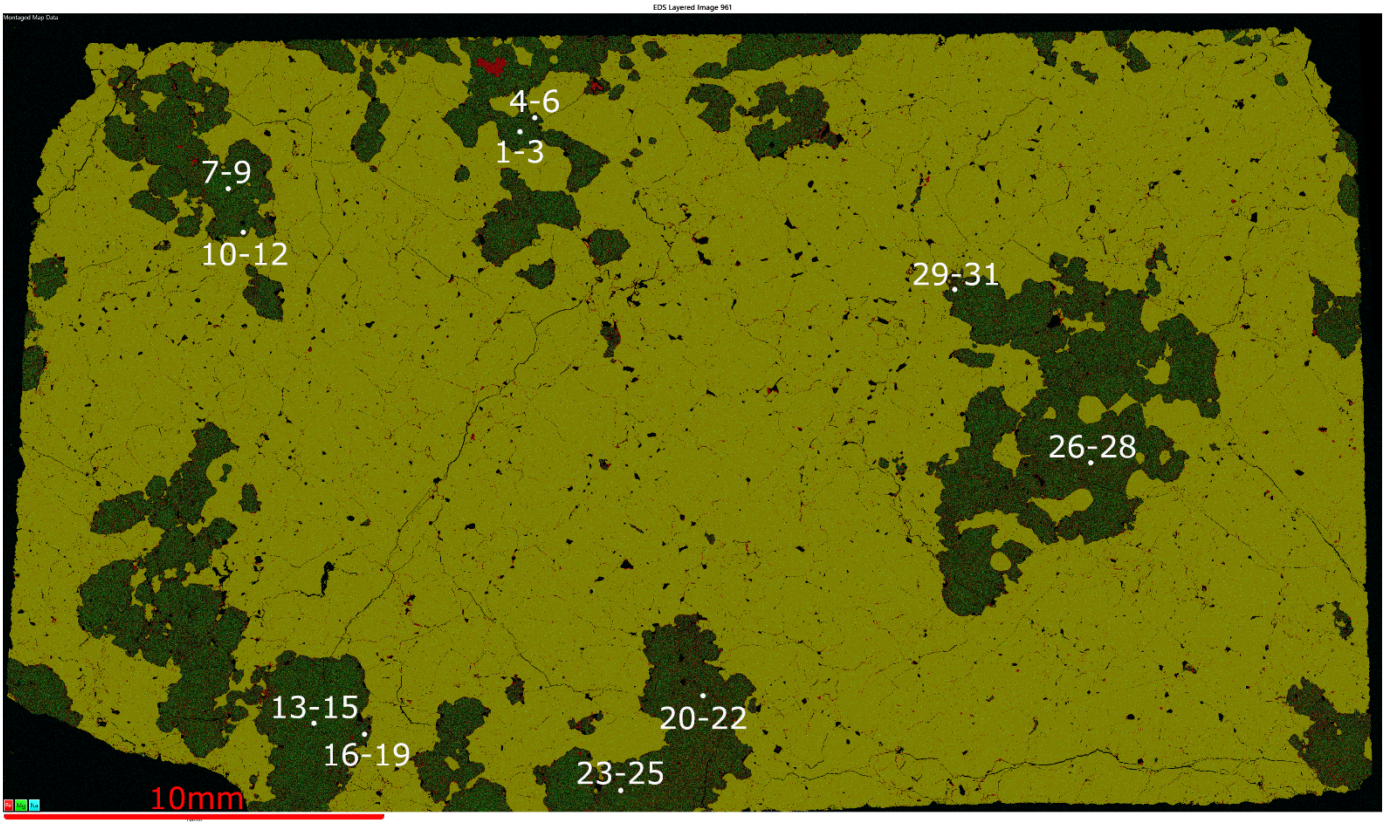

Figure 14: Major element map for sample H3 provided by Dr Matthew Gleeson. Labelled locations are the locations targeted for major element, trace element and/or isotopic analysis. The bar on the bottom left shows the scale of the map. Fe was mapped in red, Mg in green and Na in blue. Yellow regions of the map are olivine, and green areas are clinopyroxene.

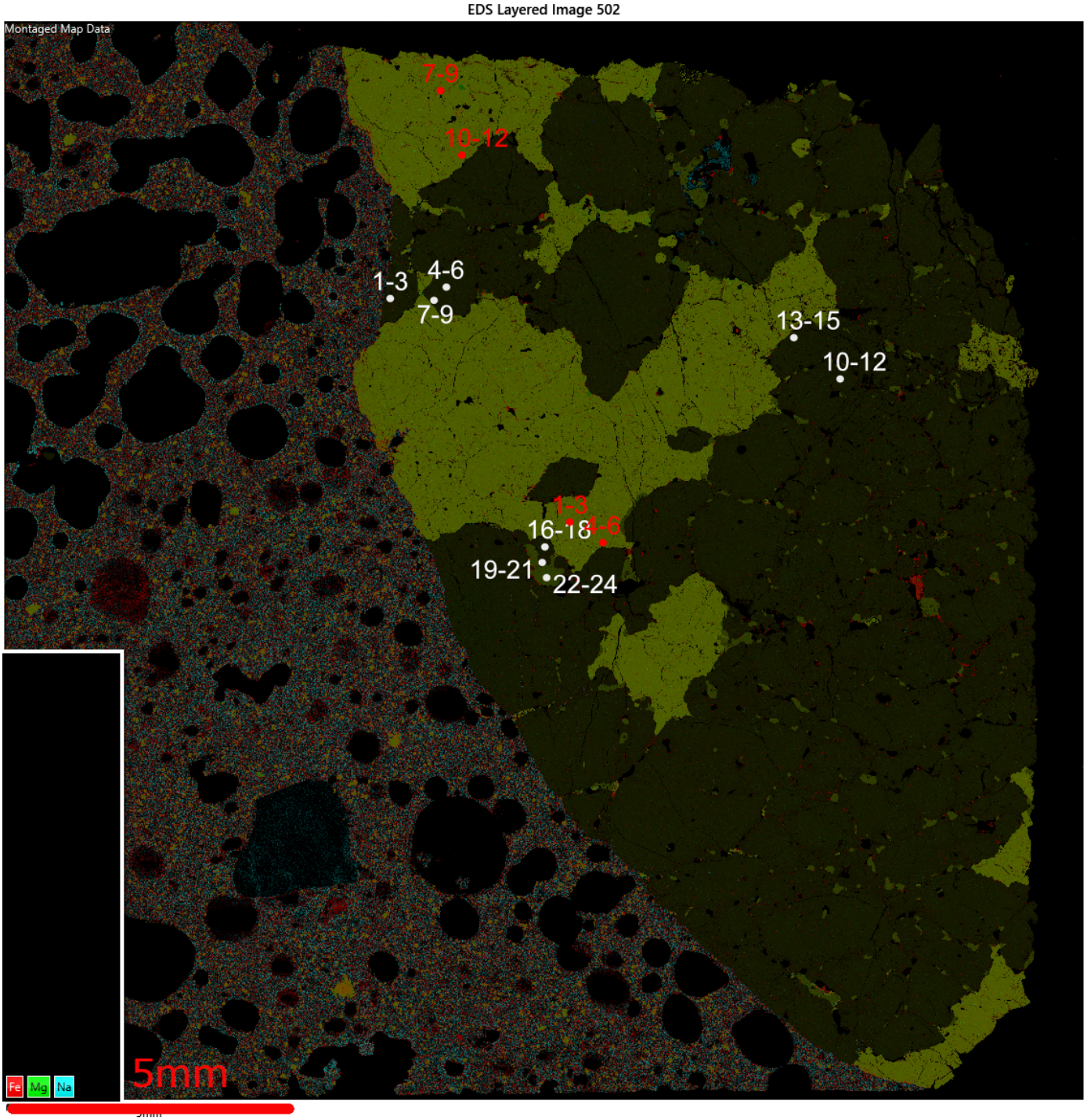

Figure 15: Major element map for sample H7 provided by Dr Matthew Gleeson. Labelled locations are the locations targeted for major element, trace element and/or isotopic analysis. The bar on the bottom left shows the scale of the map. Fe was mapped in red, Mg in green and Na in blue. Yellow regions of the map are olivine, and dark green areas are clinopyroxene.

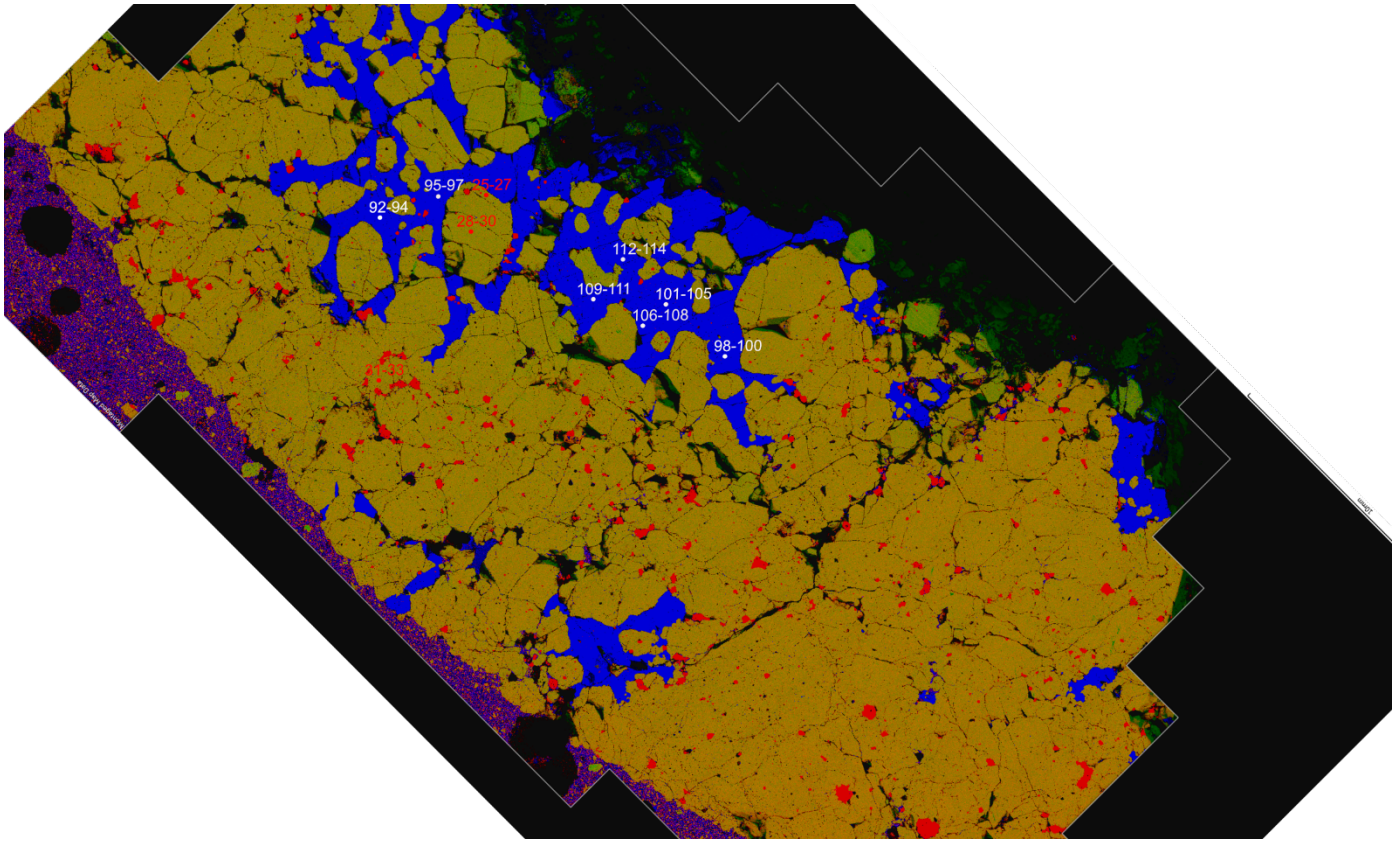

Figure 16: Major element map for sample 101870. Labelled locations are the locations targeted for major element, trace element and/or isotopic analysis. Yellow regions of the map are olivine, and blue areas are clinopyroxene.

Sample 101870 (figure 16) shows that the clinopyroxene-olivine borders do not form straight crystalline wall shapes, rather undulating borders, indicative of a dissolution front.

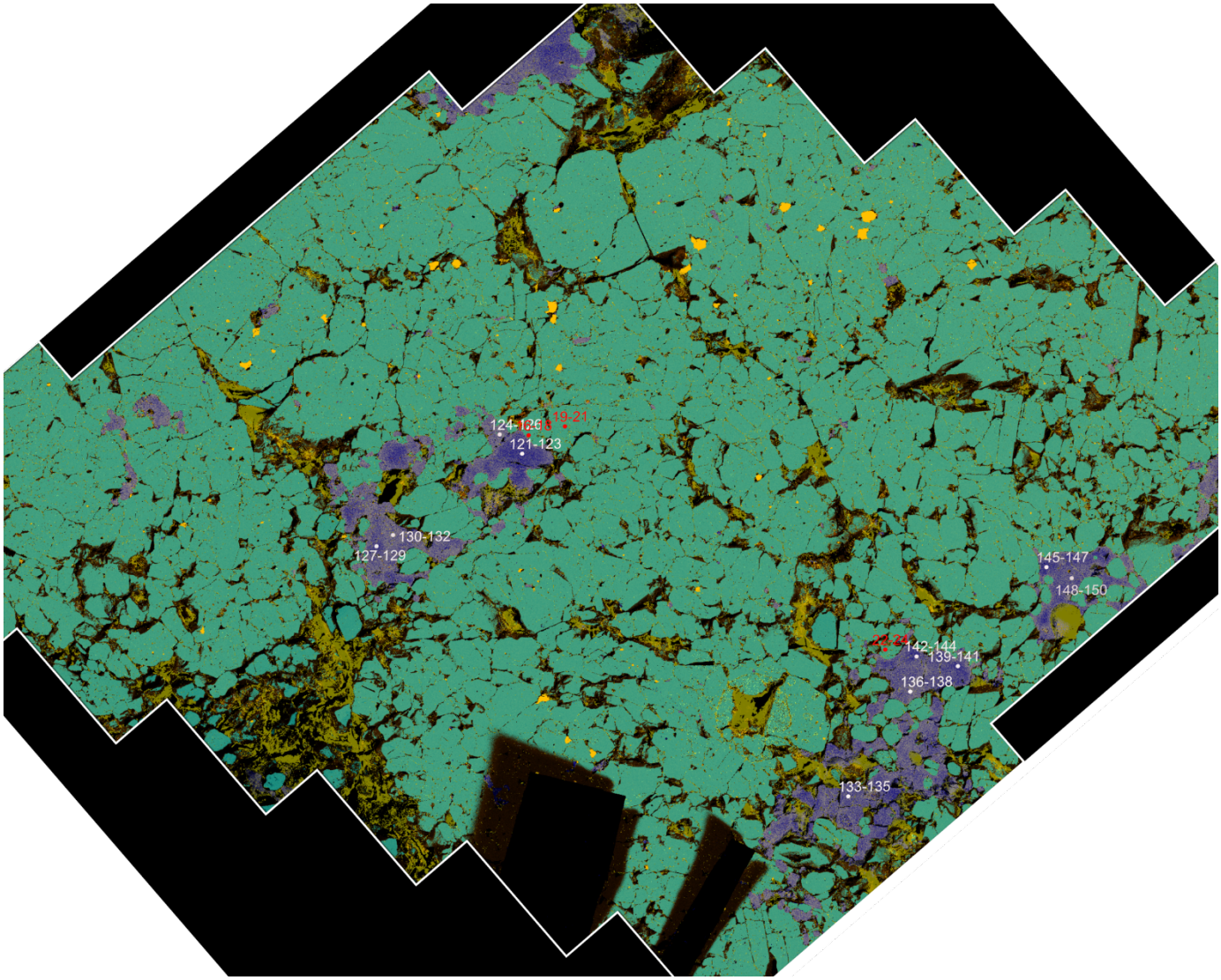

Figure 17: Major element map for sample 81862. Labelled locations are the locations targeted for major element, trace element and/or isotopic analysis. Green regions of the map are olivine, and blue/purple areas are clinopyroxene.

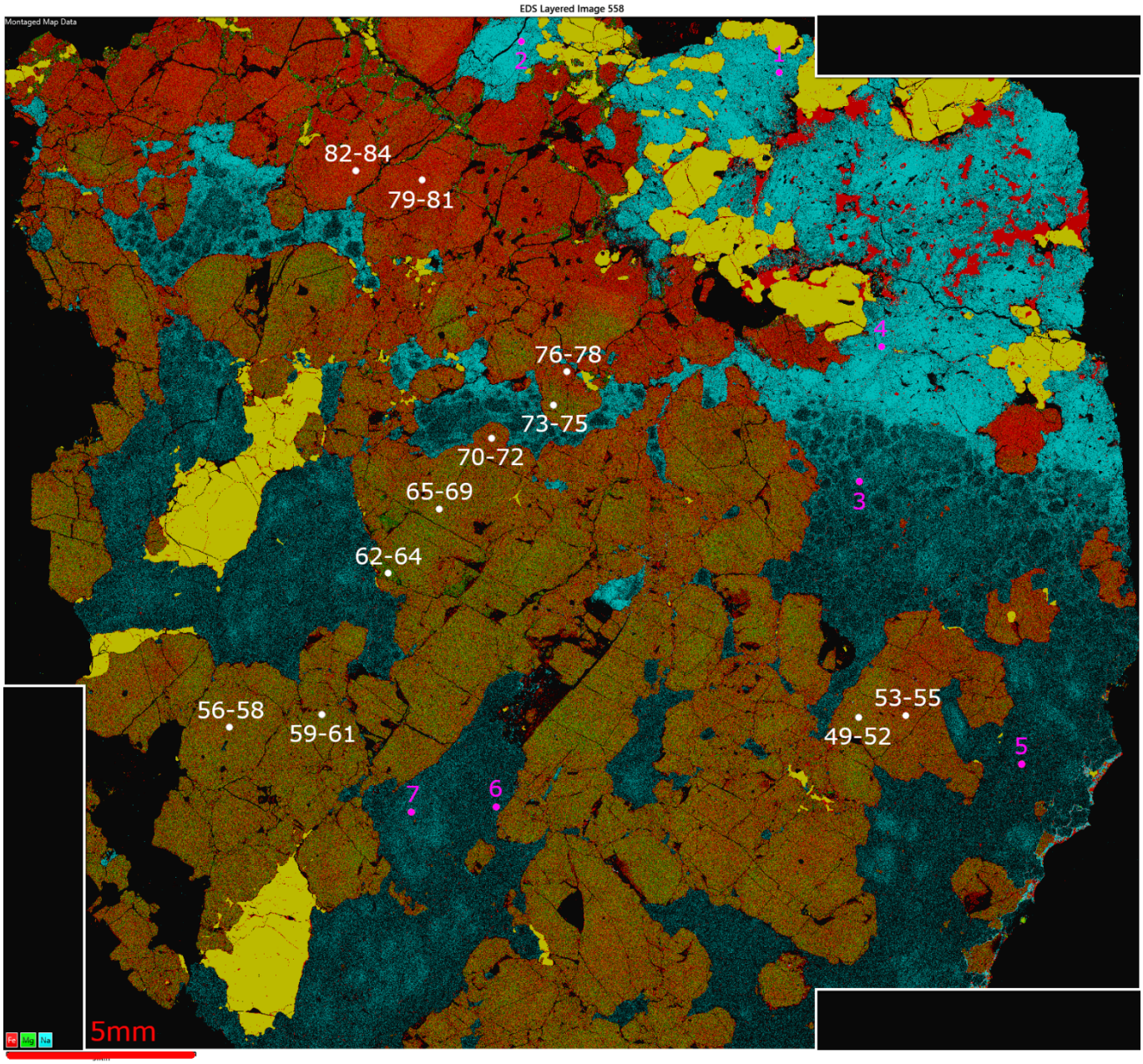

Figure 18: Major element map for sample 106426 provided by Dr Matthew Gleeson. Labelled locations are the locations targeted for major element, trace element and/or isotopic analysis. The bar on the bottom left shows the scale of the map. Fe was mapped in red, Mg in green and Na in blue. Yellow regions of the map are olivine, green/brown areas are clinopyroxene and blue areas are plagioclase.

Sample 106426 (figure 18) has a sharp compositional divide between the top and bottom of the sample.

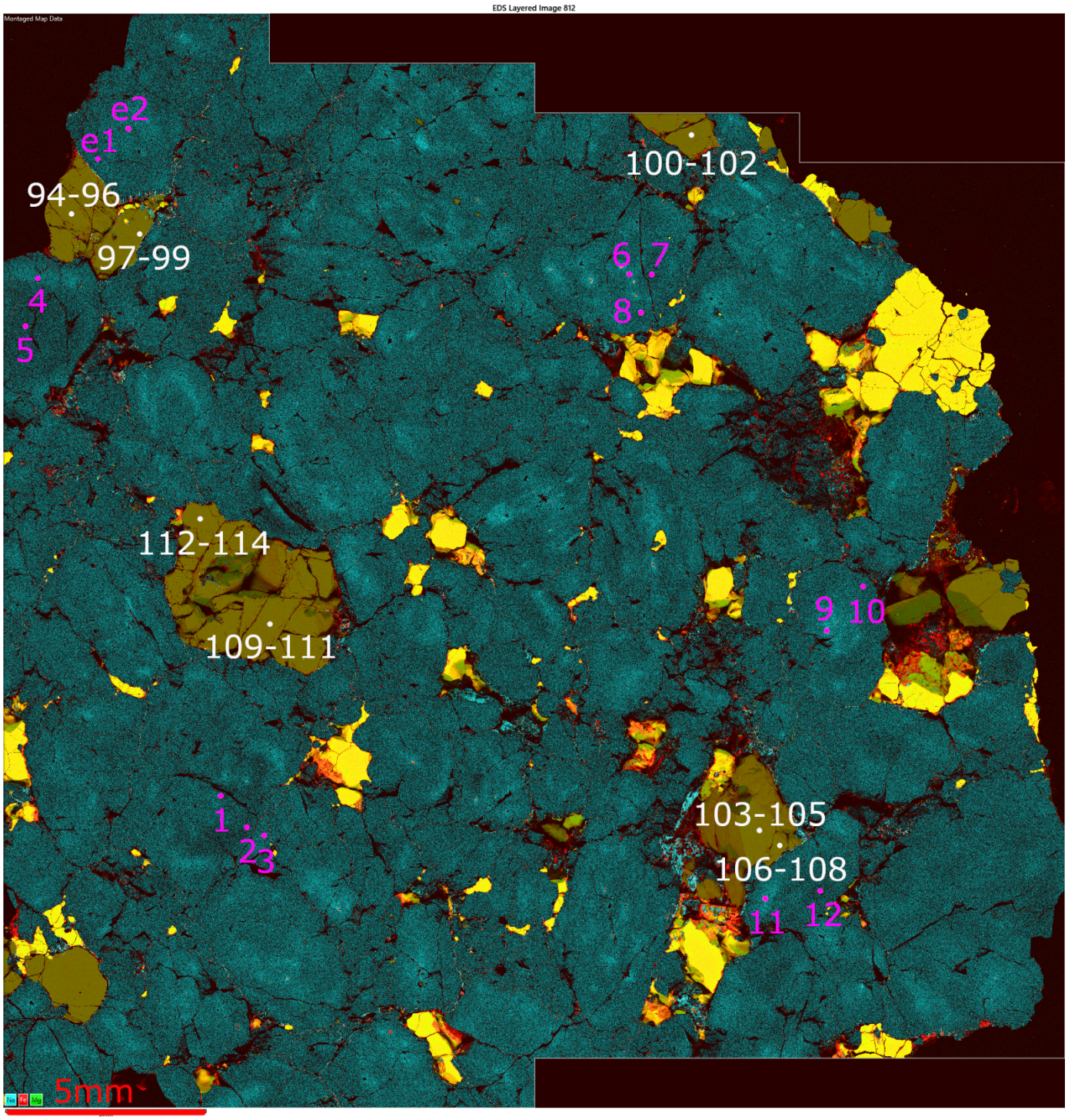

Figure 19: Major element map for sample 101863 provided by Dr Matthew Gleeson. Labelled locations are the locations targeted for major element, trace element and/or isotopic analysis. The bar on the bottom left shows the scale of the map. Fe was mapped in red, Mg in green and Na in blue. Yellow regions of the map are olivine, green/brown areas are clinopyroxene and blue areas are plagioclase.

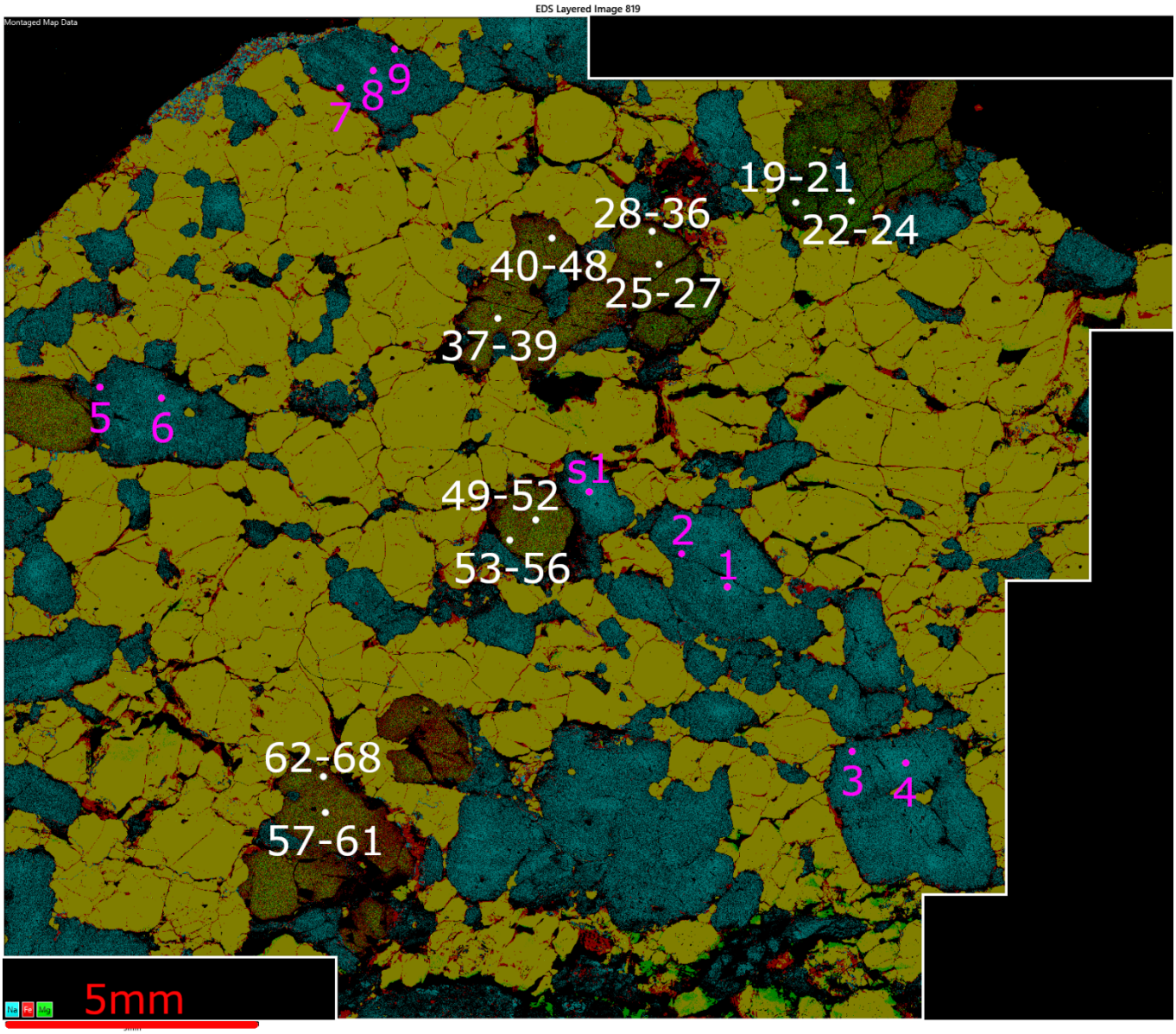

Figure 20: Major element map for sample 81874 provided by Dr Matthew Gleeson. Labelled locations are the locations targeted for major element, trace element and/or isotopic analysis. The bar on the bottom left shows the scale of the map. Fe was mapped in red, Mg in green and Na in blue. Yellow regions of the map are olivine, green/brown areas are clinopyroxene and blue areas are plagioclase.

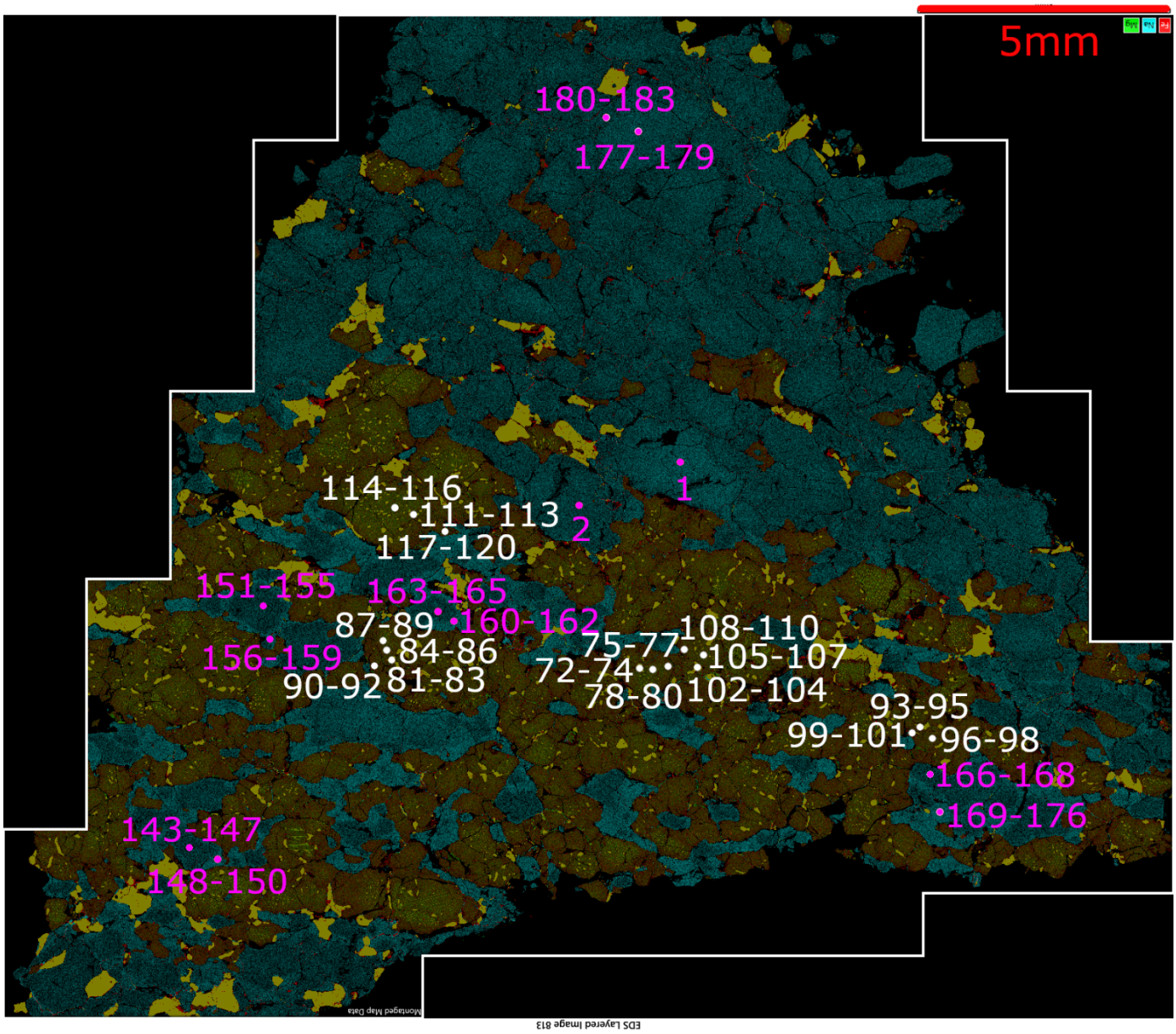

Figure 21: Major element map for sample 81869 provided by Dr Matthew Gleeson. Labelled locations are the locations targeted for major element, trace element and/or isotopic analysis. The bar in the top right shows the scale of the map. Fe was mapped in red, Mg in green and Na in blue. Yellow regions of the map are olivine, green/brown areas are clinopyroxene and blue areas are plagioclase.

4.2 Data and Evaluation of Partition Coefficients

Major element data was plotted to show TiO_2 (wt%) against Mg# of the analysed clinopyroxene locations within the samples, alongside the modelled path of fractional crystallisation of a basaltic melt (figure 22). TiO_2 values of the sample data range between

1.79 and 0.12 wt%, and Mg# values range between 0.86 and 0.75. Most sample array trends and core-rim trends follow the trend of the modelled path of fractional crystallisation. Exceptions to this include sample 81869 and 101870 which have near horizontal trends, 81874 which has a near vertical trend, and sample H1 where the core-rim trend from core 1-3 to rims 4-6 and 7-9 is not steep enough to match the modelled trend, and for which the core-rim trend is in the other direction to other core rim trends in the plot.

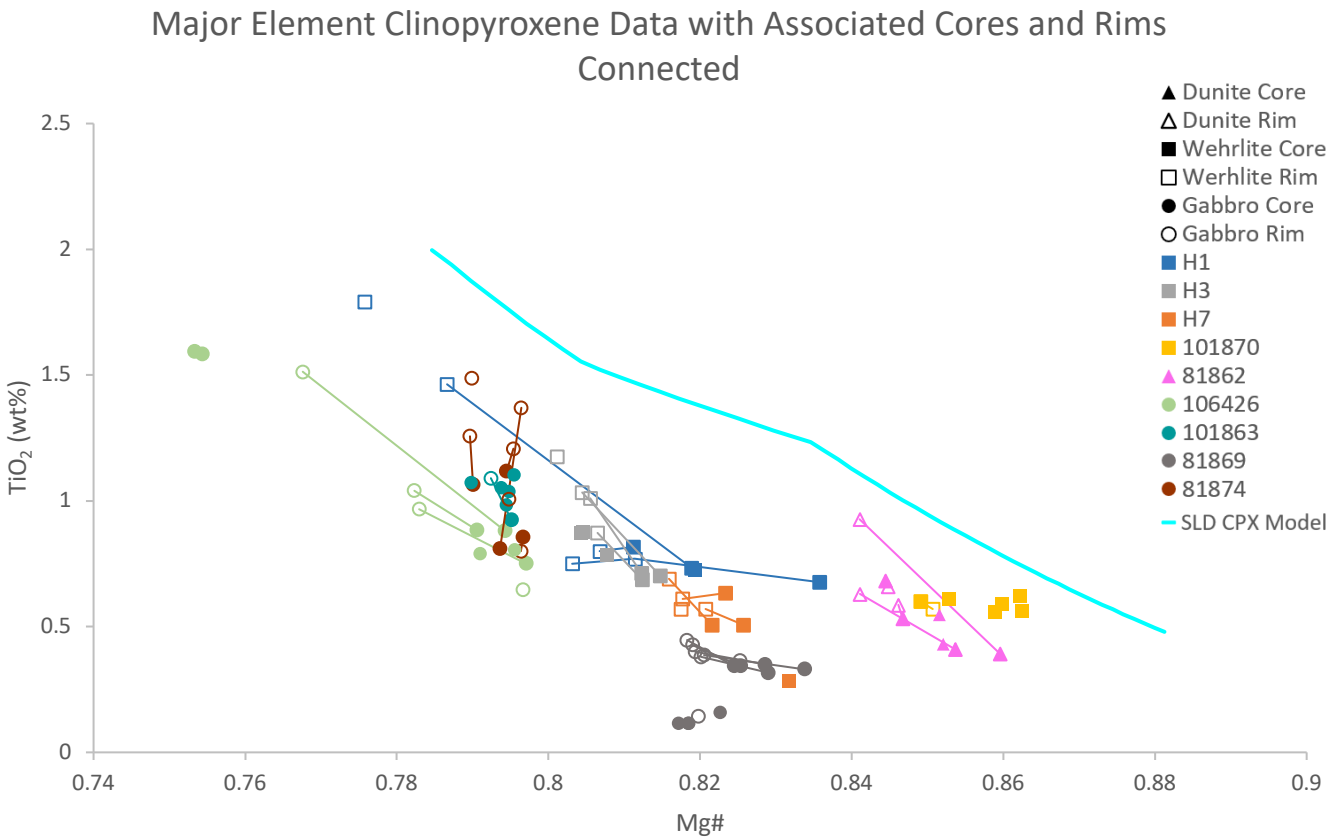

Figure 22: A graph showing the concentration of TiO_2 plotted against Mg# of sampled clinopyroxene locations from major element SEM analysis. Triangles denote dunitic samples, squares wehrlitic samples and circles gabbroic samples. Empty circles/squares/triangles represent crystal rims. Full circles/squares/triangles are crystal cores. Lines connect cores and rims of the same crystals. The blue line above the sample data shows the modelled path of fractional crystallisation of a basaltic melt calculated using the MELTS software (Gualda et al., 2012).

Major element data was plotted to show K_2O (wt%) against anorthite content of the analysed plagioclase locations within the samples (figure 23). Samples form two groups in

this plot, with 106426, 101863 and 81874 following a single trend and sample 81869 forming an isolated cluster at lower K_2O values. The K_2O values of samples 106426, 101863 and 81874 range between 0.29 and 0.09 wt%, and anorthite values of those same samples range between 0.81 and 0.61. The K_2O values of sample 81869 range between 0.07 and 0.02 wt%, and anorthite values range between 0.69 and 0.63.

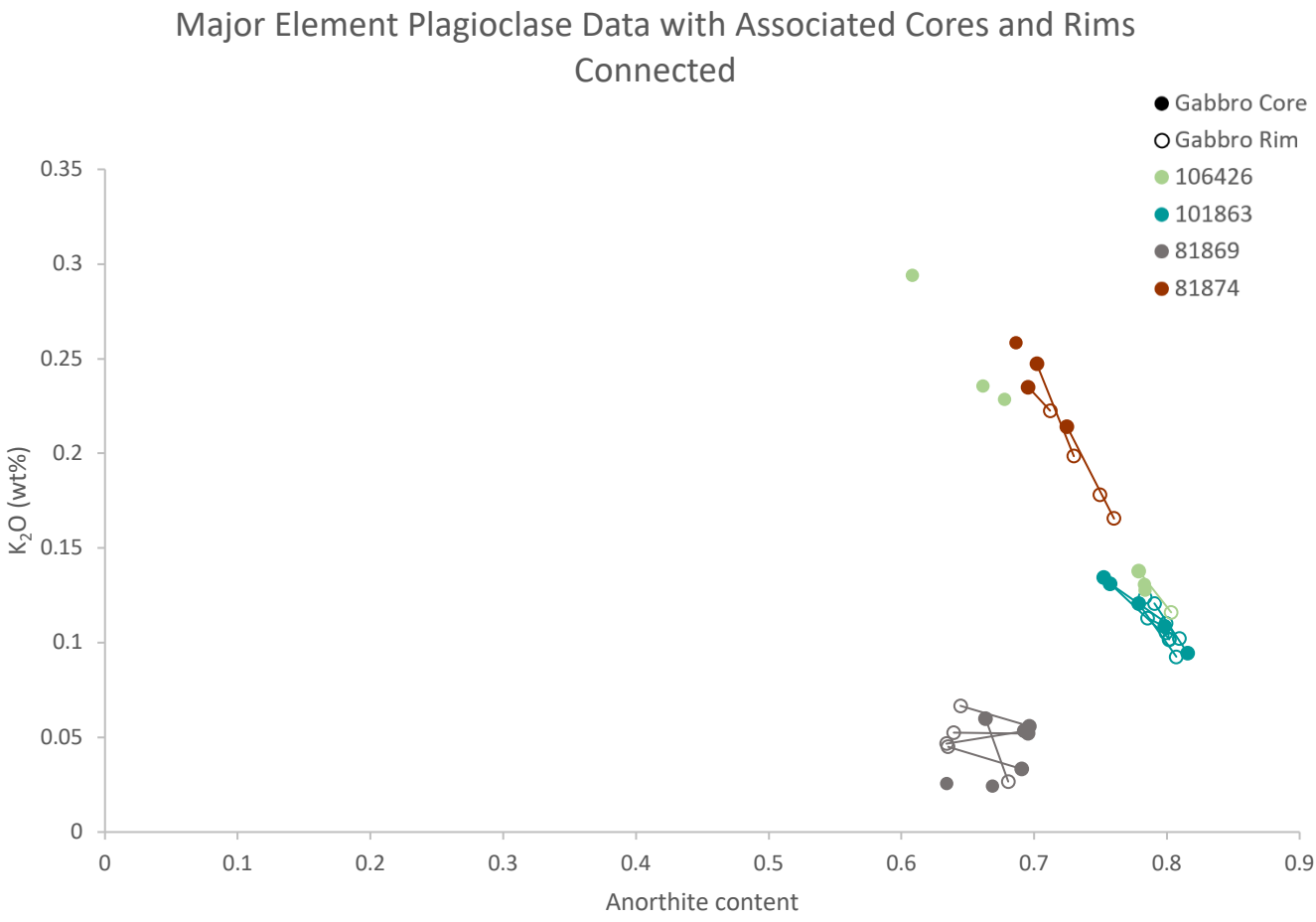

Figure 23: A graph showing the concentration of K_2O plotted against the anorthite content of sampled plagioclase locations from major element SEM analysis. Circles denote gabbroic samples. Empty circles represent crystal rims. Full circles are crystal cores. Lines connect cores and rims of the same crystals.

Trace element data was plotted to show La/Sm normalised to the primitive mantle against La concentrations normalised to the primitive mantle (figure 24), and Ce/Y normalised to the primitive mantle against Ce concentrations normalised to the primitive mantle (Figure

25) of the analysed clinopyroxene locations within the samples, alongside the modelled path of fractional crystallisation of a basaltic melt. Most sample array trends and core-rim trends follow the trend of the modelled path of fractional crystallisation. Exception to this include sample 81869 which forms a trace element depleted cluster, sample 101870 which has a steeper trend than the model and extends to higher La/Sm and Ce/Y values than the rest of the sample array, and the core-rim trend from core 1-3 to rims 4-6 and 7-9 in sample H1, which is too steep to match the modelled trend and for which the core-rim trend is in the other direction to other core rim trends in the plot.

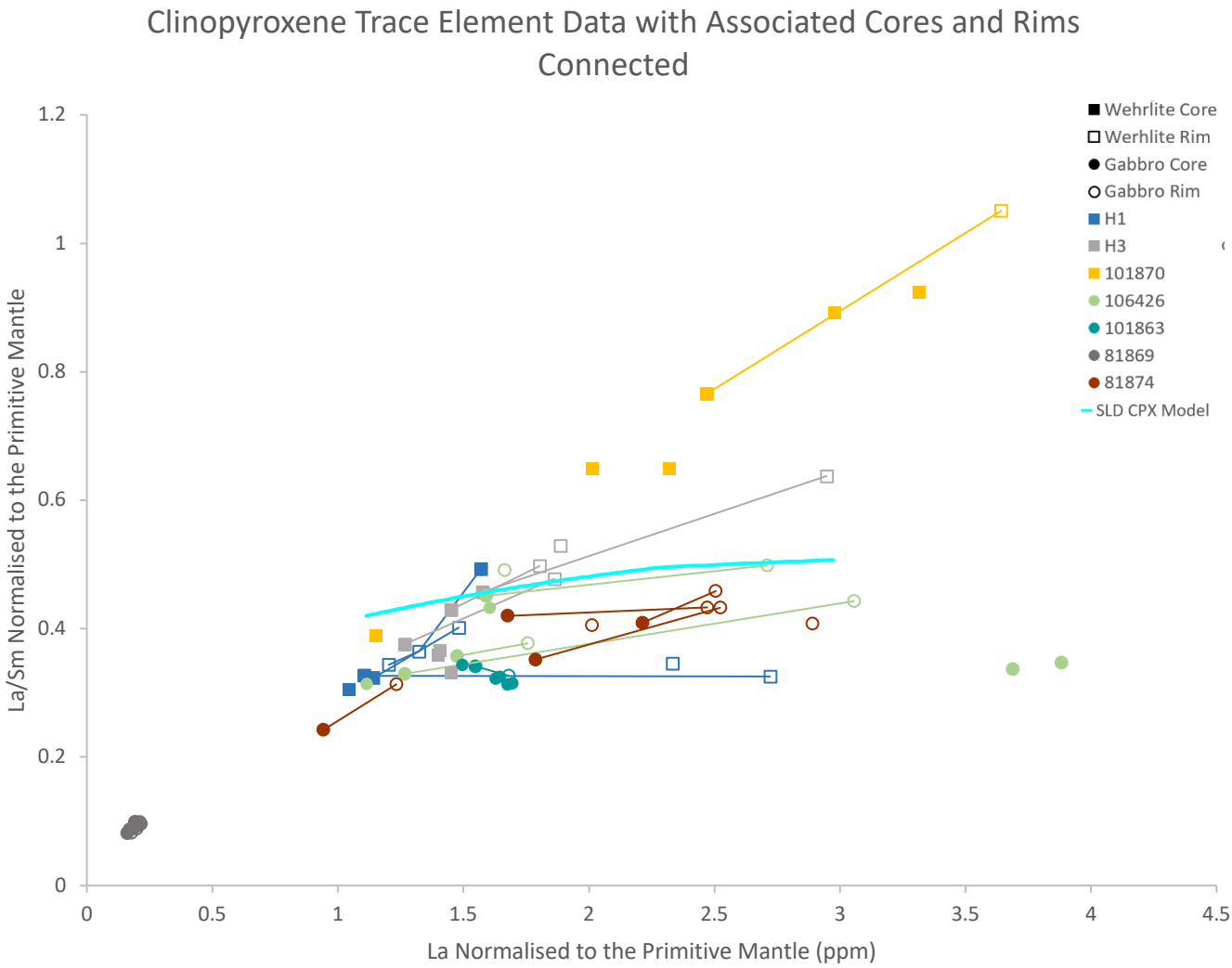

Figure 24: A plot of La/Sm normalised to the primitive mantle against La concentrations normalised to the primitive mantle for sampled clinopyroxene locations from trace element analysis. Squares denote wehrlitic samples and circles gabbroic samples. Empty

circles/squares represent crystal rims. Full circles/squares are crystal cores. Lines connect cores and rims of the same crystals. The blue line shows the modelled path of fractional crystallisation of a basaltic melt calculated using the MELTS software (Gualda et al., 2012). Trace element data from laser ablation was normalised to the primitive mantle using primitive mantle values given by McDonough and Sun (1995).

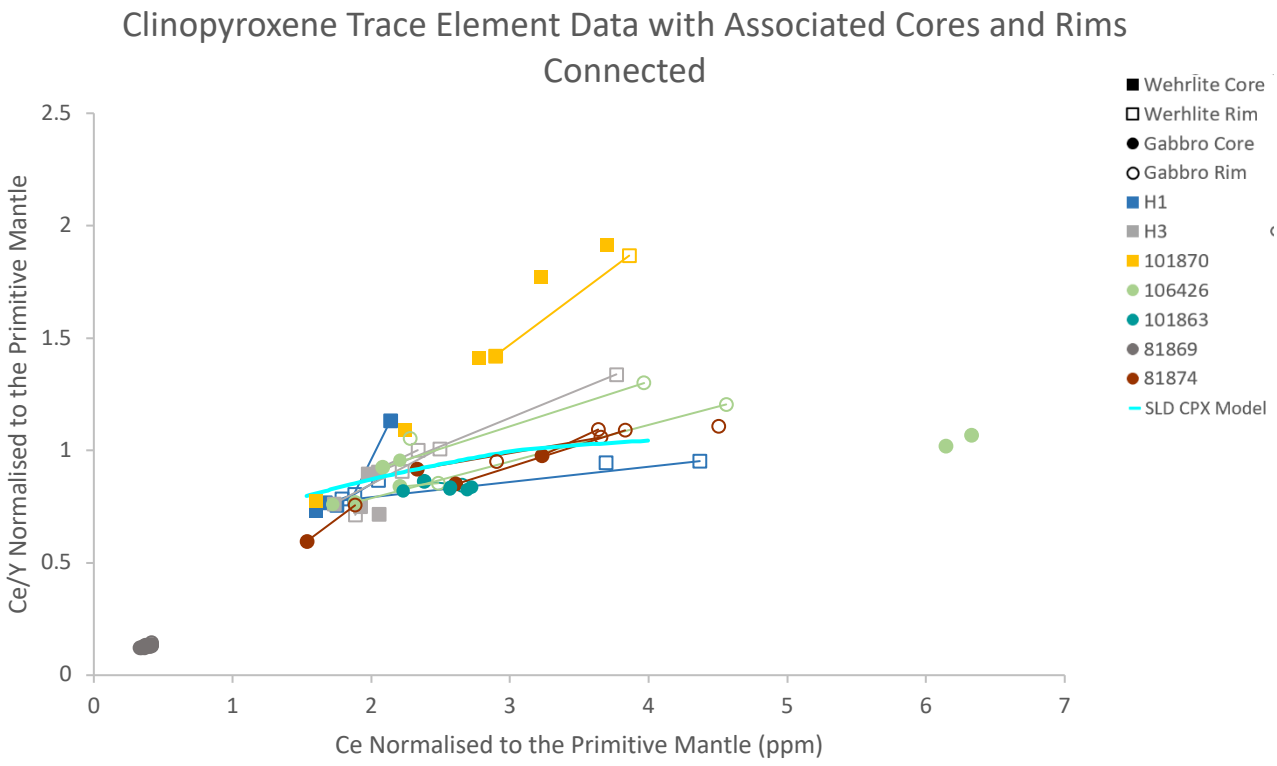

Figure 25: A plot of Ce/Y normalised to the primitive mantle against Ce concentrations normalised to the primitive mantle for sampled clinopyroxene locations from trace element analysis. Squares denote wehrlitic samples and circles gabbroic samples. Empty circles/squares represent crystal rims. Full circles/squares are crystal cores. Lines connect cores and rims of the same crystals. The blue line shows the modelled path of fractional crystallisation of a basaltic melt calculated using the MELTS software (Gualda et al., 2012). Trace element data from laser ablation was normalised to the primitive mantle using primitive mantle values given by McDonough and Sun (1995).

Primitive mantle-normalised diagrams of trace element concentration data from the analysis of clinopyroxene (figures 26-32) and plagioclase (figures 33-36) crystals were

plotted. Sample 81869 (figure 32) shows trace element concentrations, especially in the lighter trace elements, that are depleted relative to the other plots of clinopyroxene trace element concentration data for samples H1, H3, 101870, 101863, 106426 and 81874. From elements La to Lu (except Pb) in the clinopyroxene data, all samples bar 81869 have concentrations ranging between 0.9ppm and 11.2ppm, whereas sample 81869 only ranges from 0.2 to 3.7 (also excluding Pb).

It is also interesting to note that measured trace element concentrations are lower for most elements in the plagioclase data relative to the clinopyroxene data.

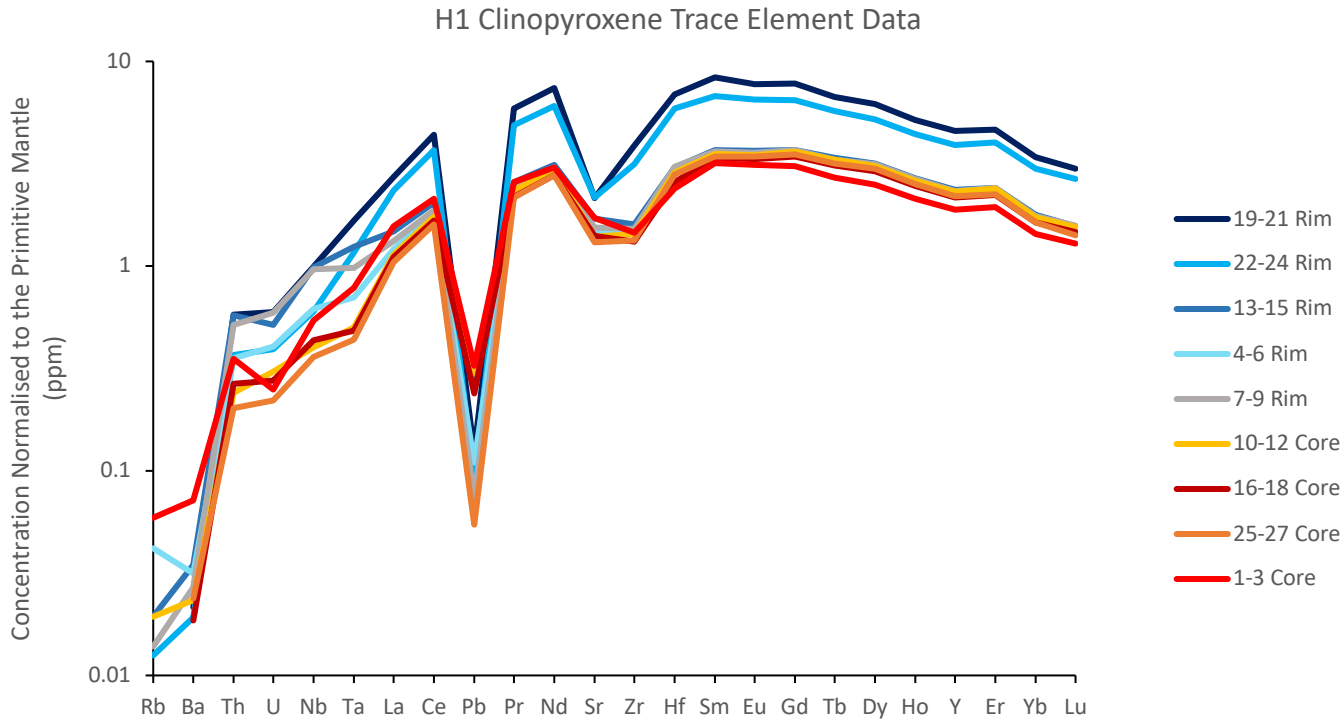

Figure 26: A diagram of trace element concentration data normalised to the primitive mantle for sampled clinopyroxene locations in sample H1. Trace element data from laser ablation was normalised to the primitive mantle using primitive mantle values given by McDonough and Sun (1995). Blue-grey lines represent crystal rims, and yellow-red lines represent crystal cores.

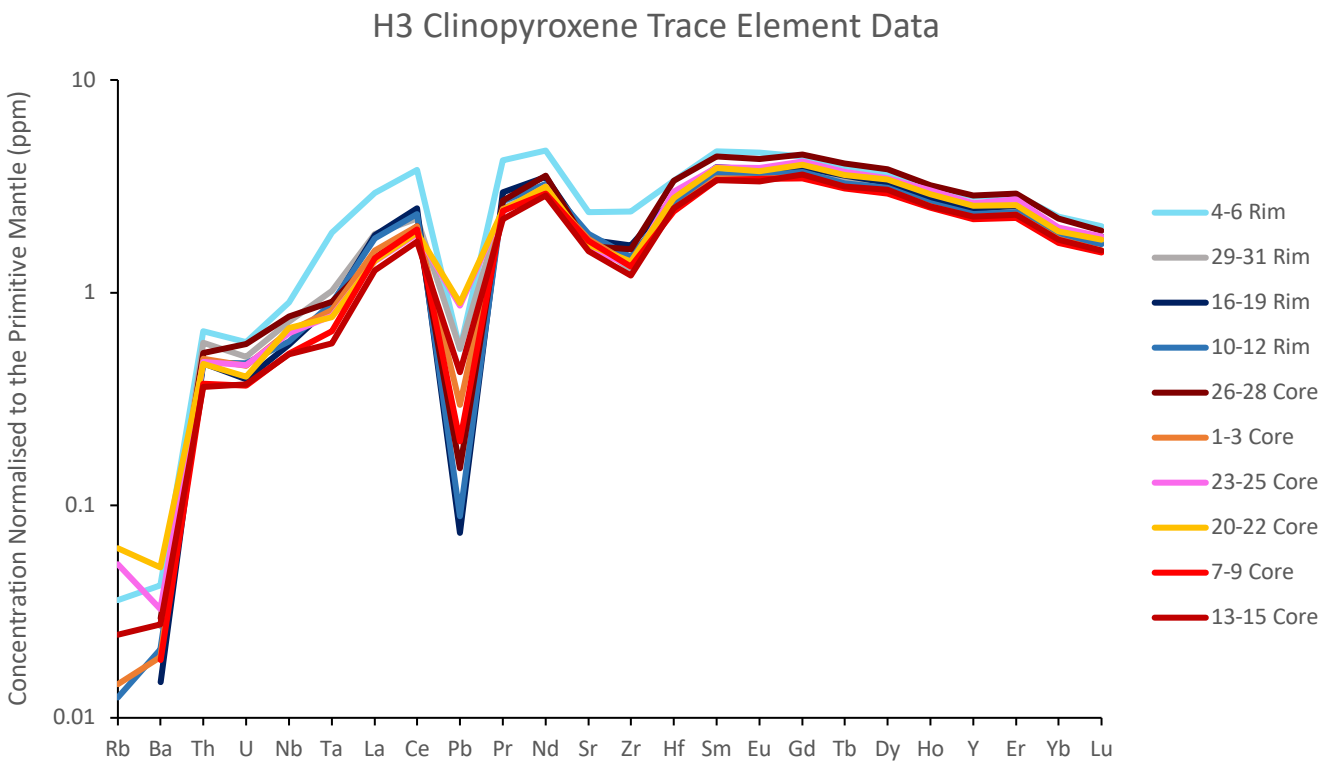

Figure 27: A diagram of trace element concentration data normalised to the primitive mantle for sampled clinopyroxene locations in sample H3. Trace element data from laser ablation was normalised to the primitive mantle using primitive mantle values given by McDonough and Sun (1995). Blue-grey lines represent crystal rims, and yellow-red lines represent crystal cores.

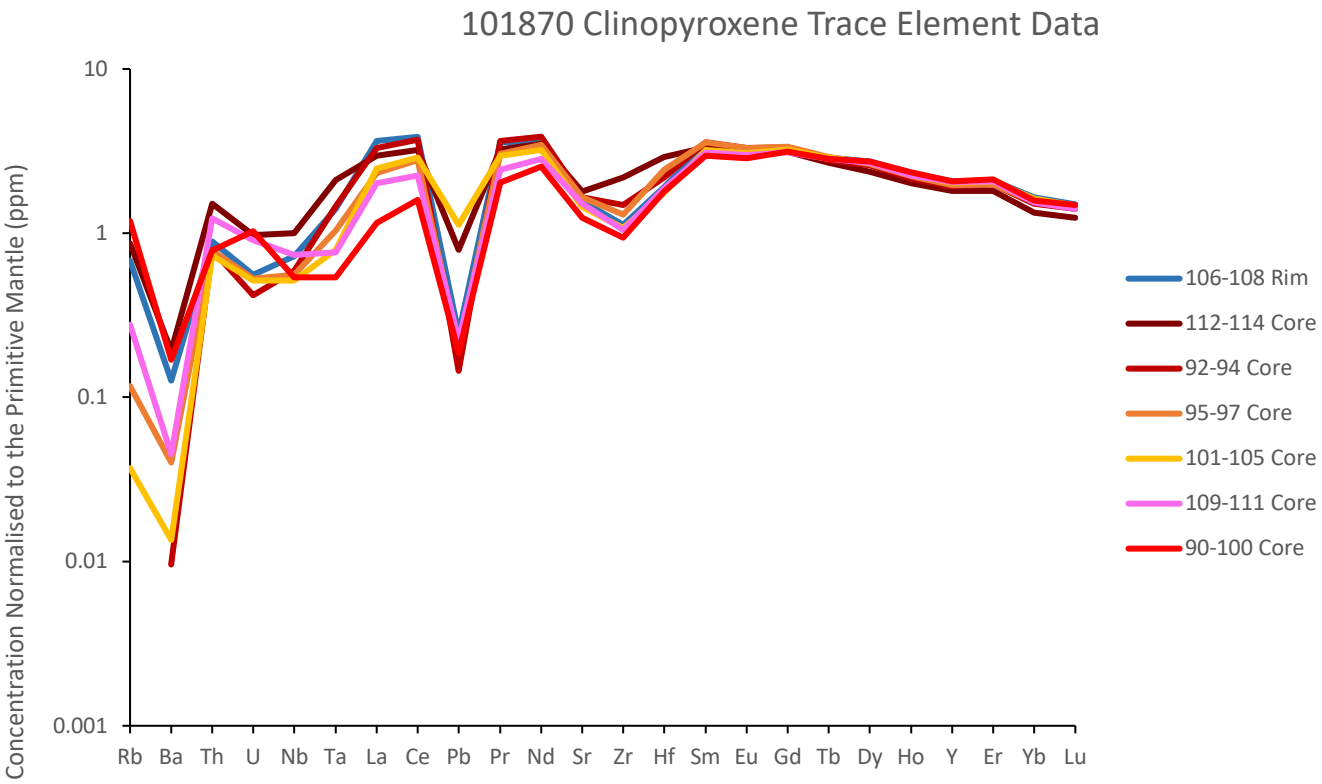

Figure 28: A diagram of trace element concentration data normalised to the primitive mantle for sampled clinopyroxene locations in sample 101870. Trace element data from laser ablation was normalised to the primitive mantle using primitive mantle values given by McDonough and Sun (1995). Blue-grey lines represent crystal rims, and yellow-red lines represent crystal cores.

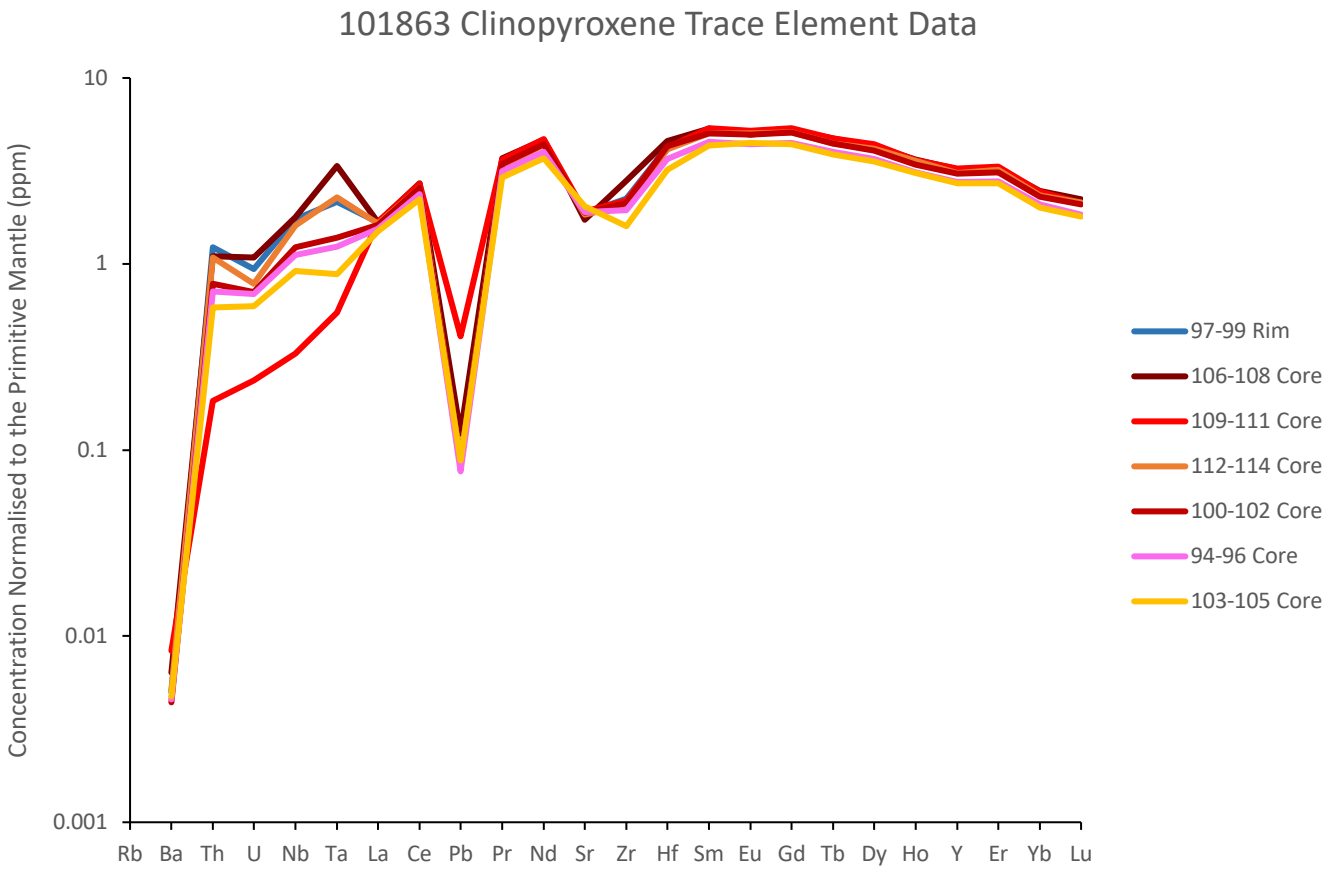

Figure 29: A diagram of trace element concentration data normalised to the primitive mantle for sampled clinopyroxene locations in sample 101863. Trace element data from laser ablation was normalised to the primitive mantle using primitive mantle values given by McDonough and Sun (1995). Blue-grey lines represent crystal rims, and yellow-red lines represent crystal cores.

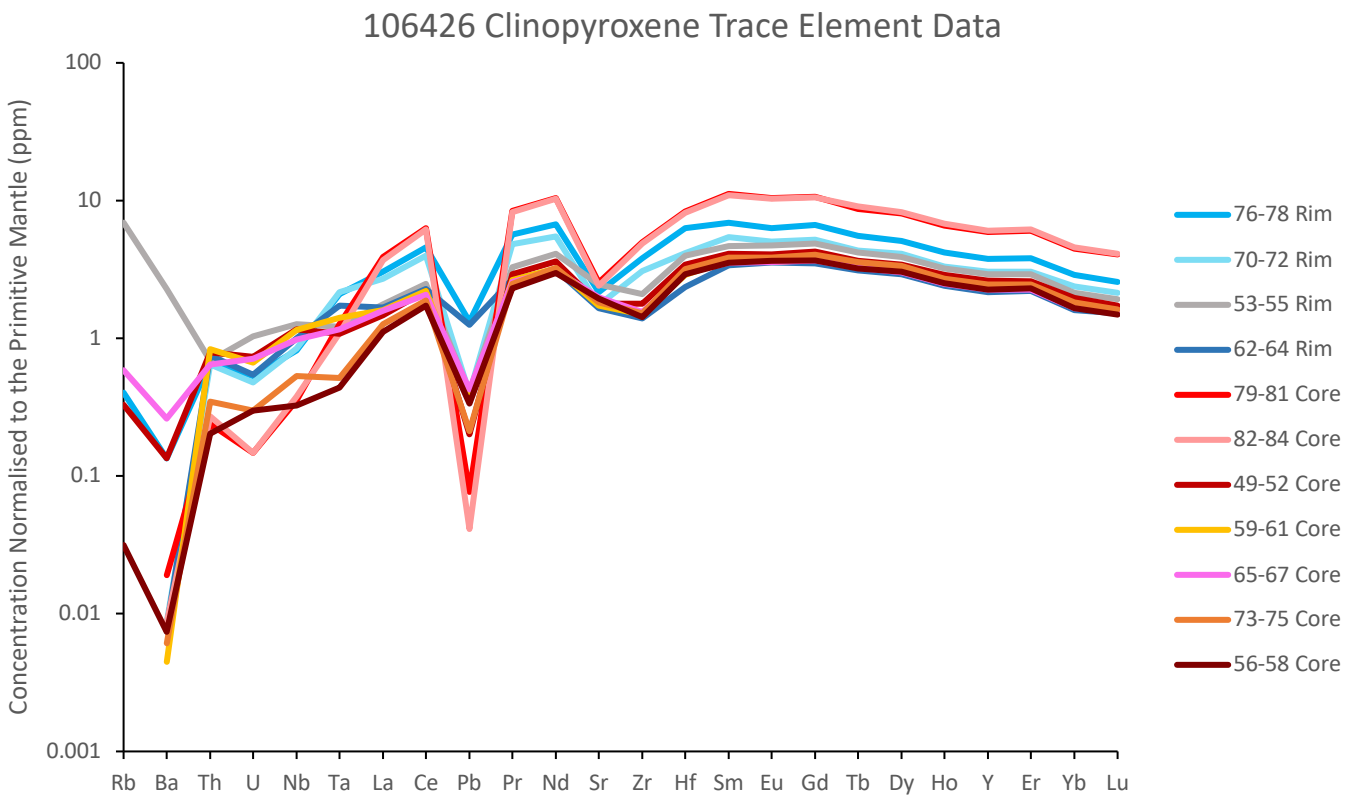

Figure 30: A diagram of trace element concentration data normalised to the primitive mantle for sampled clinopyroxene locations in sample 106426. Trace element data from laser ablation was normalised to the primitive mantle using primitive mantle values given by McDonough and Sun (1995). Blue-grey lines represent crystal rims, and yellow-red lines represent crystal cores.

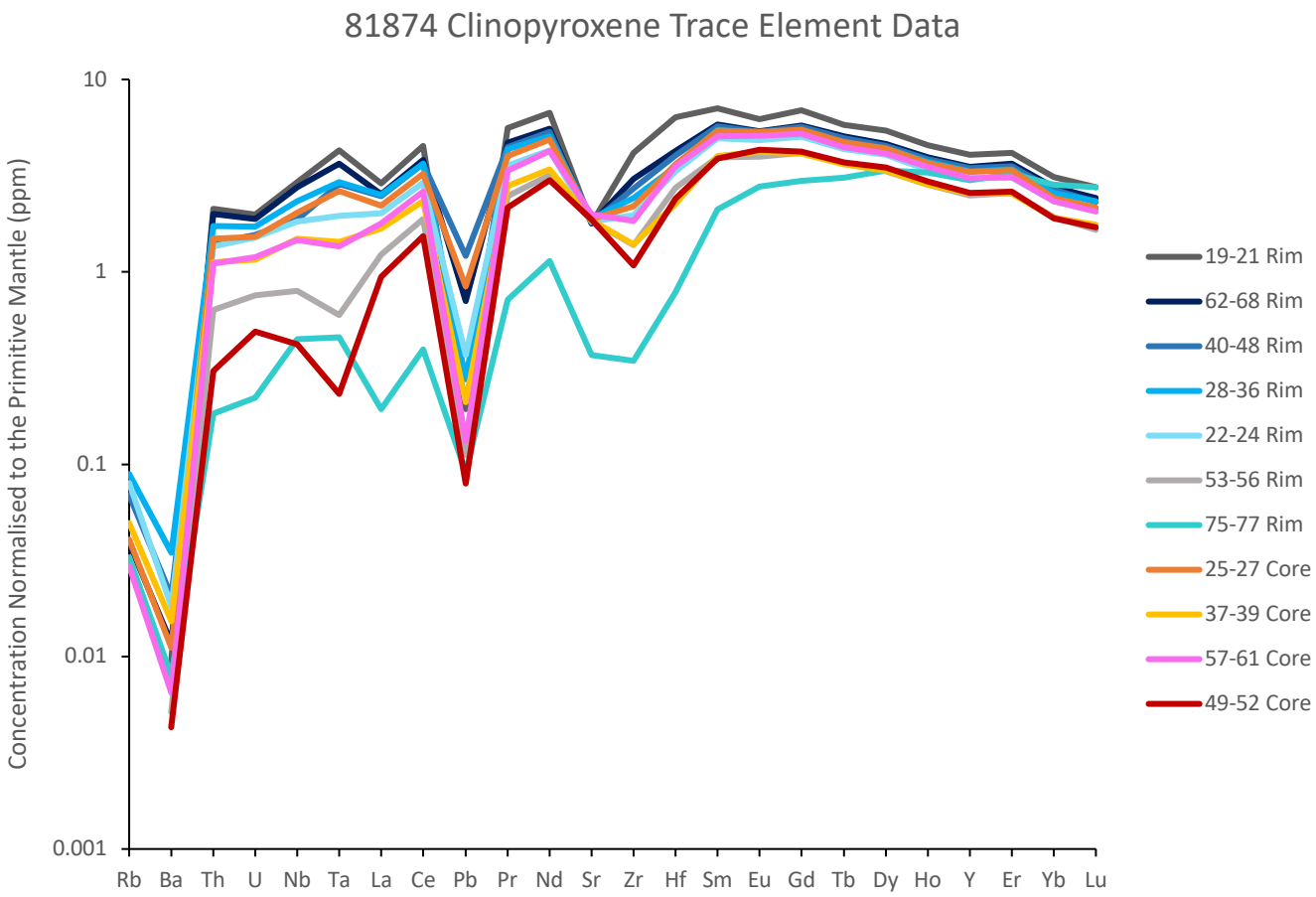

Figure 31: A diagram of trace element concentration data normalised to the primitive mantle for sampled clinopyroxene locations in sample 81874. Trace element data from laser ablation was normalised to the primitive mantle using primitive mantle values given by McDonough and Sun (1995). Blue-grey lines represent crystal rims, and yellow-red lines represent crystal cores.

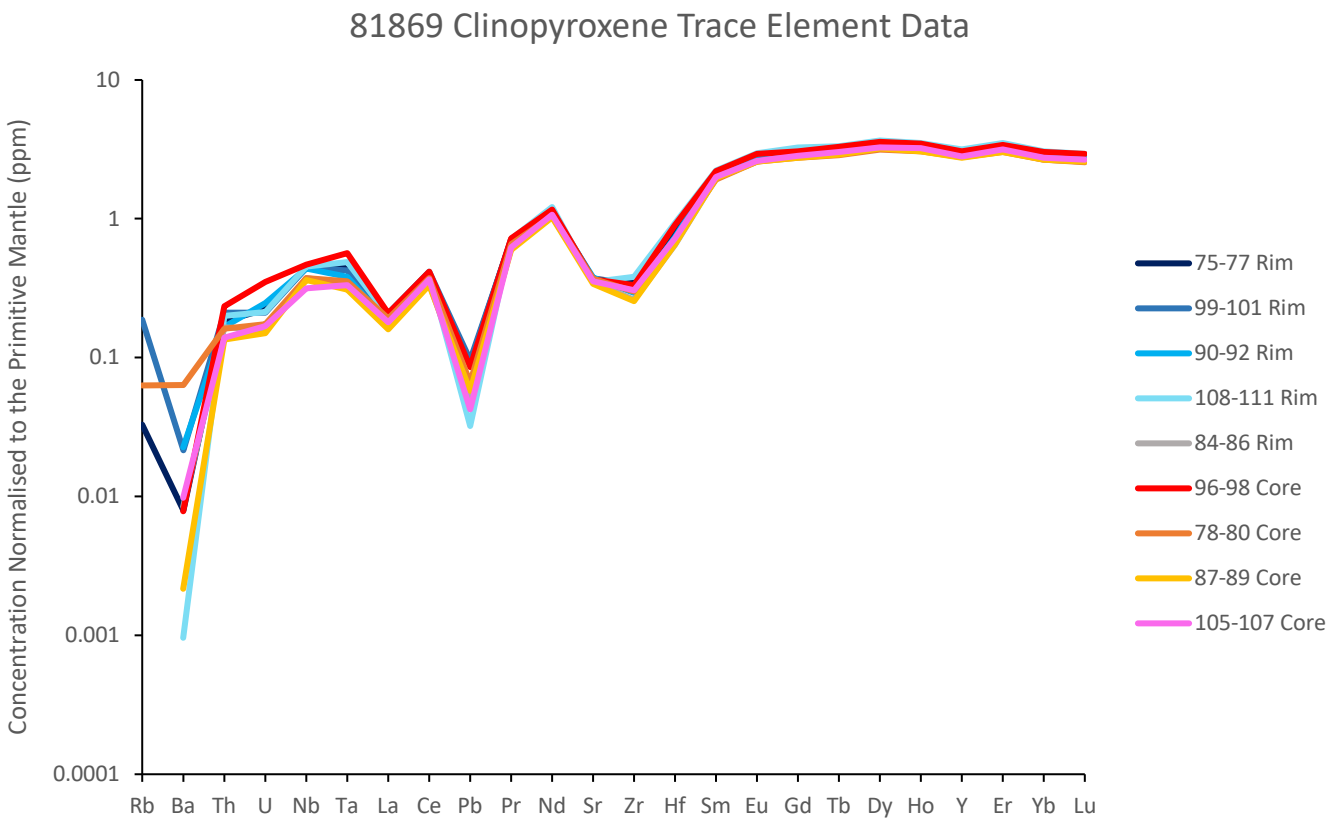

Figure 32: A diagram of trace element concentration data normalised to the primitive mantle for sampled clinopyroxene locations in sample 81869. Trace element data from laser ablation was normalised to the primitive mantle using primitive mantle values given by McDonough and Sun (1995). Blue-grey lines represent crystal rims, and yellow-red lines represent crystal cores.

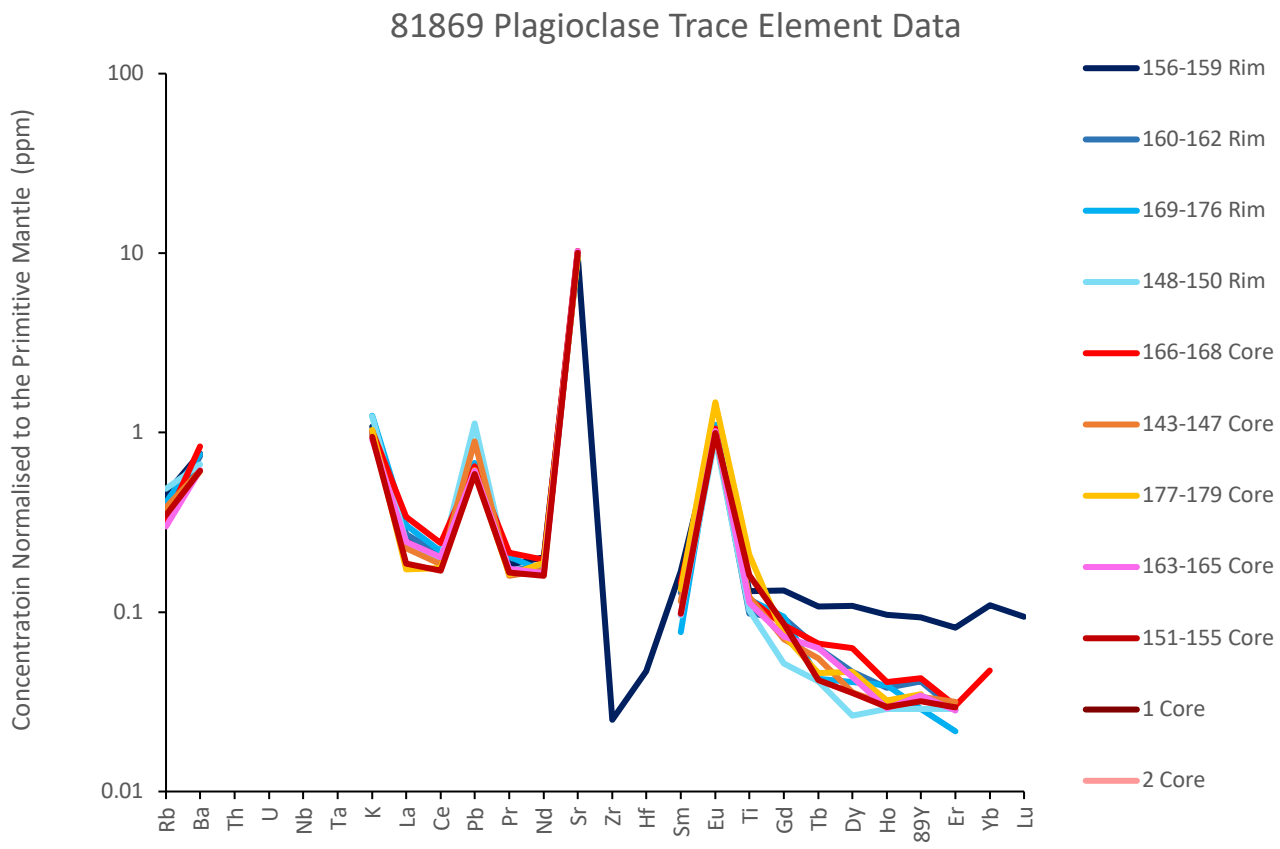

Figure 33: A diagram of trace element concentration data normalised to the primitive mantle for sampled plagioclase locations in sample 81869. Trace element data from laser ablation was normalised to the primitive mantle using primitive mantle values given by McDonough and Sun (1995). Blue-grey lines represent crystal rims, and yellow-red lines represent crystal cores.

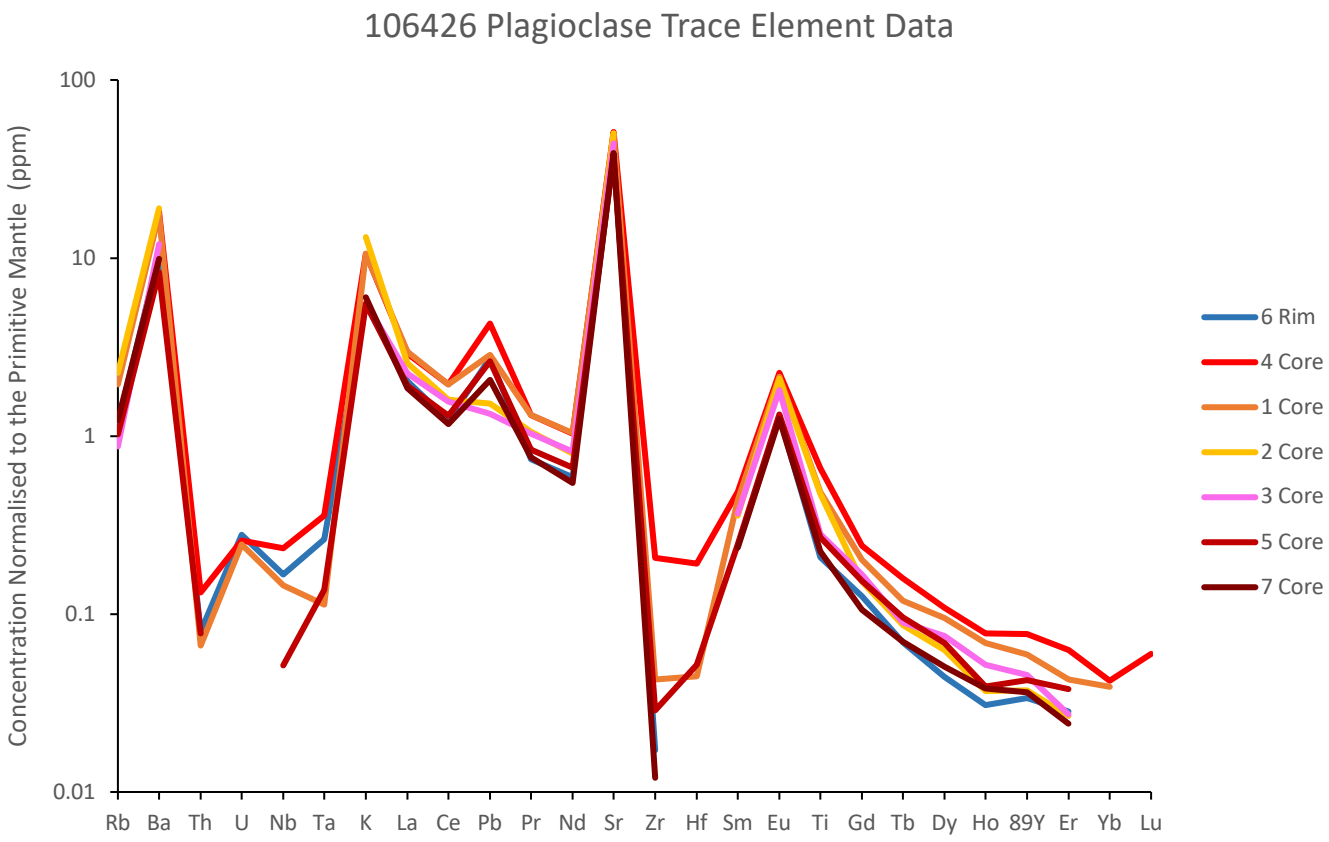

Figure 34: A diagram of trace element concentration data normalised to the primitive mantle for sampled plagioclase locations in sample 106426. Trace element data from laser ablation was normalised to the primitive mantle using primitive mantle values given by McDonough and Sun (1995). Blue-grey lines represent crystal rims, and yellow-red lines represent crystal cores.

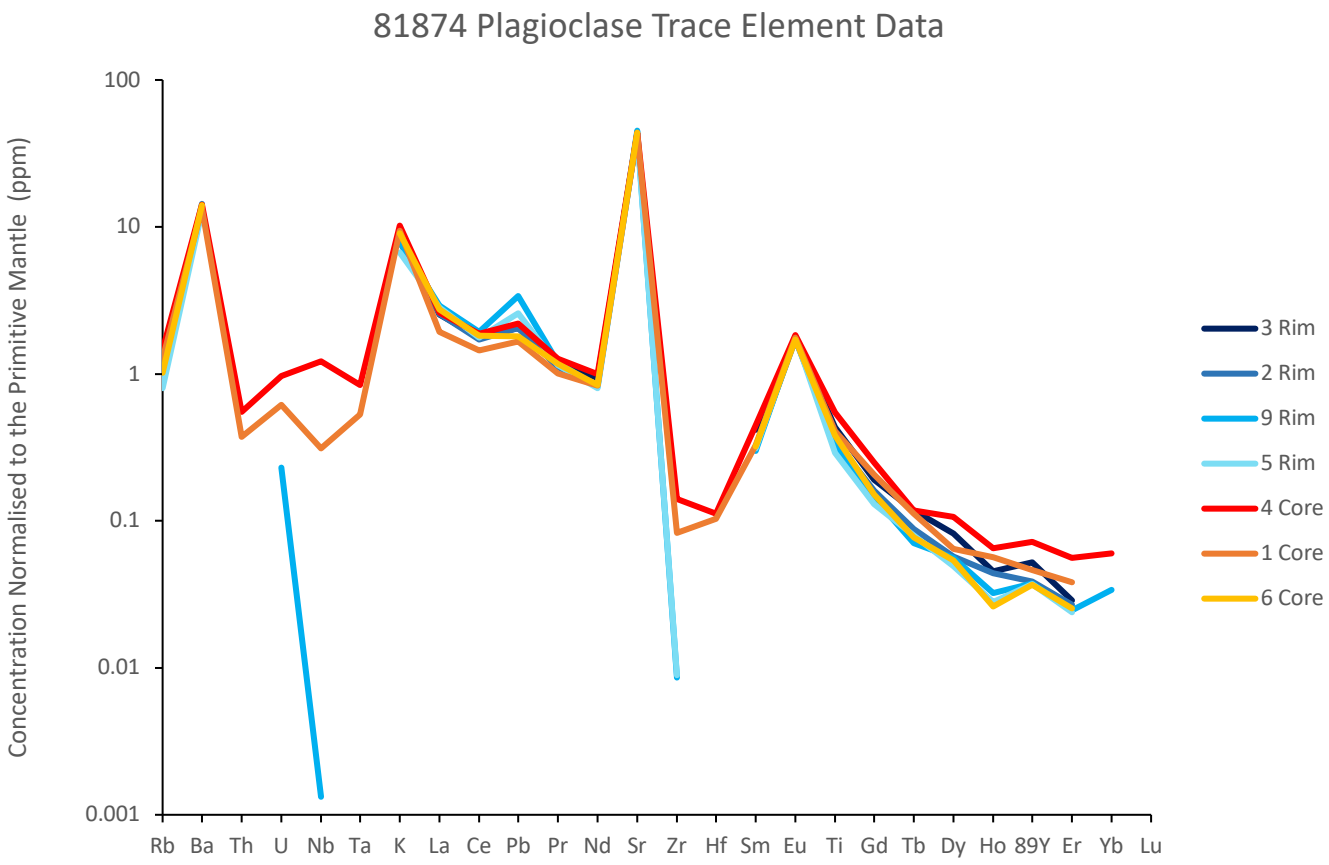

Figure 35: A diagram of trace element concentration data normalised to the primitive mantle for sampled plagioclase locations in sample 81874. Trace element data from laser ablation was normalised to the primitive mantle using primitive mantle values given by McDonough and Sun (1995). Blue-grey lines represent crystal rims, and yellow-red lines represent crystal cores.

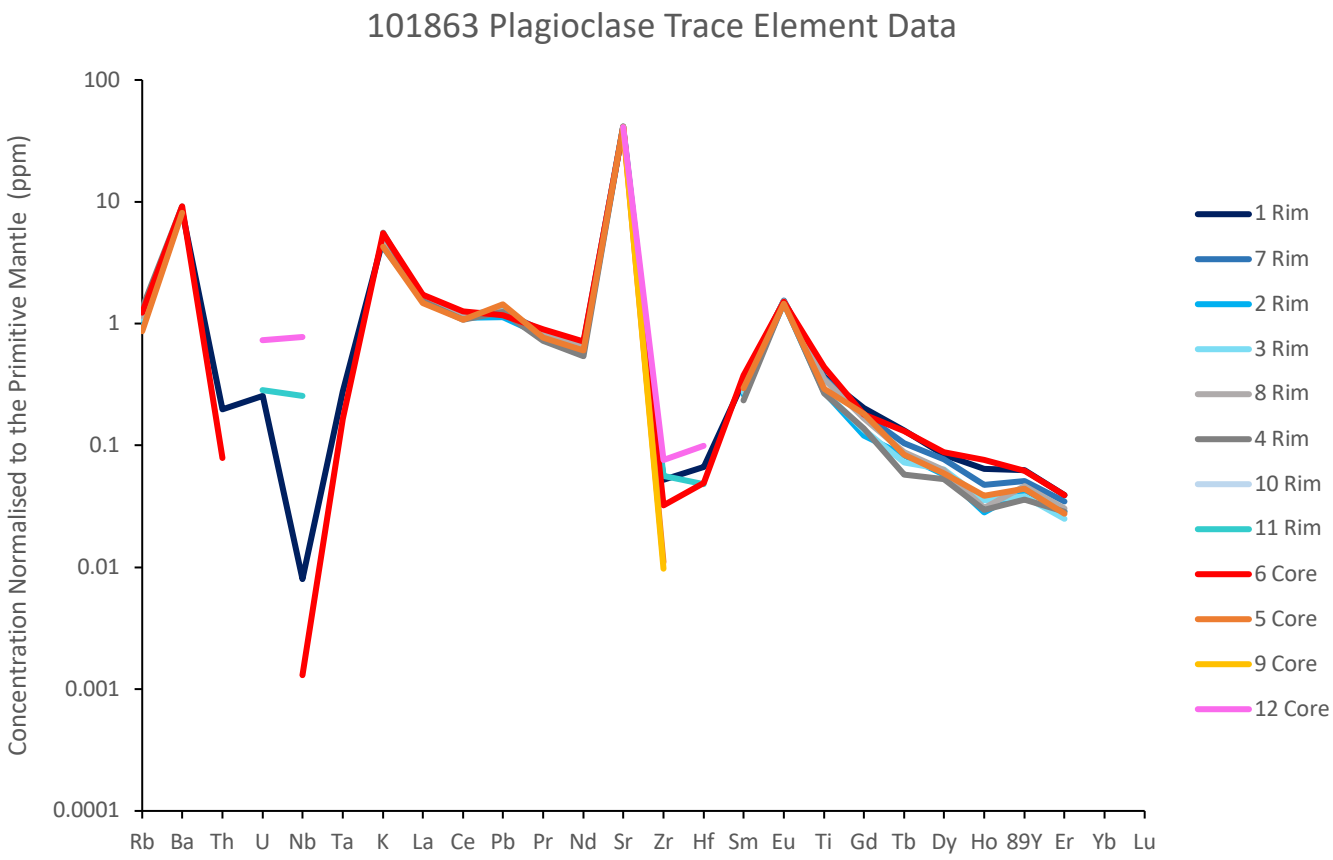

Figure 36: A diagram of trace element concentration data normalised to the primitive mantle for sampled plagioclase locations in sample 101863. Trace element data from laser ablation was normalised to the primitive mantle using primitive mantle values given by McDonough and Sun (1995). Blue-grey lines represent crystal rims, and yellow-red lines represent crystal cores.

Published volcanic whole rock (VWR) data for post-shield basalts, post-shield trachytes and shield stage picrites from Hualalai were downloaded from the GEOROC database (https://georoc.eu/) on 6 October 2021, using the following parameters: geographical location = Hualalai; Hawaii: rock type = volcanic. The post-shield basaltic, post-shield trachytic and shield stage picritic data found on GEOROC was compiled from published data (Washington, 1923; Washington and Keyes, 1928; Piggot, 1931; Lessing et al., 1963; Lessing and Catanzero, 1964; Powell et al., 1965; Hamilton, 1965; Somayajulu et al., 1966; Tatsumoto, 1966; Macdonald, 1968; Funkhouser et al., 1968; Schilling and Winchester, 1969; O'Nions et al., 1977; Anonymous, 1980; Clague et al., 1980; Moore and Clague, 1987;

Moore *et al.*, 1987; Clague, 1987; Clague and Bohrson, 1991; Sobolev and Nikogosian, 1994; Sims *et al.*, 1995; Pickett and Murrell, 1997; Sims and Depaolo, 1997; Sims *et al.*, 1999; Stracke et al., 1999; Cousens et al., 2003; Hanano *et al.*, 2010; Shea *et al.*, 2017). Trace element data from GEOROC was normalised to the primitive mantle using primitive mantle values given by McDonough and Sun (1995).

This data was used to compare the data collected in this project to published data to assess whether the data collected in this study extended the known published trace element and isotopic heterogeneity for basaltic melts. It was also used to produce models of the path of fractional crystallisation for basaltic melts (as detailed in the methods above). Diagrams of the trace element concentration data normalised to the primitive mantle from this published data set (e.g., fig. 37) were used to create basaltic and trachytic fields for the background of the primitive mantle-normalised trace element diagrams for easy comparison (figs. 38-48).

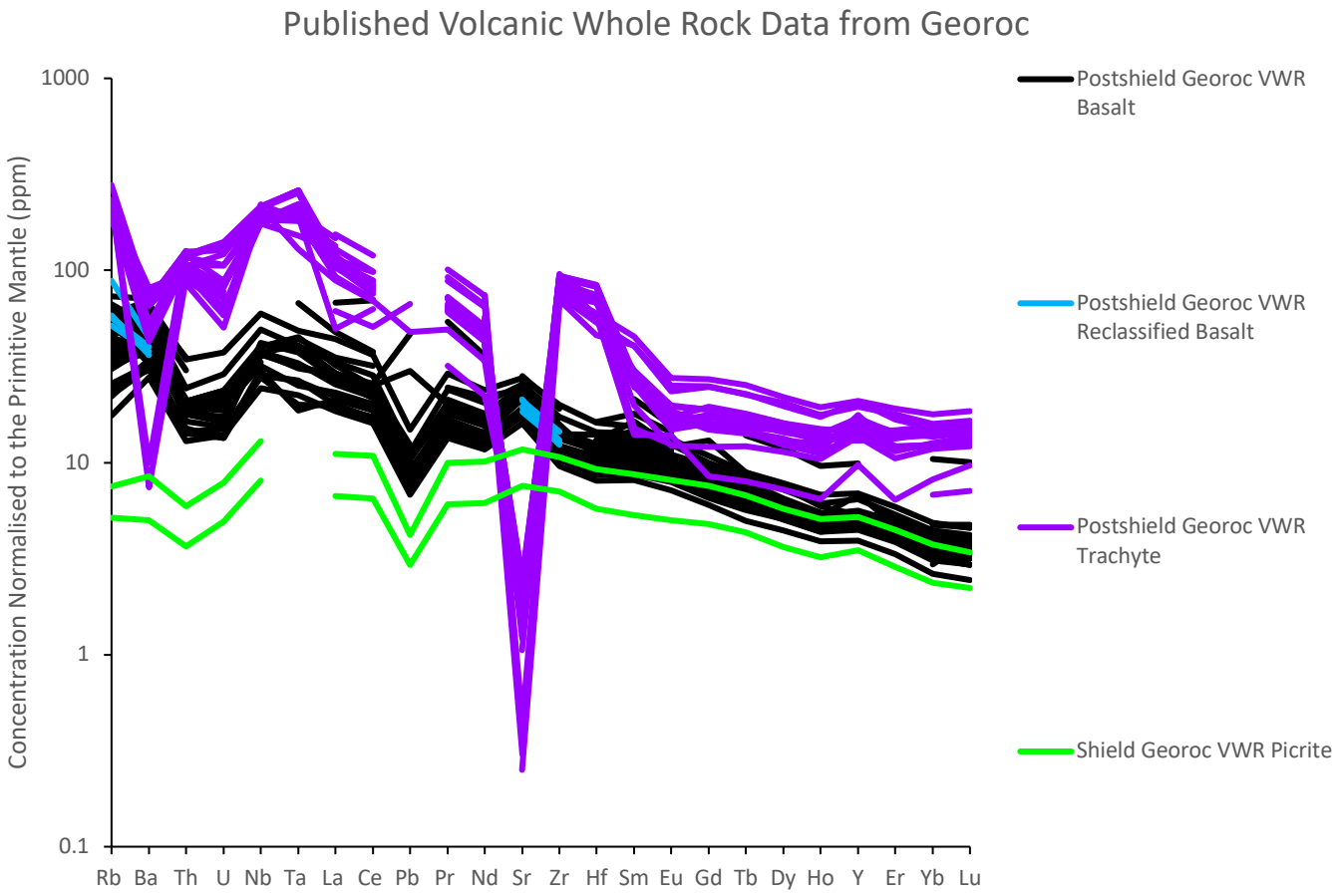

Figure 37: A diagram of trace element concentration data normalised to the primitive mantle for published volcanic whole rock (VWR) data from Hualalai. The basaltic and trachytic post-shield data and shield picrite data was downloaded from the GEOROC database (see full references from page 61). Trace element data from GEOROC was normalised to the primitive mantle using primitive mantle values given by McDonough and Sun (1995). Black lines represent post-shield basaltic samples, blue lines represent data from postshield basaltic samples which were called trachytes on GEOROC, purple lines represent data for post-shield trachytic samples and green lines represent data for shield stage picrite samples.

The post-shield VWR data downloaded from GEOROC was used to plot a basaltic and trachytic field, over which was superimposed the equilibrium melt compositions of each sample, calculated from clinopyroxene (figs. 42-48) and plagioclase data (figs. 38- 41). Equilibrium melt compositions for plagioclase data were calculated using two different sets of partition coefficients; one calculated from Sun, Graff and Liang (2017) and Shannon (1976), and one from Bédard (2006). Equilibrium melt compositions for clinopyroxene data were also calculated using two different partition coefficients; one calculated from Sun and Liang (2012), Hill, Blundy and Wood (2011, 2012) and Shannon (1976), and one calculated from Bédard (2014). The results of different partition coefficients were plotted separately in order to evaluate the effects of the different partition coefficients. Pressures and temperatures of clinopyroxene crystallisation (used to calculate these partition coefficients, see Appendices) were calculated by Gleeson et al. (Unpublished Data) using the clinopyroxene-only thermobarometer of Wang et al. (2021). Equations 1 and 2 from Wang et al. (2021) were used for pressure and temperature, respectively. Calculations were performed using the Python3 package Thermobar (Wieser, Petrelli et al. 2022).

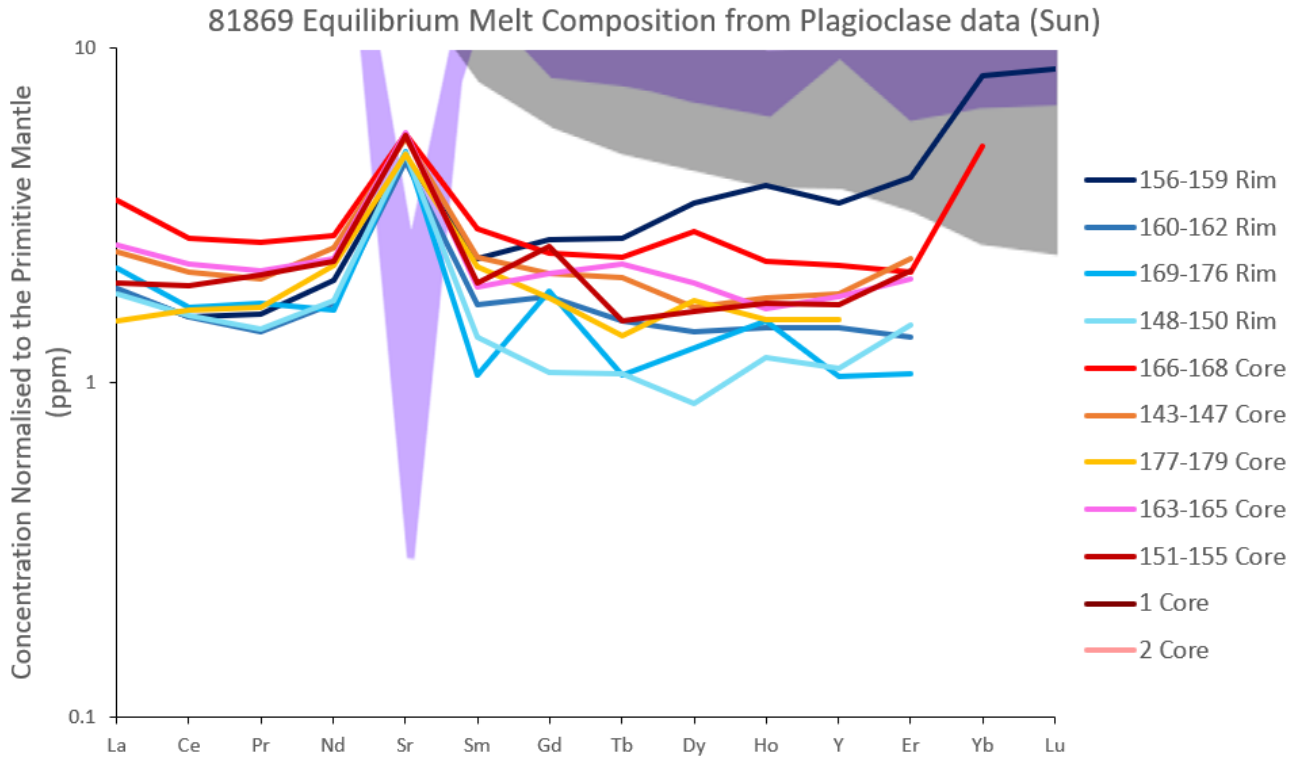
81869 Equilibrium Melt Composition from Plagioclase data (Sun)
Concentration Normalised to the Primitive Mantle (ppm)
10
1
0.1
La
Ce
Pr
Nd
Sr
Sm
Gd
Tb
Dy
Ho
Y
Er
Yb
Lu
156-159 Rim
160-162 Rim
169-176 Rim
148-150 Rim
166-168 Core
143-147 Core
177-179 Core
163-165 Core
151-155 Core
1 Core
2 Core

a)

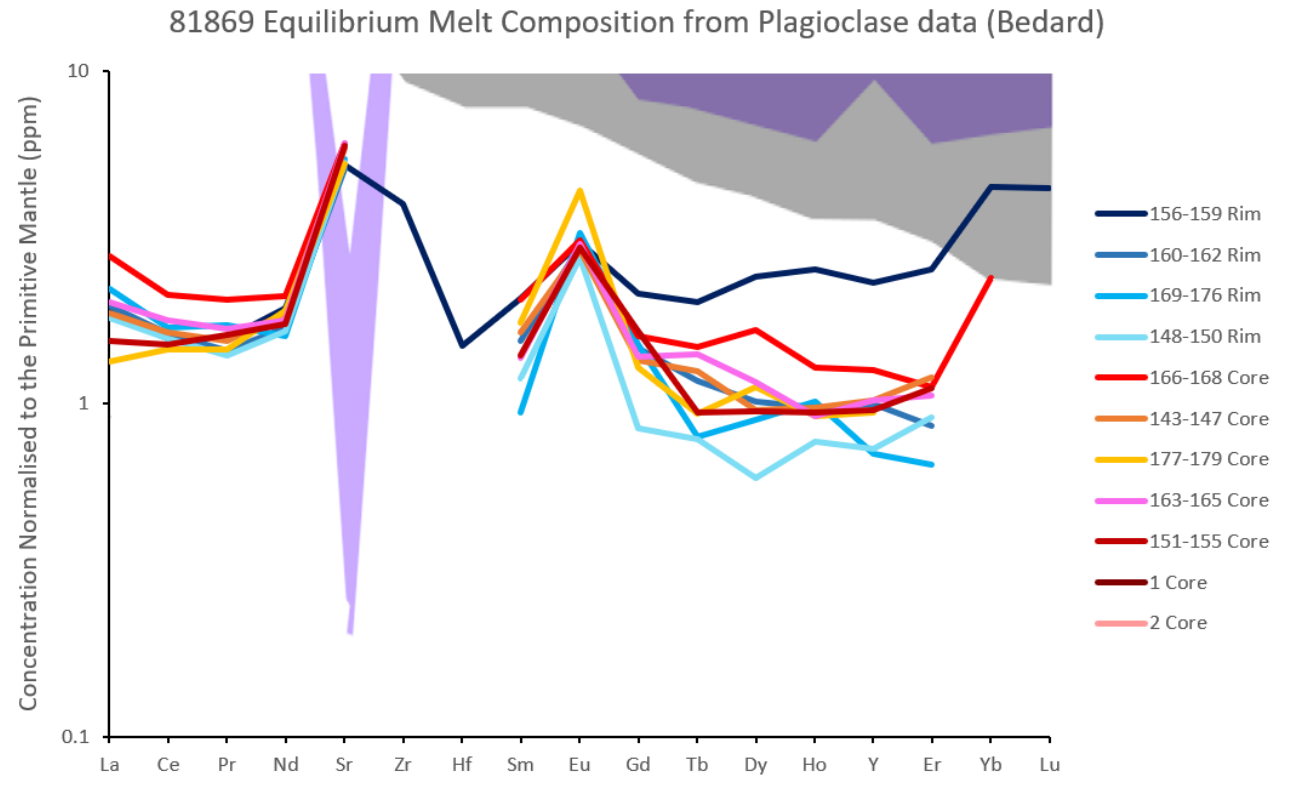
81869 Equilibrium Melt Composition from Plagioclase data (Bedard)
Concentration Normalised to the Primitive Mantle (ppm)
10
1
0.1
La
Ce
Pr
Nd
Sr
Zr
Hf
Sm
Eu
Gd
Tb
Dy
Ho
Y
Er
Yb
Lu
156-159 Rim
160-162 Rim
169-176 Rim
148-150 Rim
166-168 Core
143-147 Core
177-179 Core
163-165 Core
151-155 Core
1 Core
2 Core

b)

Figure 38: Diagrams of trace element concentration data normalised to the primitive mantle for equilibrium melt compositions calculated from plagioclase data for sample 81869, superimposed on basaltic (grey field) and trachytic (purple field) fields created from published post-shield basaltic and trachytic volcanic whole rock data downloaded from the GEOROC database (see full references from page 21). Trace element data was normalised to the primitive mantle using primitive mantle values given by McDonough and Sun (1995). Blue-grey lines represent crystal rims, and yellow-red lines represent crystal cores. The equilibrium melt composition in a) was calculated using partition coefficients calculated using Sun et al. (2017) and Shannon (1976). The equilibrium melt composition in b) was calculated using partition coefficients calculated using Bédard (2006).

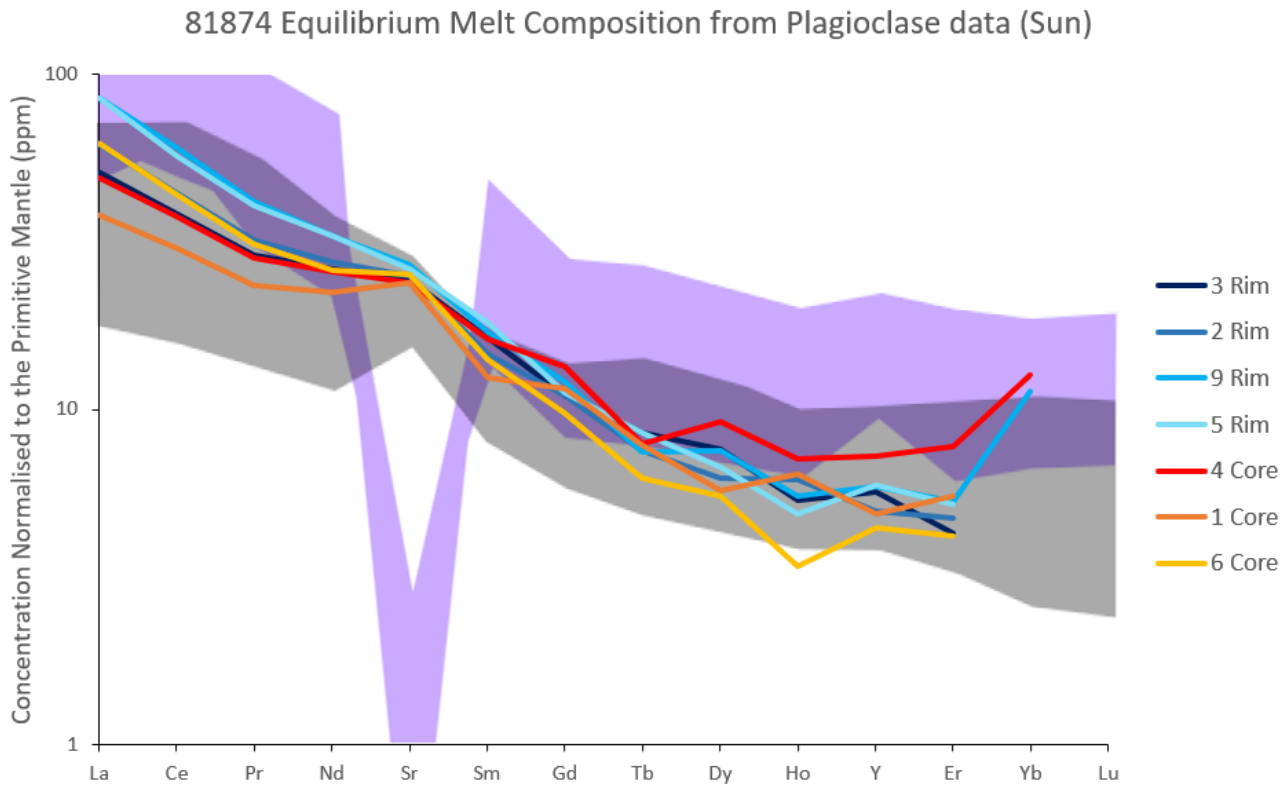

a)

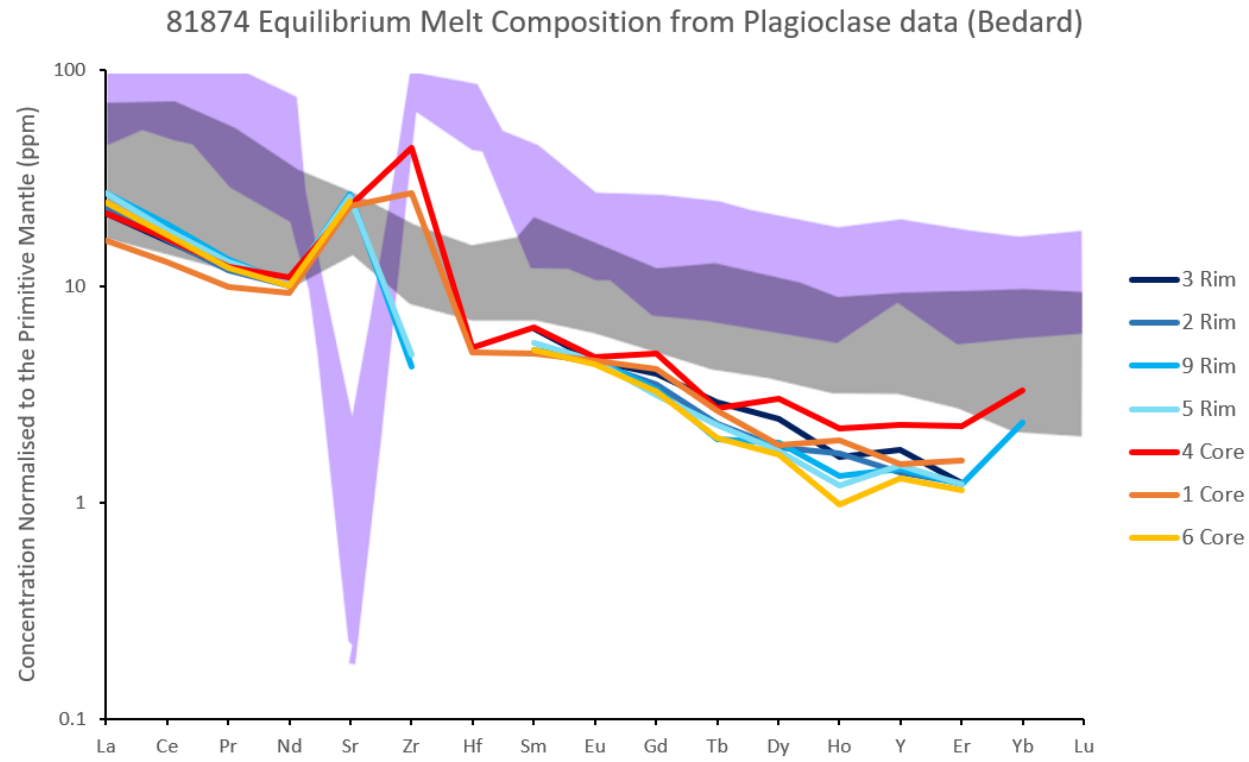

b)

Figure 39: Diagrams of trace element concentration data normalised to the primitive mantle for equilibrium melt compositions calculated from plagioclase data for sample 81874, superimposed on basaltic (grey field) and trachytic (purple field) fields created from published post-shield basaltic and trachytic volcanic whole rock data downloaded from the GEOROC database (see full references from page 21). Trace element data was normalised to the primitive mantle using primitive mantle values given by McDonough and Sun (1995).Blue-grey lines represent crystal rims, and yellow-red lines represent crystal cores. The equilibrium melt composition in a) was calculated using partition coefficients calculated using Sun et al. (2017) and Shannon (1976). The equilibrium melt composition in b) was calculated using partition coefficients calculated using Bédard (2006).

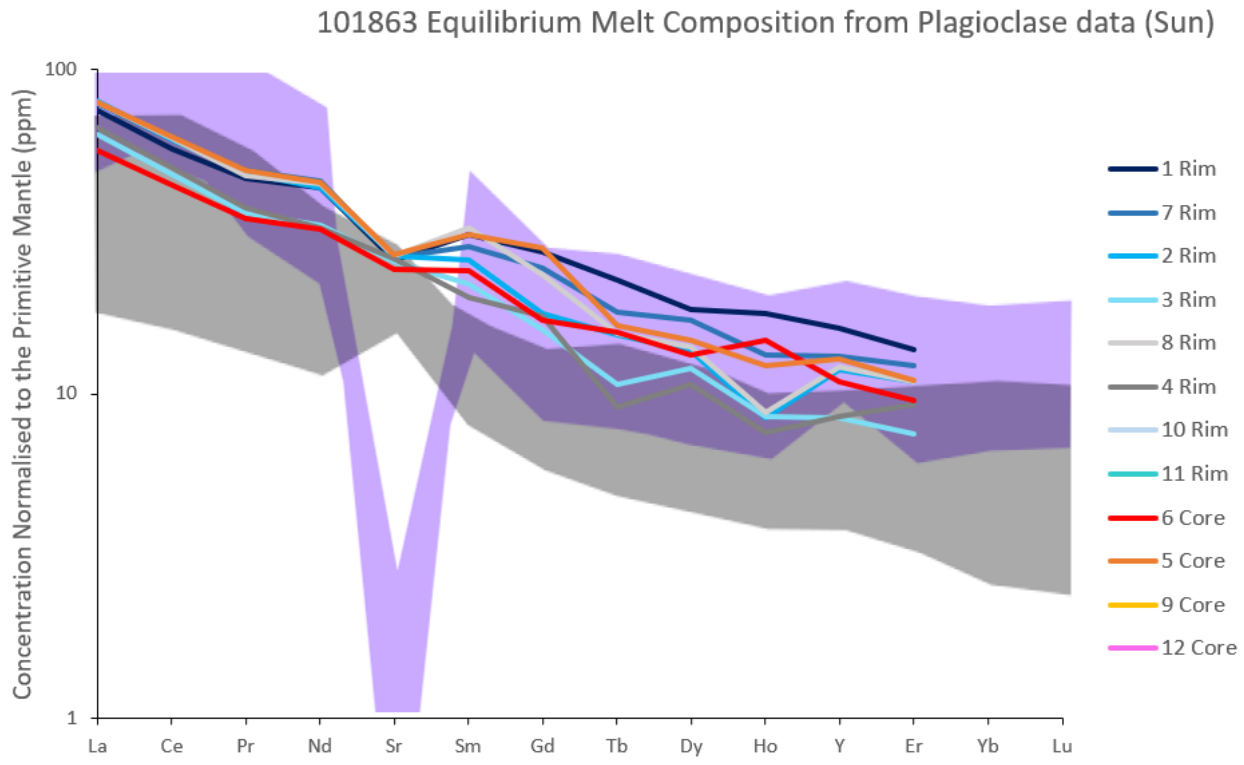
101863 Equilibrium Melt Composition from Plagioclase data (Sun)
Concentration Normalised to the Primitive Mantle (ppm)
100
10
1
La
Ce
Pr
Nd
Sr
Sm
Gd
Tb
Dy
Ho
Y
Er
Yb
Lu
1 Rim
7 Rim
2 Rim
3 Rim
8 Rim
4 Rim
10 Rim
11 Rim
6 Core
5 Core
9 Core
12 Core

a)

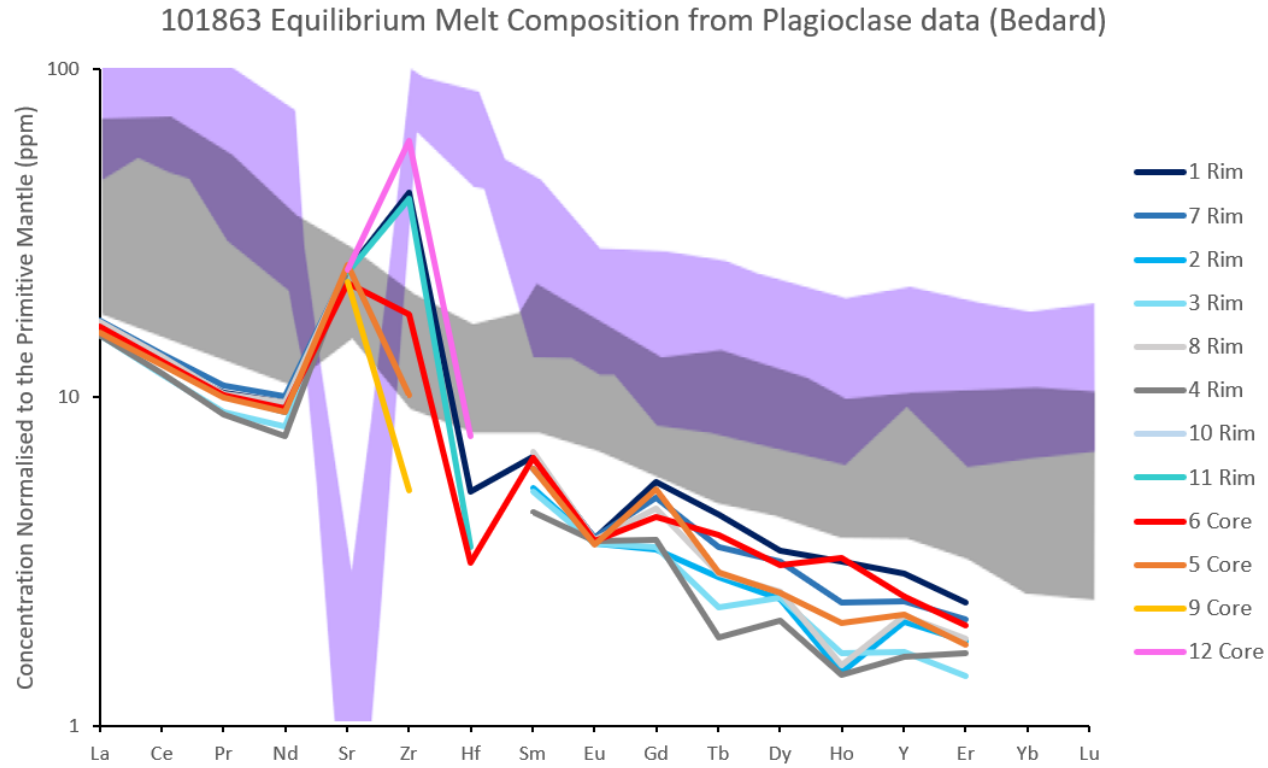
101863 Equilibrium Melt Composition from Plagioclase data (Bedard)
Concentration Normalised to the Primitive Mantle (ppm)
100
10
1
La
Ce
Pr
Nd
Sr
Zr
Hf
Sm
Eu
Gd
Tb
Dy
Ho
Y
Er
Yb
Lu
1 Rim
7 Rim
2 Rim
3 Rim
8 Rim
4 Rim
10 Rim
11 Rim
6 Core
5 Core
9 Core
12 Core

b)

Figure 40: Diagrams of trace element concentration data normalised to the primitive mantle for equilibrium melt compositions calculated from plagioclase data for sample 101863, superimposed on basaltic (grey field) and trachytic (purple field) fields created from published post-shield basaltic and trachytic volcanic whole rock data downloaded from the GEOROC database (see full references from page 21). Trace element data was normalised to the primitive mantle using primitive mantle values given by McDonough and Sun (1995). Blue-grey lines represent crystal rims, and yellow-red lines represent crystal cores. The equilibrium melt composition in a) was calculated using partition coefficients calculated using Sun et al. (2017) and Shannon (1976). The equilibrium melt composition in b) was calculated using partition coefficients calculated using Bédard (2006).

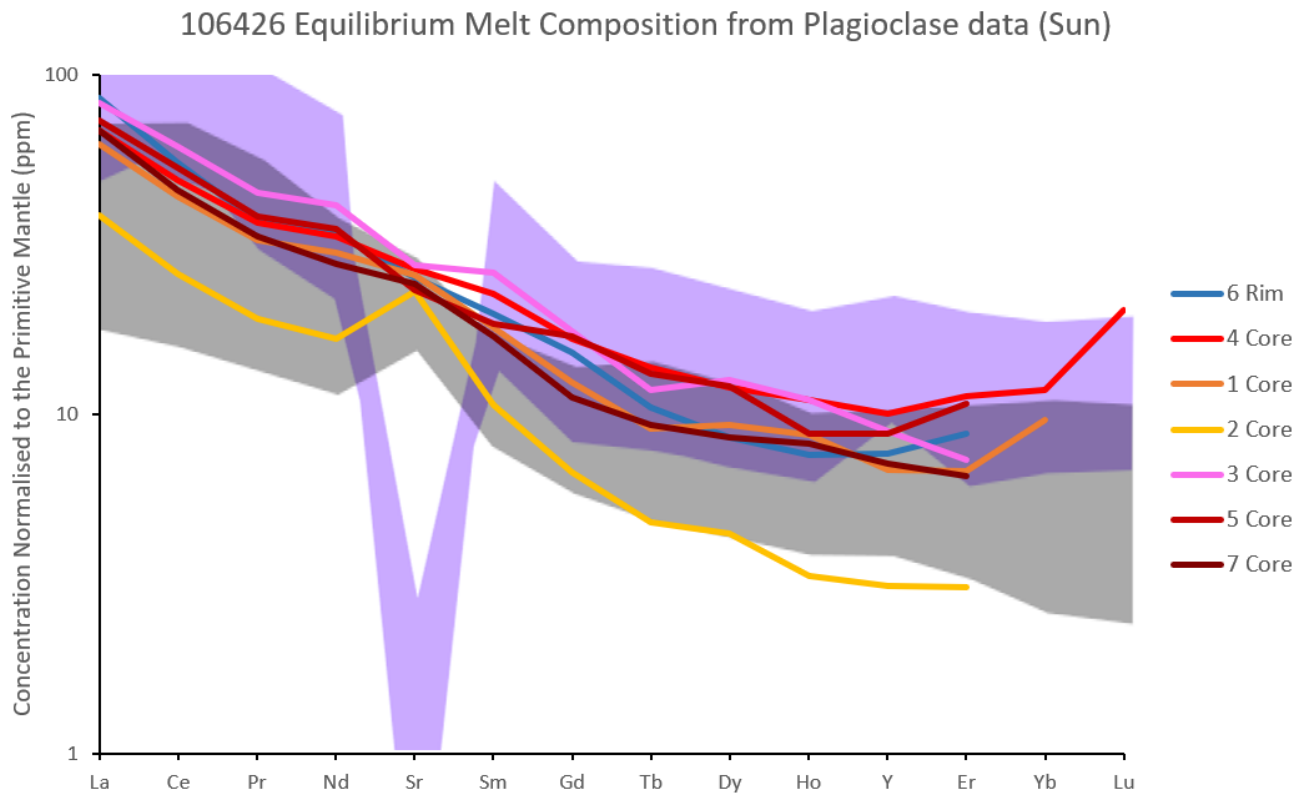

a)

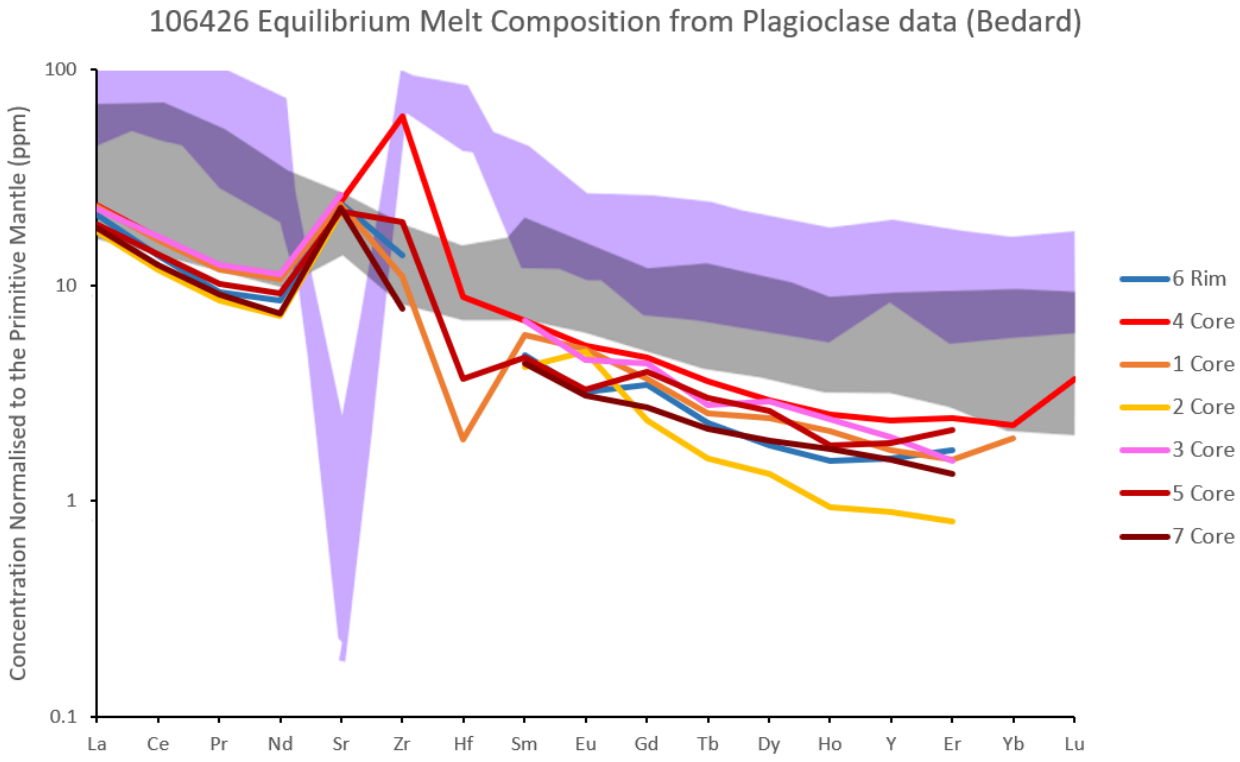

b)

Figure 41: Diagrams of trace element concentration data normalised to the primitive mantle for equilibrium melt compositions calculated from plagioclase data for sample 106426, superimposed on basaltic (grey field) and trachytic (purple field) fields created from published post-shield basaltic and trachytic volcanic whole rock data downloaded from the GEOROC database (see full references from page 21). Trace element data was normalised to the primitive mantle using primitive mantle values given by McDonough and Sun (1995). Blue-grey lines represent crystal rims, and yellow-red lines represent crystal cores. The equilibrium melt composition in a) was calculated using partition coefficients calculated using Sun et al. (2017) and Shannon (1976). The equilibrium melt composition in b) was calculated using partition coefficients calculated using Bédard (2006).

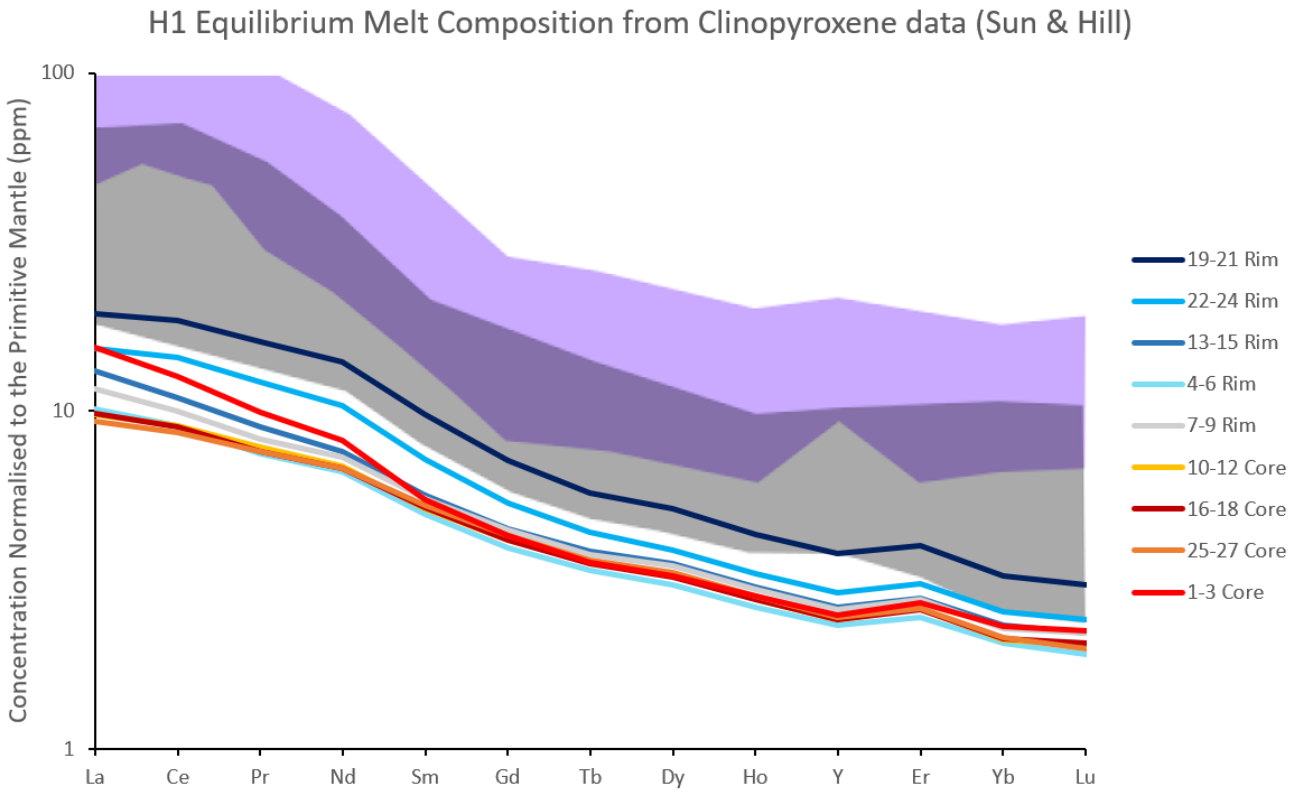
H1 Equilibrium Melt Composition from Clinopyroxene data (Sun & Hill)
Concentration Normalised to the Primitive Mantle (ppm)
100
10
1
La
Ce
Pr
Nd
Sm
Gd
Tb
Dy
Ho
Y
Er
Yb
Lu
19-21 Rim
22-24 Rim
13-15 Rim
4-6 Rim
7-9 Rim
10-12 Core
16-18 Core
25-27 Core
1-3 Core

a)

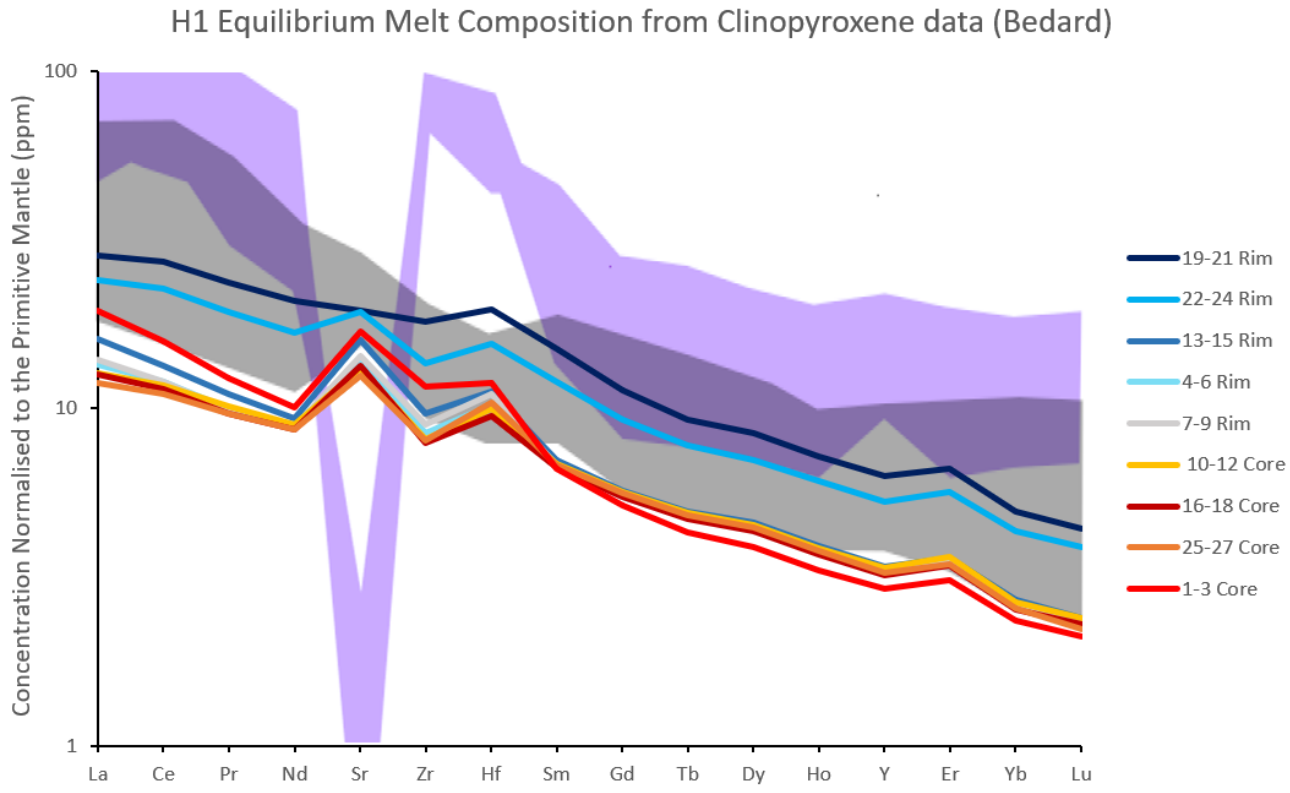
H1 Equilibrium Melt Composition from Clinopyroxene data (Bedard)
Concentration Normalised to the Primitive Mantle (ppm)
100
10
1
La
Ce
Pr
Nd
Sr
Zr
Hf
Sm
Gd
Tb
Dy
Ho
Y
Er
Yb
Lu
19-21 Rim
22-24 Rim
13-15 Rim
4-6 Rim
7-9 Rim
10-12 Core
16-18 Core
25-27 Core
1-3 Core

b)

Figure 42: Diagrams of trace element concentration data normalised to the primitive mantle for equilibrium melt compositions calculated from clinopyroxene data for sample H1, superimposed on basaltic (grey field) and trachytic (purple field) fields created from published post-shield basaltic and trachytic volcanic whole rock data downloaded from the GEOROC database (see full references from page 21). Trace element data was normalised to the primitive mantle using primitive mantle values given by McDonough and Sun (1995). Blue-grey lines represent crystal rims, and yellow-red lines represent crystal cores. The equilibrium melt composition in a) was calculated using partition coefficients calculated using Sun and Liang (2012), Hill et al. (2011, 2012) and Shannon (1976). The equilibrium melt composition in b) was calculated using partition coefficients found using methods from Bédard (2014).

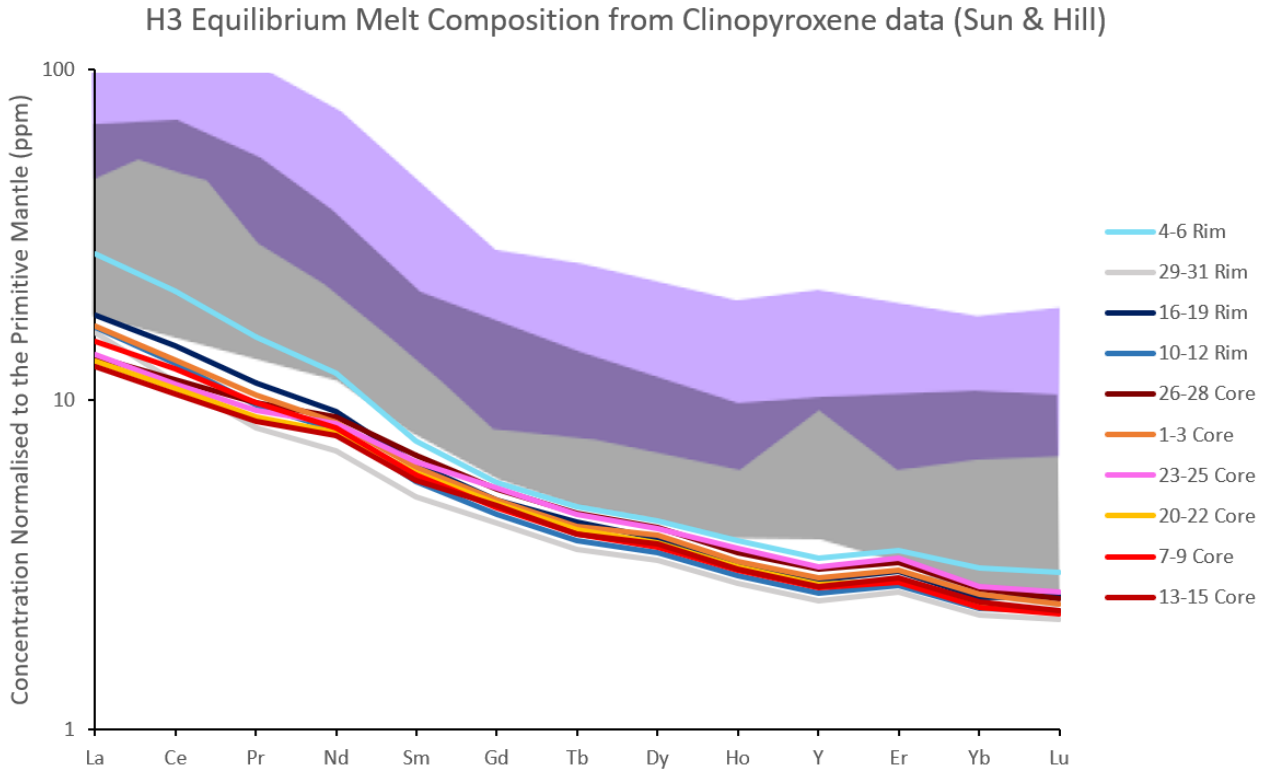

a)

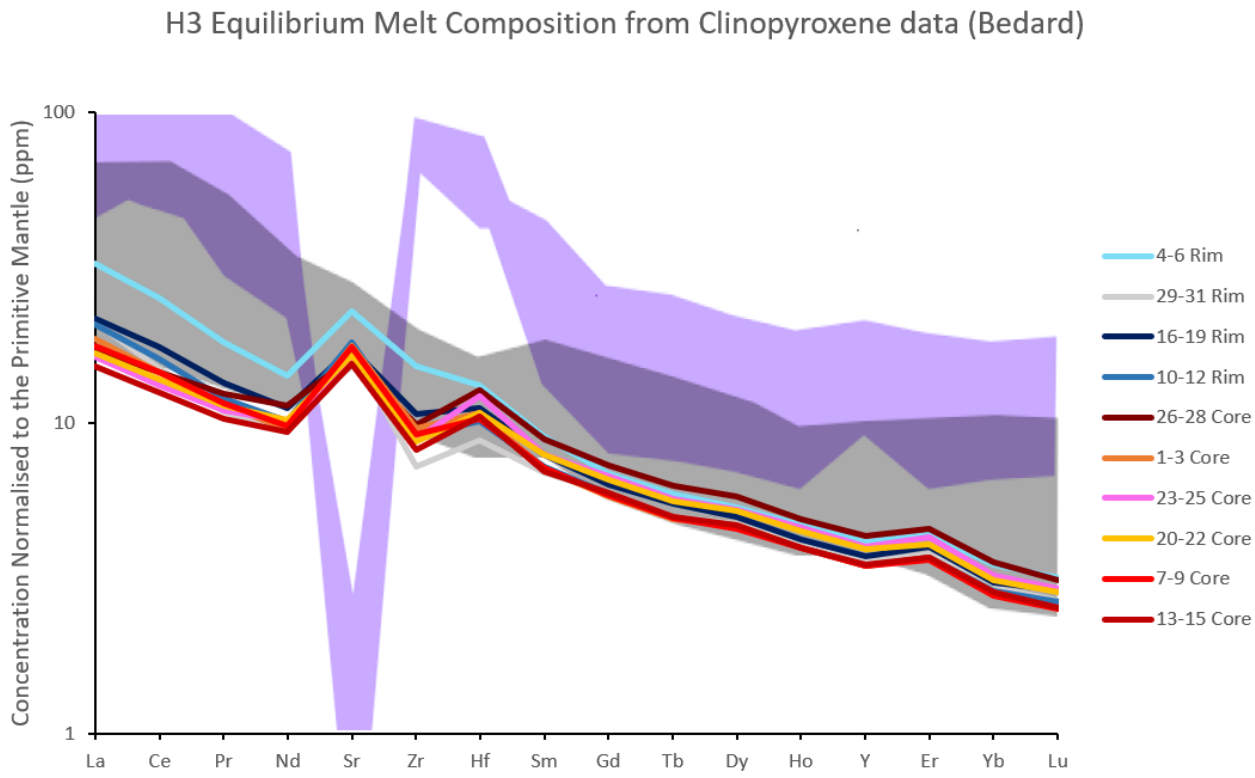

b)

Figure 43: Diagrams of trace element concentration data normalised to the primitive mantle for equilibrium melt compositions calculated from clinopyroxene data for sample H3, superimposed on basaltic (grey field) and trachytic (purple field) fields created from published post-shield basaltic and trachytic volcanic whole rock data downloaded from the GEOROC database (see full references from page 21). Trace element data was normalised to the primitive mantle using primitive mantle values given by McDonough and Sun (1995). Blue-grey lines represent crystal rims, and yellow-red lines represent crystal cores. The equilibrium melt composition in a) was calculated using partition coefficients calculated using Sun and Liang (2012), Hill et al. (2011, 2012) and Shannon (1976). The equilibrium melt composition in b) was calculated using partition coefficients found using methods from Bédard (2014).

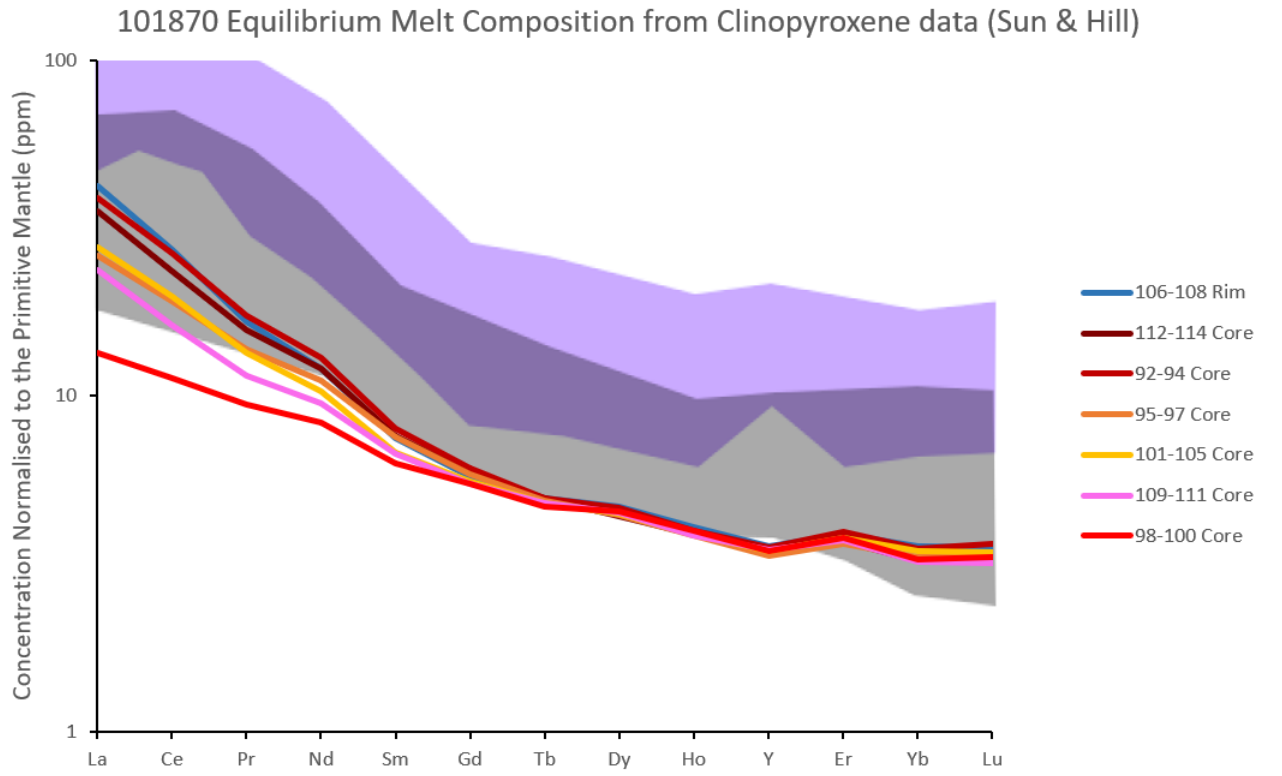
101870 Equilibrium Melt Composition from Clinopyroxene data (Sun & Hill)
Concentration Normalised to the Primitive Mantle (ppm)
100
10
1
La
Ce
Pr
Nd
Sm
Gd
Tb
Dy
Ho
Y
Er
Yb
Lu
106-108 Rim
112-114 Core
92-94 Core
95-97 Core
101-105 Core
109-111 Core
98-100 Core

a)

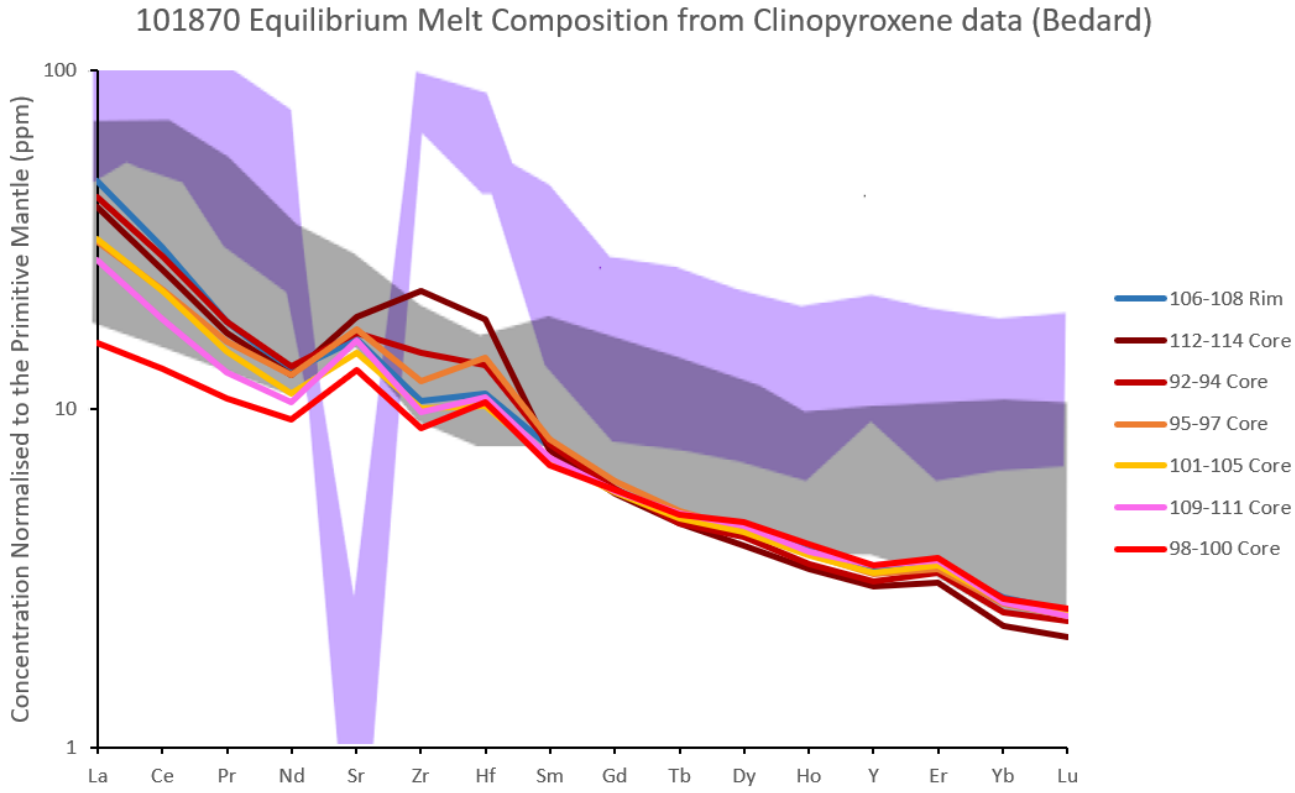
101870 Equilibrium Melt Composition from Clinopyroxene data (Bedard)
Concentration Normalised to the Primitive Mantle (ppm)
100
10
1
La
Ce
Pr
Nd
Sr
Zr
Hf
Sm
Gd
Tb
Dy
Ho
Y
Er
Yb
Lu
106-108 Rim
112-114 Core
92-94 Core
95-97 Core
101-105 Core
109-111 Core
98-100 Core

b)

Figure 44: Diagrams of trace element concentration data normalised to the primitive mantle for equilibrium melt compositions calculated from clinopyroxene data for sample 101870, superimposed on basaltic (grey field) and trachytic (purple field) fields created from published post-shield basaltic and trachytic volcanic whole rock data downloaded from the GEOROC database (see full references from page 21). Trace element data was normalised to the primitive mantle using primitive mantle values given by McDonough and Sun (1995). Blue-grey lines represent crystal rims, and yellow-red lines represent crystal cores. The equilibrium melt composition in a) was calculated using partition coefficients calculated using Sun and Liang (2012), Hill et al. (2011, 2012) and Shannon (1976). The equilibrium melt composition in b) was calculated using partition coefficients found using methods from Bédard (2014).

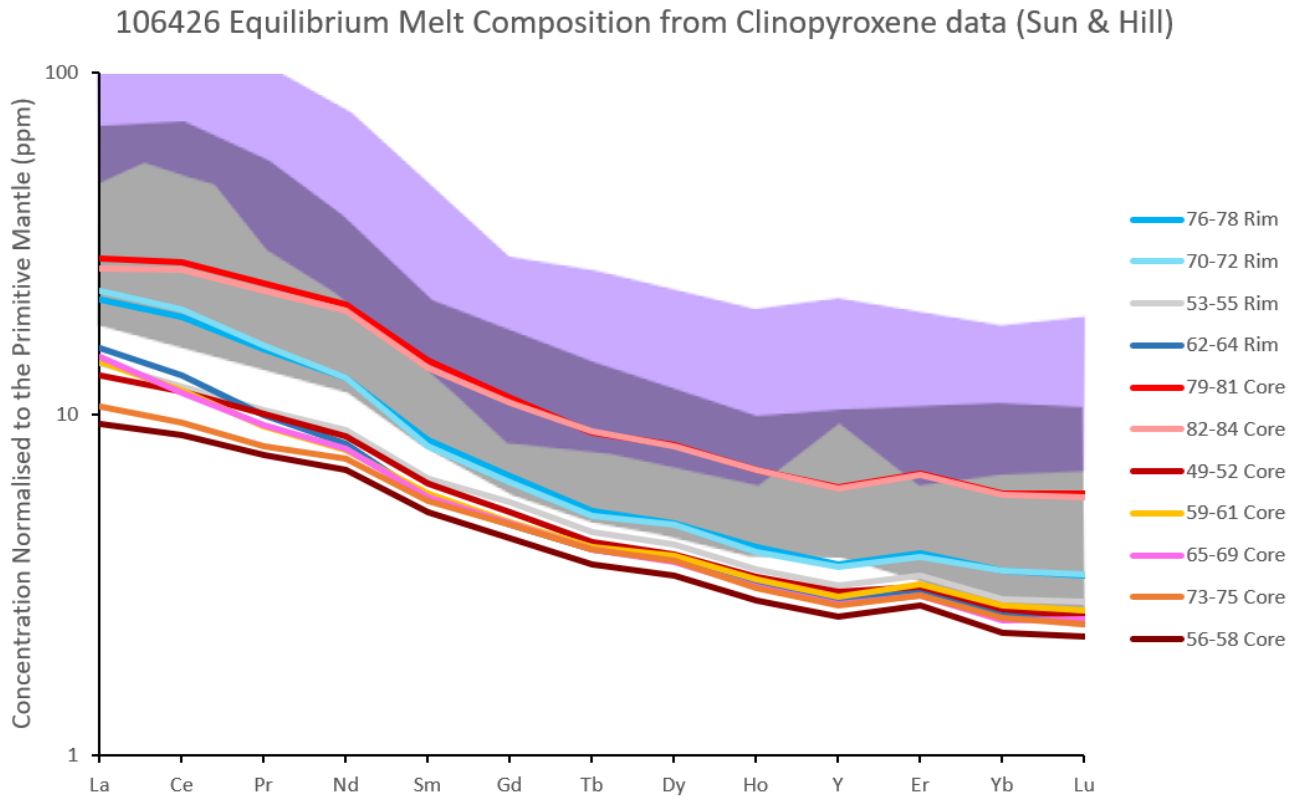

a)

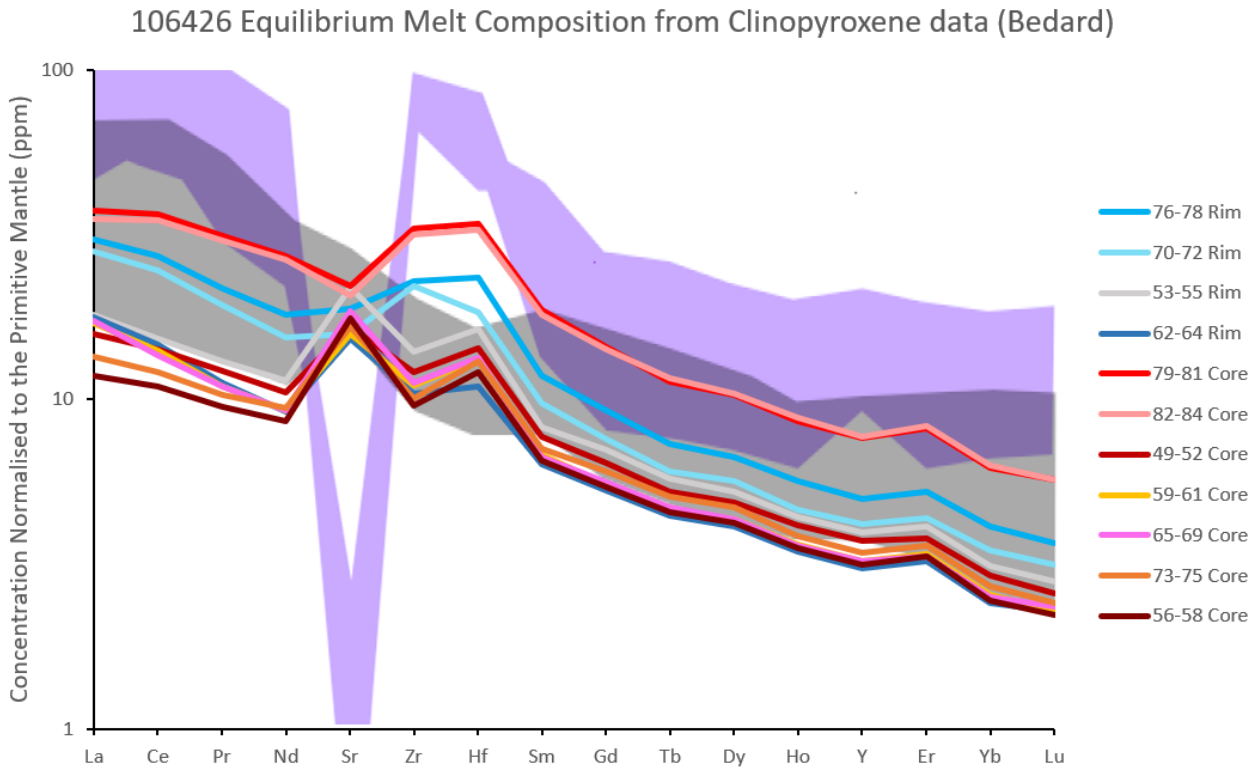

b)

Figure 45: Diagrams of trace element concentration data normalised to the primitive mantle for equilibrium melt compositions calculated from clinopyroxene data for sample 106426, superimposed on basaltic (grey field) and trachytic (purple field) fields created from published post-shield basaltic and trachytic volcanic whole rock data downloaded from the GEOROC database (see full references from page 21). Trace element data was normalised to the primitive mantle using primitive mantle values given by McDonough and Sun (1995). Blue-grey lines represent crystal rims, and yellow-red lines represent crystal cores. The equilibrium melt composition in a) was calculated using partition coefficients calculated using Sun and Liang (2012), Hill et al. (2011, 2012) and Shannon (1976). The equilibrium melt composition in b) was calculated using partition coefficients found using methods from Bédard (2014).

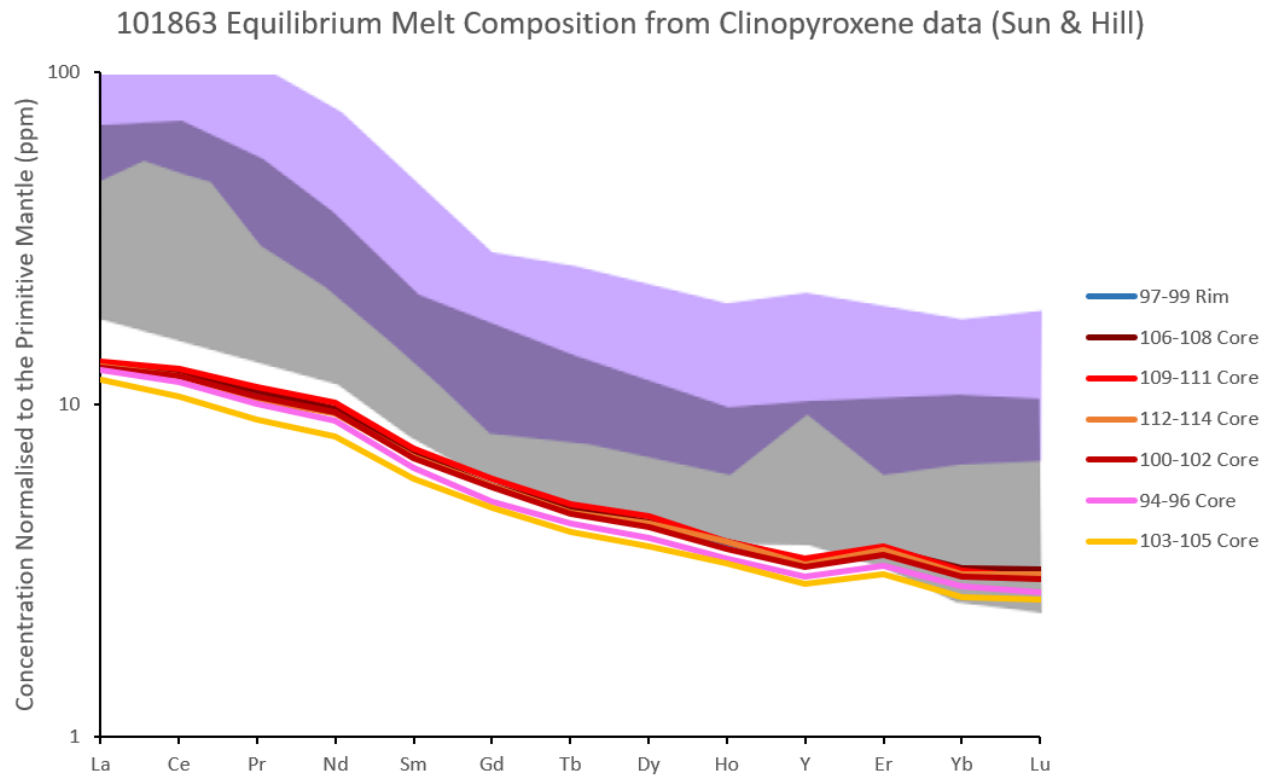
101863 Equilibrium Melt Composition from Clinopyroxene data (Sun & Hill)
Concentration Normalised to the Primitive Mantle (ppm)
100
10
1
La
Ce
Pr
Nd
Sm
Gd
Tb
Dy
Ho
Y
Er
Yb
Lu
97-99 Rim
106-108 Core
109-111 Core
112-114 Core
100-102 Core
94-96 Core
103-105 Core

a)

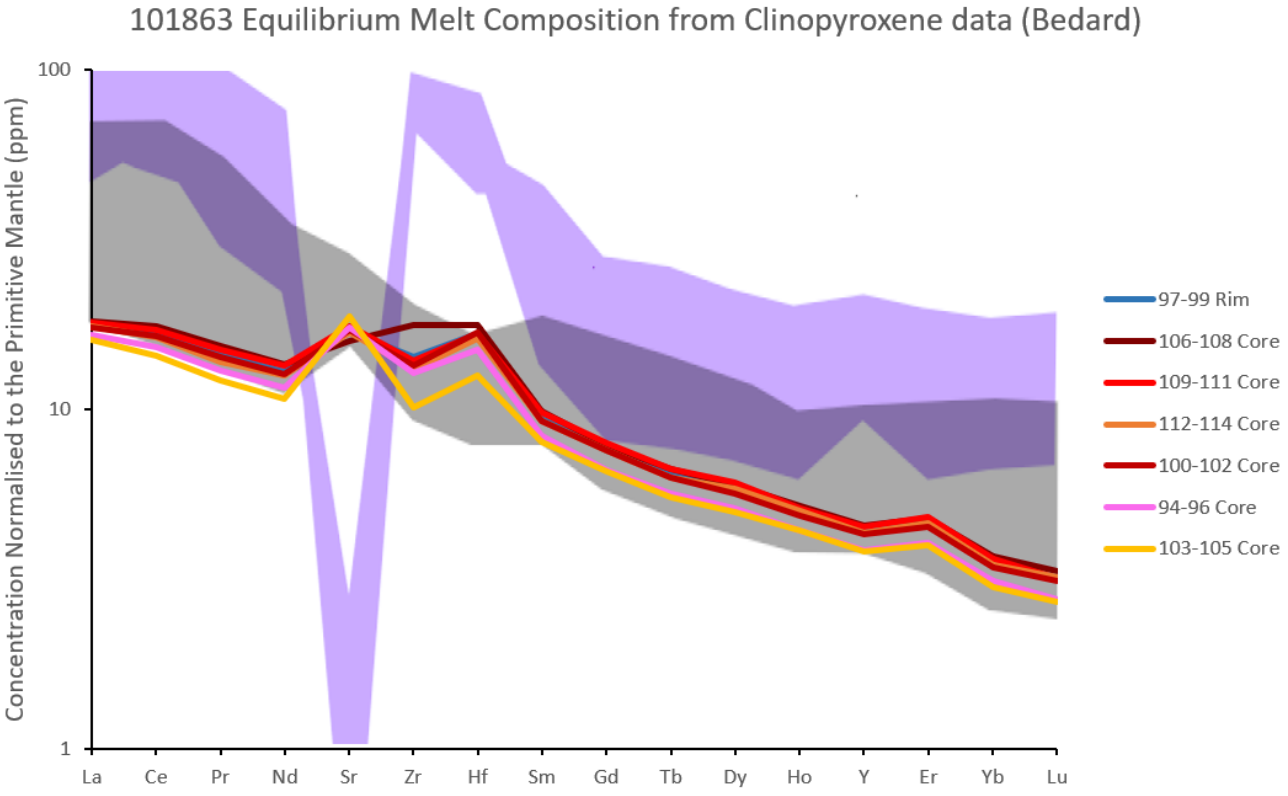
101863 Equilibrium Melt Composition from Clinopyroxene data (Bedard)
Concentration Normalised to the Primitive Mantle (ppm)
100
10
1
La
Ce
Pr
Nd
Sr
Zr
Hf
Sm
Gd
Tb
Dy
Ho
Y
Er
Yb
Lu
97-99 Rim
106-108 Core
109-111 Core
112-114 Core
100-102 Core
94-96 Core
103-105 Core

b)

Figure 46: Diagrams of trace element concentration data normalised to the primitive mantle for equilibrium melt compositions calculated from clinopyroxene data for sample 101863, superimposed on basaltic (grey field) and trachytic (purple field) fields created from published post-shield basaltic and trachytic volcanic whole rock data downloaded from the GEOROC database (see full references from page 21). Trace element data was normalised to the primitive mantle using primitive mantle values given by McDonough and Sun (1995). Blue-grey lines represent crystal rims, and yellow-red lines represent crystal cores. The equilibrium melt composition in a) was calculated using partition coefficients calculated using Sun and Liang (2012), Hill et al. (2011, 2012) and Shannon (1976). The equilibrium melt composition in b) was calculated using partition coefficients found using methods from Bédard (2014).

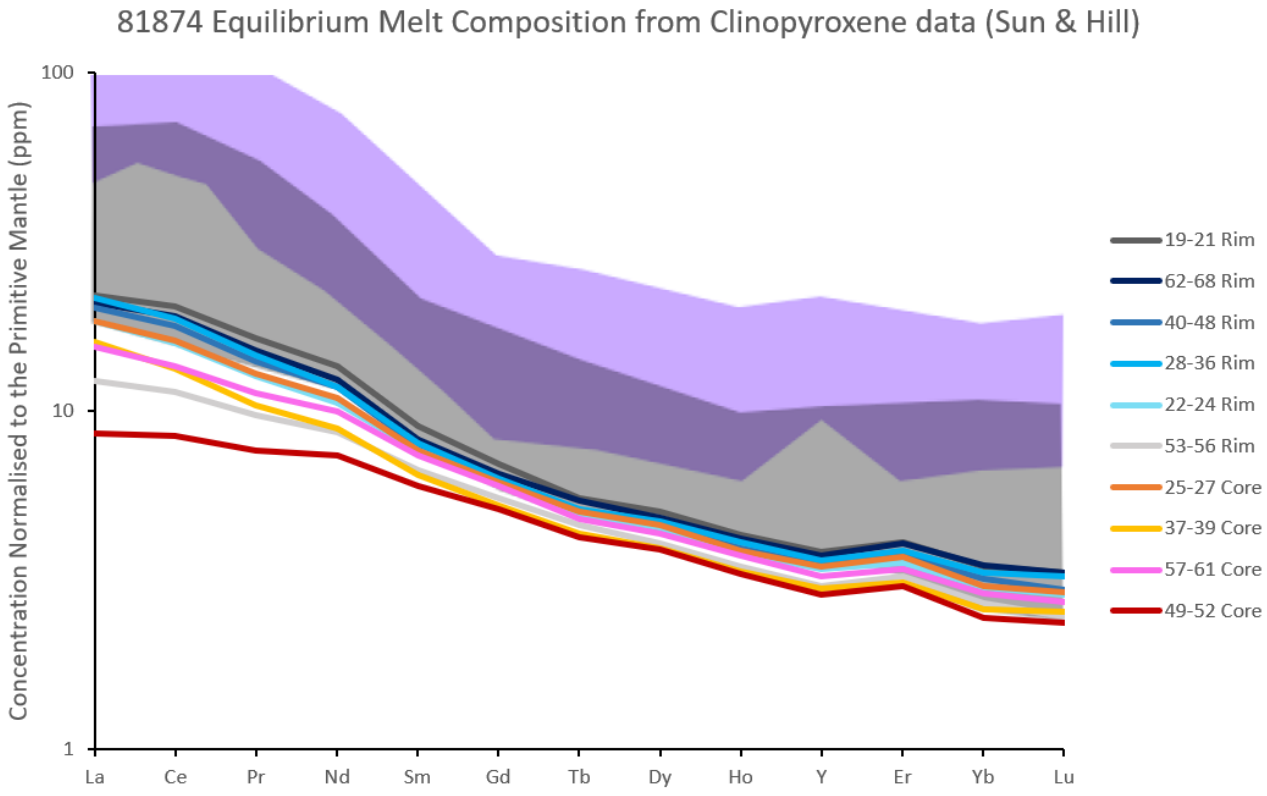

a)

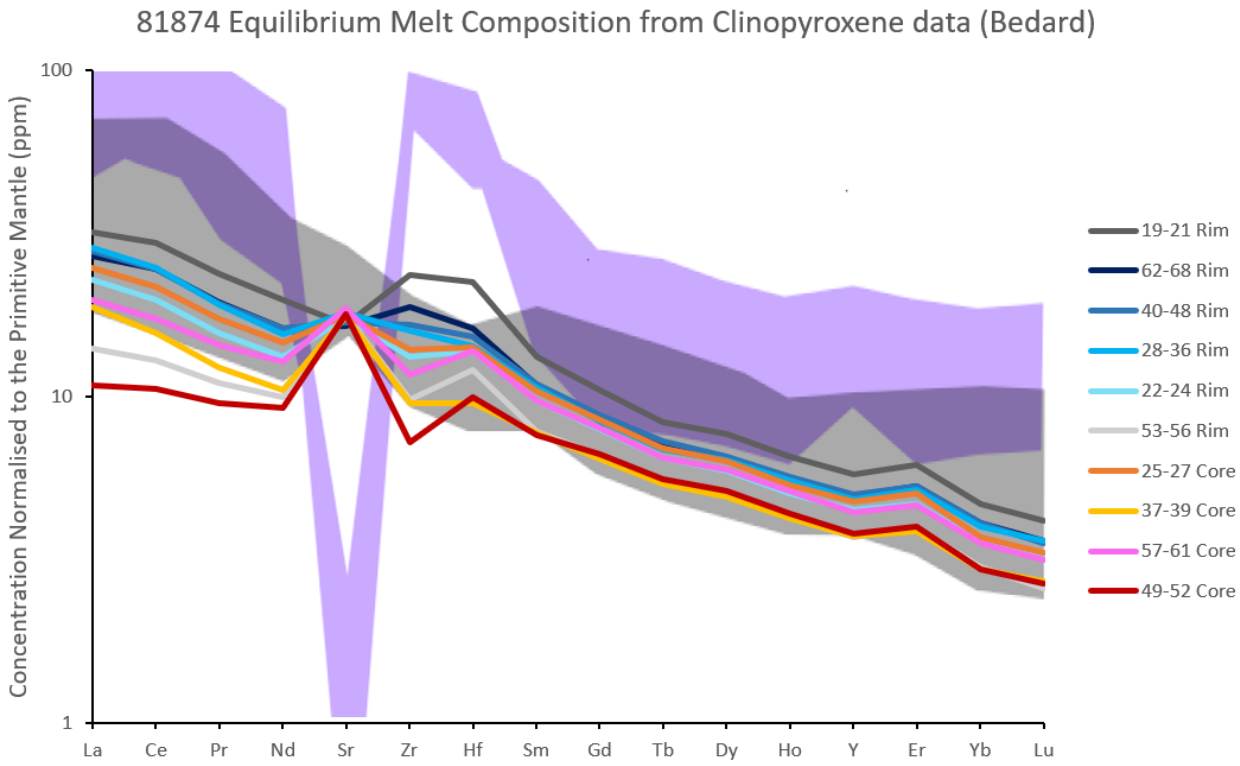

b)

Figure 47: Diagrams of trace element concentration data normalised to the primitive mantle for equilibrium melt compositions calculated from clinopyroxene data for sample 81874, superimposed on basaltic (grey field) and trachytic (purple field) fields created from published post-shield basaltic and trachytic volcanic whole rock data downloaded from the GEOROC database (see full references from page 21). Trace element data was normalised to the primitive mantle using primitive mantle values given by McDonough and Sun (1995). Blue-grey lines represent crystal rims, and yellow-red lines represent crystal cores. The equilibrium melt composition in a) was calculated using partition coefficients calculated using Sun and Liang (2012), Hill et al. (2011, 2012) and Shannon (1976). The equilibrium melt composition in b) was calculated using partition coefficients found using methods from Bédard (2014).

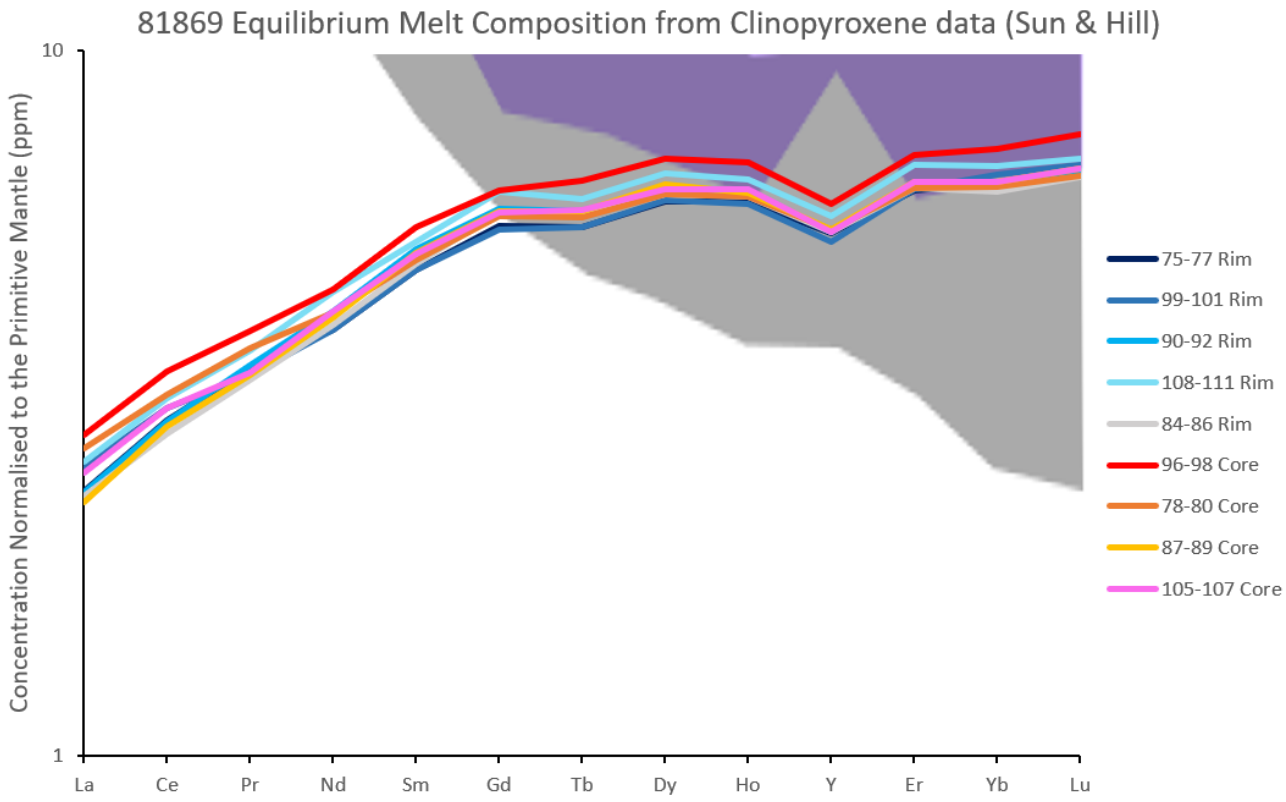
81869 Equilibrium Melt Composition from Clinopyroxene data (Sun & Hill)
Concentration Normalised to the Primitive Mantle (ppm)
10
1
La
Ce
Pr
Nd
Sm
Gd
Tb
Dy
Ho
Y
Er
Yb
Lu
75-77 Rim
99-101 Rim
90-92 Rim
108-111 Rim
84-86 Rim
96-98 Core
78-80 Core
87-89 Core
105-107 Core

a)

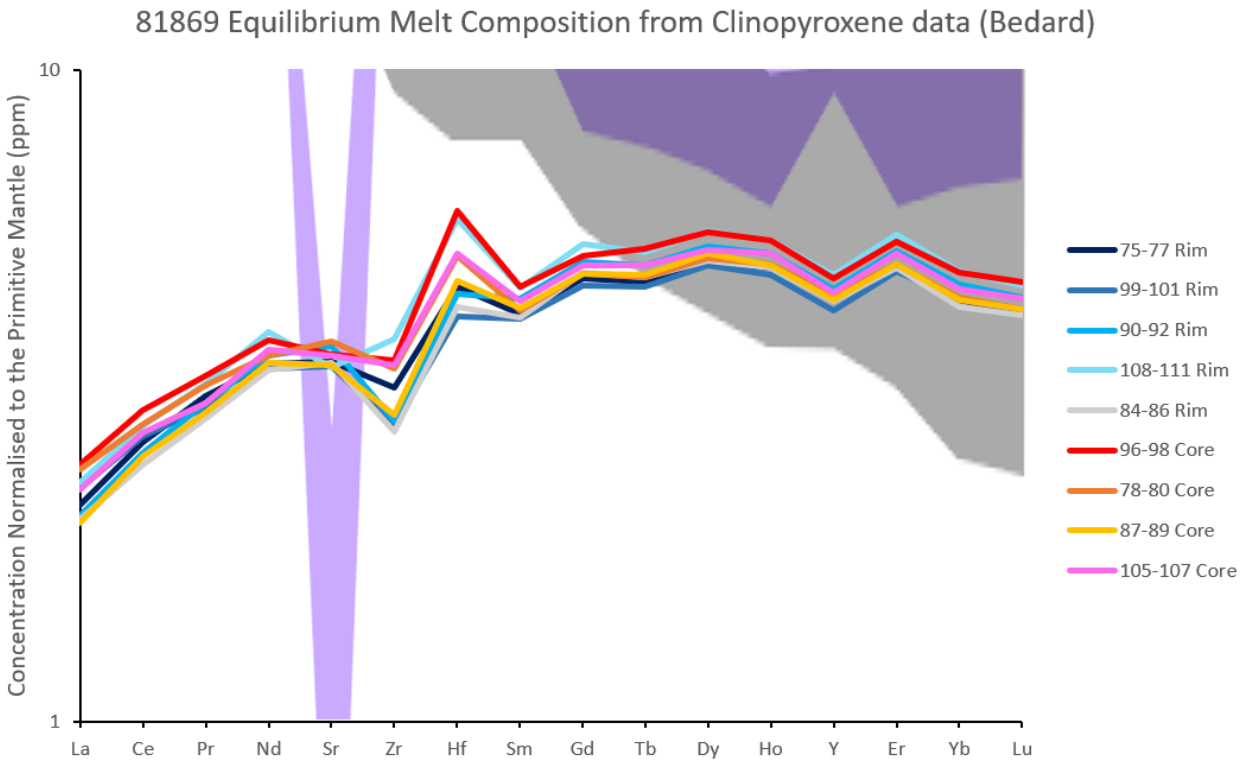
81869 Equilibrium Melt Composition from Clinopyroxene data (Bedard)
Concentration Normalised to the Primitive Mantle (ppm)
10
1
La
Ce
Pr
Nd
Sr
Zr
Hf
Sm
Gd
Tb
Dy
Ho
Y
Er
Yb
Lu
75-77 Rim
99-101 Rim
90-92 Rim
108-111 Rim
84-86 Rim
96-98 Core
78-80 Core
87-89 Core
105-107 Core

b)

Figure 48: Diagrams of trace element concentration data normalised to the primitive mantle for equilibrium melt compositions calculated from clinopyroxene data for sample 81869, superimposed on basaltic (grey field) and trachytic (purple field) fields created from published post-shield basaltic and trachytic volcanic whole rock data downloaded from the GEOROC database (see full references from page 21). Trace element data was normalised to the primitive mantle using primitive mantle values given by McDonough and Sun (1995). Blue-grey lines represent crystal rims, and yellow-red lines represent crystal cores. The equilibrium melt composition in a) was calculated using partition coefficients calculated using Sun and Liang (2012), Hill et al. (2011, 2012) and Shannon (1976). The equilibrium melt composition in b) was calculated using partition coefficients found using methods from Bédard (2014).

Figures 39 a), 40 a) and 41 a) show the trace element concentrations of a parental melt calculated from the plagioclase data collected in this study using partition coefficients produced by Sun et al. (2017) and Shannon (1976). In these graphs, the samples seem to lie between the basaltic and trachytic fields. Figures 39 b), 40 b) and 41 b) also show the trace element concentrations of a parental melt calculated from the plagioclase data collected in this study, but using partition coefficients produced by Bédard (2006). The graphs using Bédard (2006) reveal concentrations that have a similar slope to the basaltic field. This suggests that the plagioclase parental melt trace element concentrations are very sensitive to the partition coefficients used, making it difficult to reliably use plagioclase data to make conclusions about the nature of the samples.

Sample 81869 represents MORB (see discussion), however primitive mantle-normalised trace element concentration diagrams for the equilibrium melt composition of this sample created using plagioclase data do not show the typical trace element depletion pattern expected of a MORB sample; this is the case for primitive mantle-normalised trace element concentration diagrams of equilibrium melt concentrations calculated from plagioclase data using partition coefficients from both Bédard (2006) and by Sun et al. (2017) and Shannon (1976) (figs. 38 b) & 38 a) respectively). Primitive mantle-normalised trace element concentration diagrams of the equilibrium melt composition of sample 81869 calculated from clinopyroxene data, however, do show an appropriate pattern of trace element depletion using both Bédard (2014) and Sun and Liang (2012), Hill et al. (2011, 2012) and

Shannon (1976). In fact, many samples reveal differences in the calculated equilibrium melt trace element concentrations from clinopyroxene and plagioclase data respectively. These differences between clinopyroxene and plagioclase graphs could suggest that either:

I) Plagioclase crystals may have crystallised from a different melt than the clinopyroxene crystals.

ii) Diffusion post-formation may have influenced the trace element composition of various minerals; trace elements diffuse faster in plagioclase than in clinopyroxene ((Van Orman et al. , 2001; Cherniak, 2003), so trace element signatures in these samples may have been modified by trace element diffusion in the plagioclase crystals.

iii) The partition coefficients used to calculate the equilibrium melt compositions from plagioclase data are not accurate enough to produce reasonable results.

Point iii) is the most likely cause because, as mentioned above, the differences produced by using different partition coefficients (from Bédard (2006) and from Sun et al. (2017) and Shannon (1976)) show that the plagioclase data is very sensitive to changes in partition coefficient, resulting in concentrations varying greatly between the basaltic and trachytic field. The large effect of partition coefficient on the interpretation of the plagioclase results means that the plagioclase results are unreliable.

The greater difference in trace element concentrations found between the parental melt primitive mantle-normalised trace element concentration diagrams from plagioclase data created using Bédard (2006) and by Sun et al. (2017) and Shannon (1976), relative to the small difference between those from clinopyroxene data using Bédard (2014) and Sun and Liang (2012), Hill et al. (2011, 2012) and Shannon (1976) suggests that plagioclase is far more sensitive to partition coefficients than clinopyroxene. Furthermore, the plagioclase primitive mantle-normalised trace element concentration diagrams for MORB sample 81869 (see discussion), show trends unlike those of traditional MORB parent melts (see fig. 38) – potentially as a result of secondary processes such as post-formation diffusion in plagioclase (point ii) mentioned above) - unlike clinopyroxene primitive mantle-normalised trace element concentration diagrams which do show expected MORB trends (see fig. 48). In

effect, this suggests that, despite being unable to rely on plagioclase data, the clinopyroxene data is likely still reliable.

In conclusion, the partition coefficients for plagioclase calculated from Bédard (2006) and from Sun et al. (2017) and Shannon (1976) are not robust enough to come up with an interpretation of the significance of the plagioclase data. This, combined with the possibility of more rapid post-formation diffusion in plagioclase relative to clinopyroxene, and the lower concentrations of most trace elements in the plagioclase data relative to the clinopyroxene data (which increases the analytical uncertainty of the plagioclase data relative to the clinopyroxene data), raises further doubts regarding the ability to use measured plagioclase compositions to reconstruct the original trace element composition of the parent melt. As a result, the uncertainty in the plagioclase data is too great for the data to be used with any confidence. However, the smaller degree of variability in calculated clinopyroxene parental melt compositions using Bédard (2014) and Sun and Liang (2012), Hill et al. (2011, 2012) and Shannon (1976), paired with slower post-formation trace element diffusivities and higher measured trace element concentrations, indicate that clinopyroxene data could be used more reliably to interpret parental melt compositions.

For the discussion (figs. 49 and 50), the data from parental melts that were calculated from clinopyroxene data using partition coefficients from Bédard (2014) were used, as this model provided a greater range of trace elements to analyse.

In the graphs of equilibrium melt compositions calculated from clinopyroxene data, it is interesting to note that location 1-3 in sample H1 (see fig. 42) has a clearly different gradient to that of the other samples. Similarly, sample 101870 shows that all sampled locations have different gradients (see fig. 44).

To study the trace element heterogeneity of the samples used in this study relative to published basaltic lavas, the trace element ratios of the equilibrium melt composition data from this study were plotted alongside both the modelled path for fractional crystallisation for basaltic lavas and the published basaltic and trachytic post-shield data and shield-stage picrite data downloaded from the GEOROC database (see full references from page 61). The data from this study's samples appears to be distinct from the published trachytic lava

array, having lower absolute trace element concentrations than the trachytes. For example, in figure 49 a), trachytic Ce values extend above 50ppm, whereas the samples from this study sit below 37ppm. In figure 49 c) this difference is even clearer, with trachitic data lying above 70ppm of Zr and the data from this study lying below 33ppm.

Despite this, sample 101870 does not follow the trend of the basaltic array nor the modelled path of fractional crystallisation for a basaltic lava, extending to much higher Ce/Y (see fig. 49 a)), La/Sm (see fig. 49 b)) and Zr/Sm (see fig. 49 c)) values than any other sample.

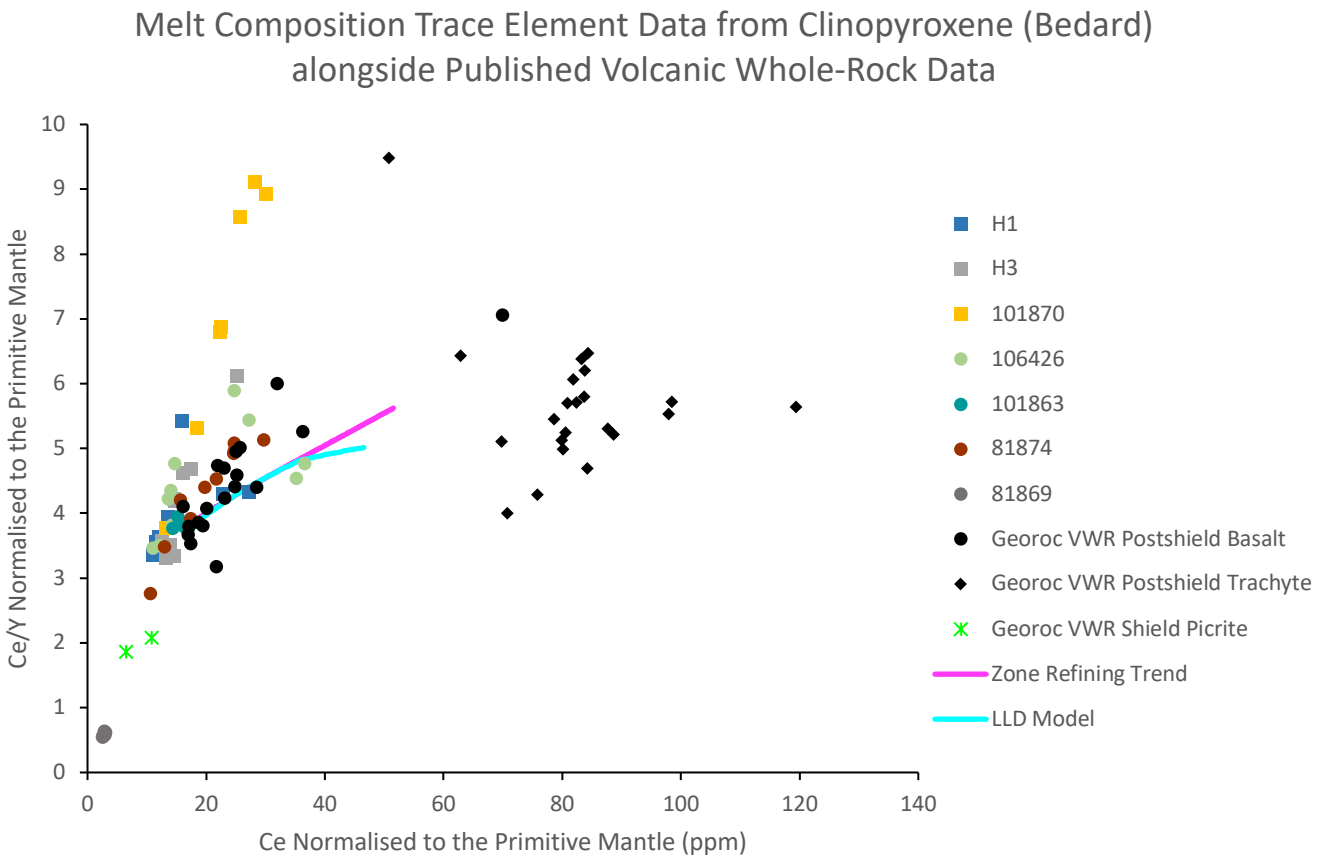

a)

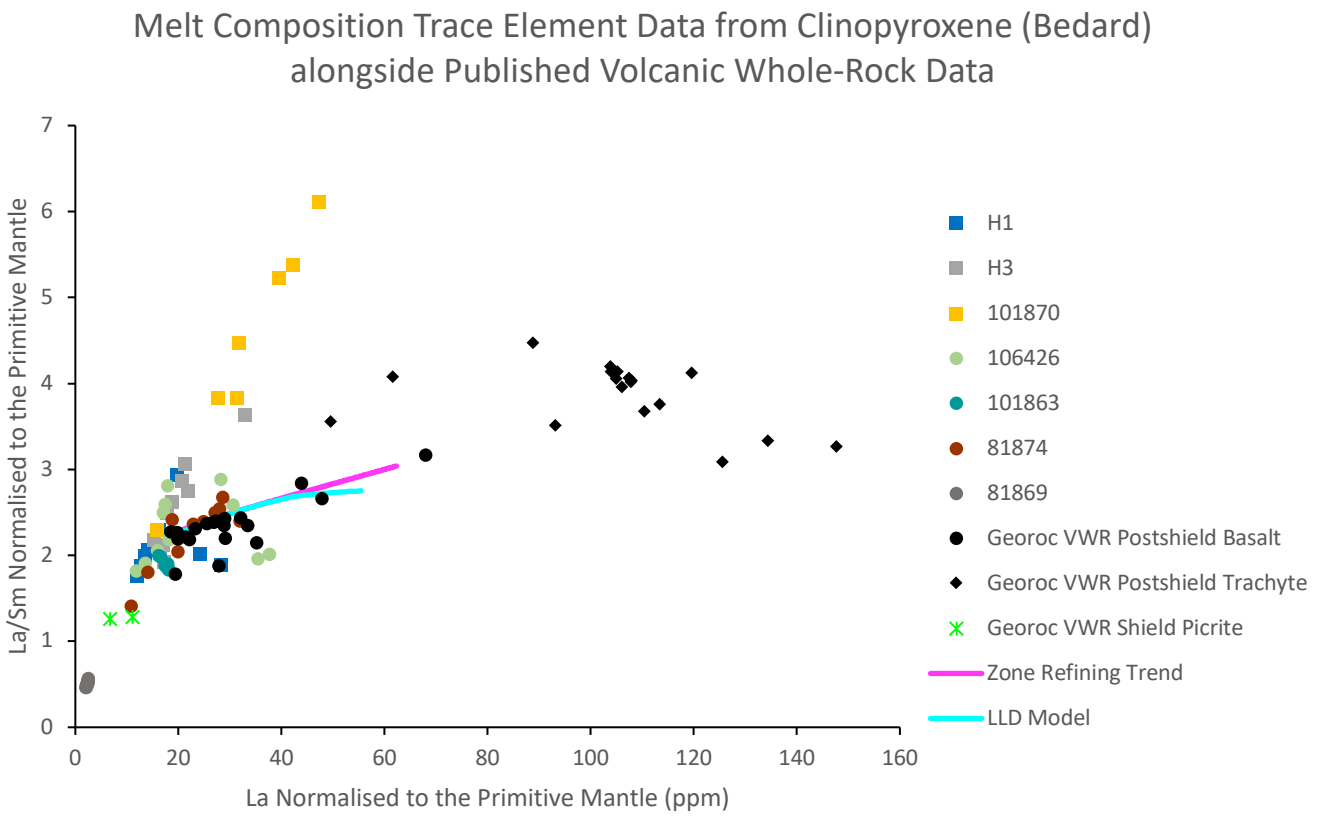
Melt Composition Trace Element Data from Clinopyroxene (Bedard) alongside Published Volcanic Whole-Rock Data
La/Sm Normalised to the Primitive Mantle
La Normalised to the Primitive Mantle (ppm)
0
1
2
3
4
5
6
7
0
20
40
60
80
100
120
140
160
H1
H3
101870
106426
101863
81874
81869
Georoc VWR Postshield Basalt
Georoc VWR Postshield Trachyte
Georoc VWR Shield Picrite
Zone Refining Trend
LLD Model

b)

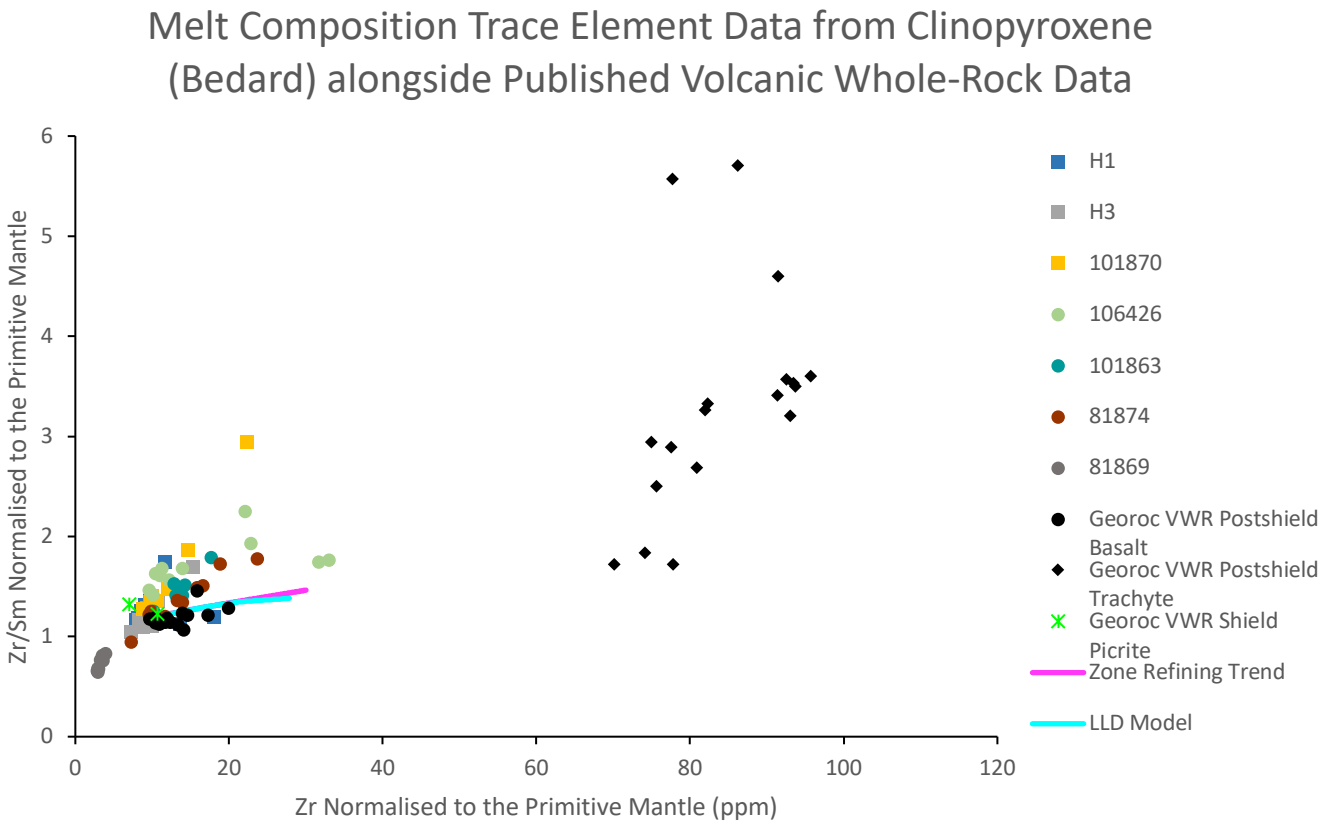
Melt Composition Trace Element Data from Clinopyroxene (Bedard) alongside Published Volcanic Whole-Rock Data
Zr/Sm Normalised to the Primitive Mantle
Zr Normalised to the Primitive Mantle (ppm)
0
1
2
3
4
5
6
0
20
40
60
80
100
120
H1
H3
101870
106426
101863
81874
81869
Georoc VWR Postshield Basalt
Georoc VWR Postshield Trachyte
Georoc VWR Shield Picrite
Zone Refining Trend
LLD Model

c)

Figure 49: Plots of trace element concentration data normalised to the primitive mantle for equilibrium melt compositions calculated from clinopyroxene data, alongside published volcanic whole rock (VWR) data for post-shield basalts (black circles), post-shield trachytes (black diamonds) and shield stage picrites (green star) downloaded from the GEOROC database (see full references from page 61). Trace element data was normalised to the primitive mantle using primitive mantle values given by McDonough and Sun (1995). Equilibrium melt compositions were calculated using partition coefficients calculated using Bédard (2014). Square symbols denote wehrlitic samples, and circular symbols denote basaltic samples. The blue line plots the modelled path of fractional crystallisation from a basaltic melt. The pink line plots the zone refining trend which models reactive melt flow. Plot a) shows the Ce/Y ratio normalised to the primitive mantle against Ce concentrations normalised to the primitive mantle. Plot b) shows the La/Sm ratio normalised to the primitive mantle against La concentrations normalised to the primitive mantle. Plot c) shows the Zr/Sm ratio normalised to the primitive mantle against Zr concentrations normalised to the primitive mantle.

Finally, to compare the isotopic heterogeneity of the samples from this study with that of published data, the $^{87}Sr/^{86}Sr$ of the samples was plotted alongside that of published trachytic and basaltic post-shield data downloaded from the GEOROC database (see full references from page 21). In these plots, it is interesting to note that the isotopic range of the samples in this study is greater than that of published basaltic post-shield lavas downloaded from the GEOROC database, extending to greater $^{87}Sr/^{86}Sr$ values. In 49 a) and b), it also appears that some samples approach the array of published trachytic post-shield lavas downloaded from the GEOROC database, in particular, sample 101870.

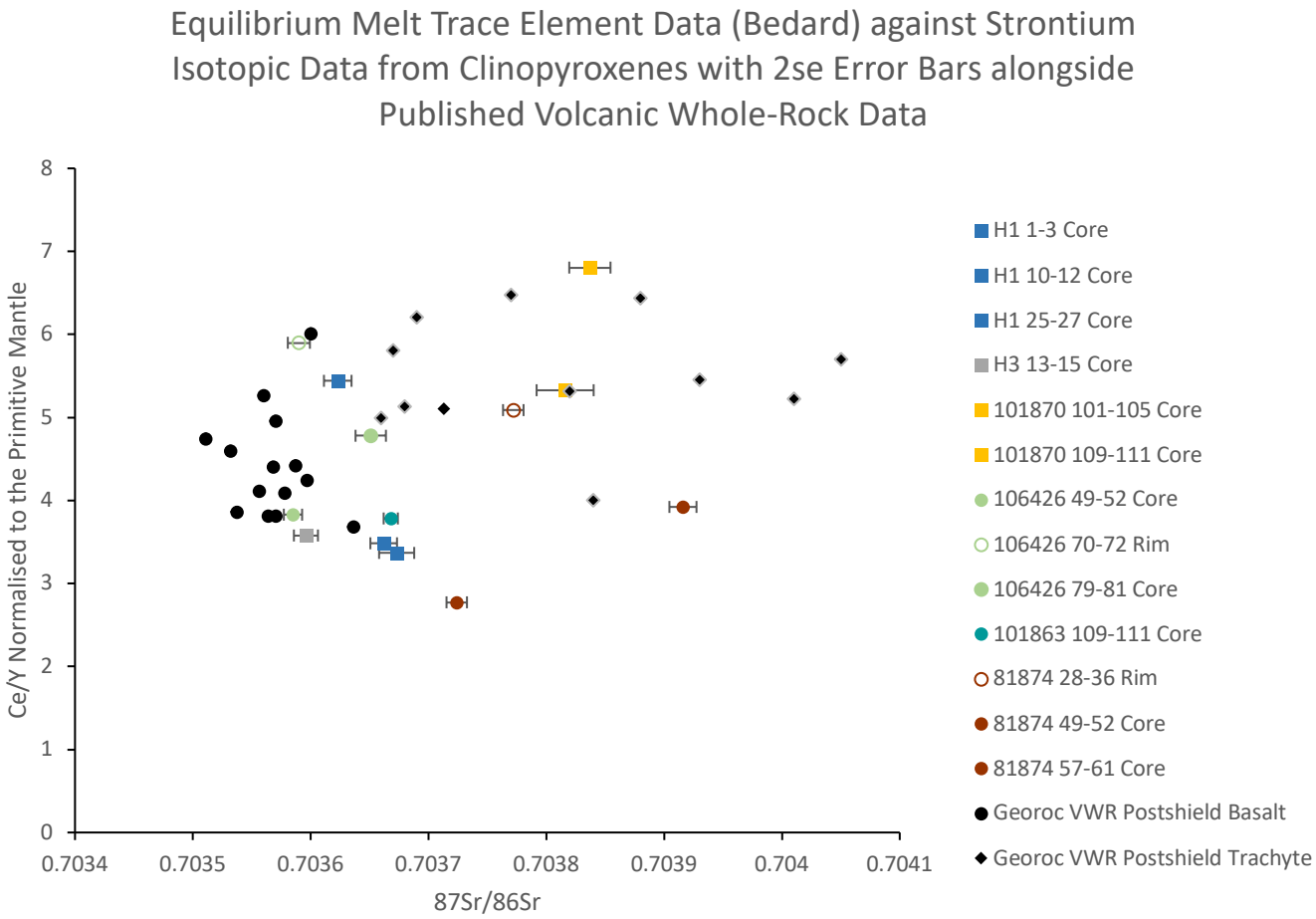
Equilibrium Melt Trace Element Data (Bedard) against Strontium Isotopic Data from Clinopyroxenes with 2se Error Bars alongside Published Volcanic Whole-Rock Data
Ce/Y Normalised to the Primitive Mantle
87Sr/86Sr
0
1
2
3
4
5
6
7
8
0.7034
0.7035
0.7036
0.7037
0.7038
0.7039
0.704
0.7041
H1 1-3 Core
H1 10-12 Core
H1 25-27 Core
H3 13-15 Core
101870 101-105 Core
101870 109-111 Core
106426 49-52 Core
106426 70-72 Rim
106426 79-81 Core
101863 109-111 Core
81874 28-36 Rim
81874 49-52 Core
81874 57-61 Core
Georoc VWR Postshield Basalt
Georoc VWR Postshield Trachyte

a)

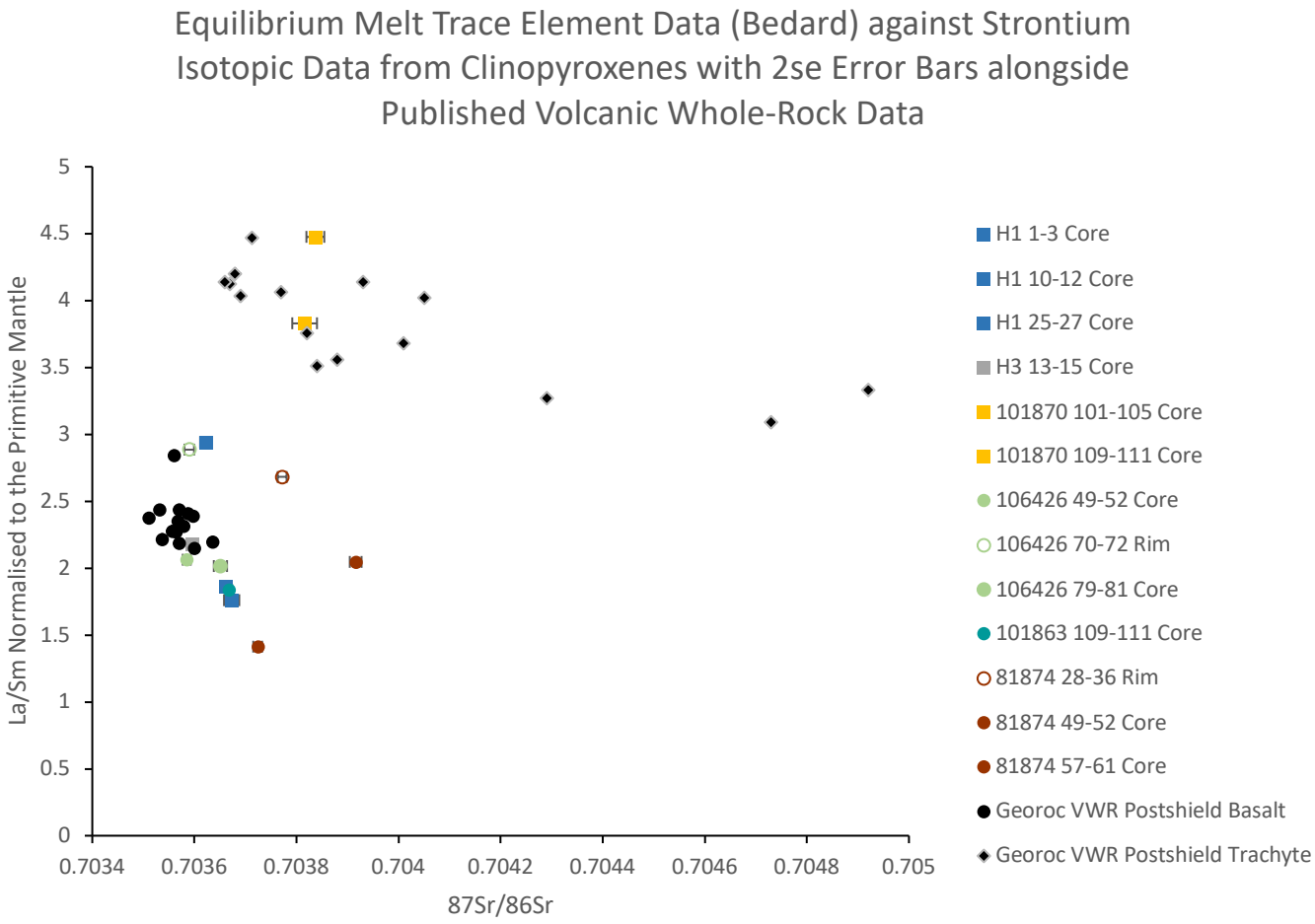
Equilibrium Melt Trace Element Data (Bedard) against Strontium Isotopic Data from Clinopyroxenes with 2se Error Bars alongside Published Volcanic Whole-Rock Data
La/Sm Normalised to the Primitive Mantle
87Sr/86Sr
0
0.5
1
1.5
2
2.5
3
3.5
4
4.5
5
0.7034
0.7036
0.7038
0.704
0.7042
0.7044
0.7046
0.7048
0.705
H1 1-3 Core
H1 10-12 Core
H1 25-27 Core
H3 13-15 Core
101870 101-105 Core
101870 109-111 Core
106426 49-52 Core
106426 70-72 Rim
106426 79-81 Core
101863 109-111 Core
81874 28-36 Rim
81874 49-52 Core
81874 57-61 Core
Georoc VWR Postshield Basalt
Georoc VWR Postshield Trachyte

b)

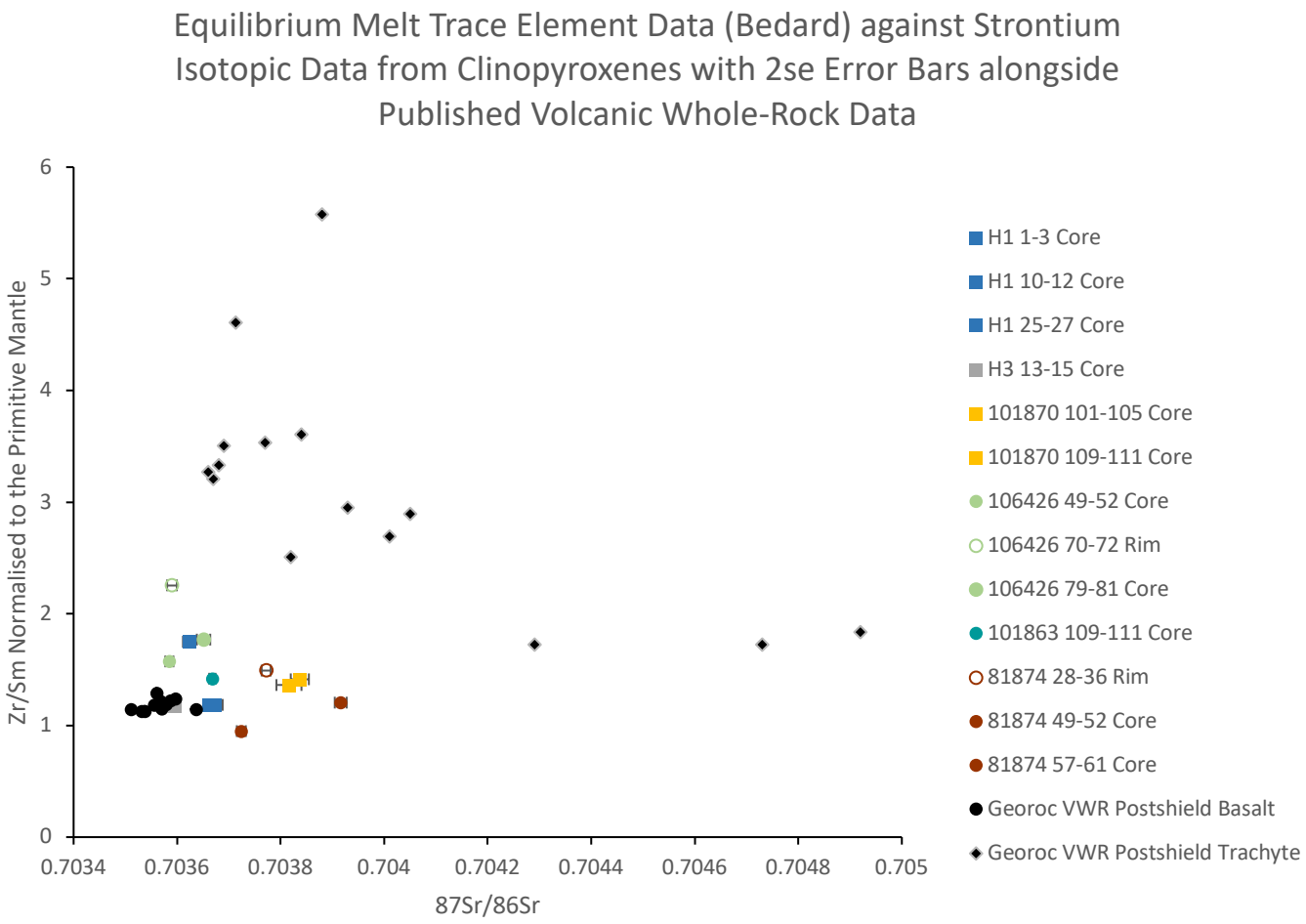

c)

Figure 50: Plots of trace element concentration ratios normalised to the primitive mantle for equilibrium melt compositions calculated from clinopyroxene data against $^{87}Sr/^{86}Sr$ isotopic data, alongside published volcanic whole rock (VWR) data for post-shield basalts (black circles) and post-shield trachytes (black diamonds) downloaded from the GEOROC database (see full references from page 21). Trace element data from the data collected in this study and GEOROC was normalised to the primitive mantle using primitive mantle values given by McDonough and Sun (1995). Equilibrium melt compositions were calculated using partition coefficients calculated using Bédard (2014). Square symbols denote wehrlitic samples, and circular symbols denote basaltic samples. Full squares/circles denote crystal cores, whereas hollow squares/circles represent crystal rims. The blue line plots the modelled path of fractional crystallisation from a basaltic melt. Error bars on $^{87}Sr/^{86}Sr$ isotopic data represent the internal precision for each data point (2se). Plot a) shows the Ce/Y ratio normalised to

the primitive mantle against $^{87}Sr/^{86}Sr$. Plot b) shows the La/Sm ratio normalised to the primitive mantle against $^{87}Sr/^{86}Sr$. Plot c) shows the Zr/Sm ratio normalised to the primitive mantle $^{87}Sr/^{86}Sr$.

5. Discussion

5.1 Petrogenetic Origin of the Hualalai Cumulates: Do Samples Represent Plume-Source Ocean Island Basalt (OIB) Material or Original Pacific Oceanic Crust (Mid-Ocean Ridge Basalt, MORB) Beneath Hawaii.

Previous studies have reported that xenoliths found at Hualalai have a range of origins. Xenolith samples have been found that relate to the shield and post-shield stages of Hualalai volcanism, with some rarer samples originating from the original Pacific lower oceanic crust beneath Hawaii (Clague, 1987; Gao *et al.*, 2016). To determine the heterogeneity of magma storage and mantle source regions associated with the Hualalai volcanic system, it must first be determined which of the Hualalai samples are appropriate for further consideration (i.e., which are actually related to the Hawaiian plume).

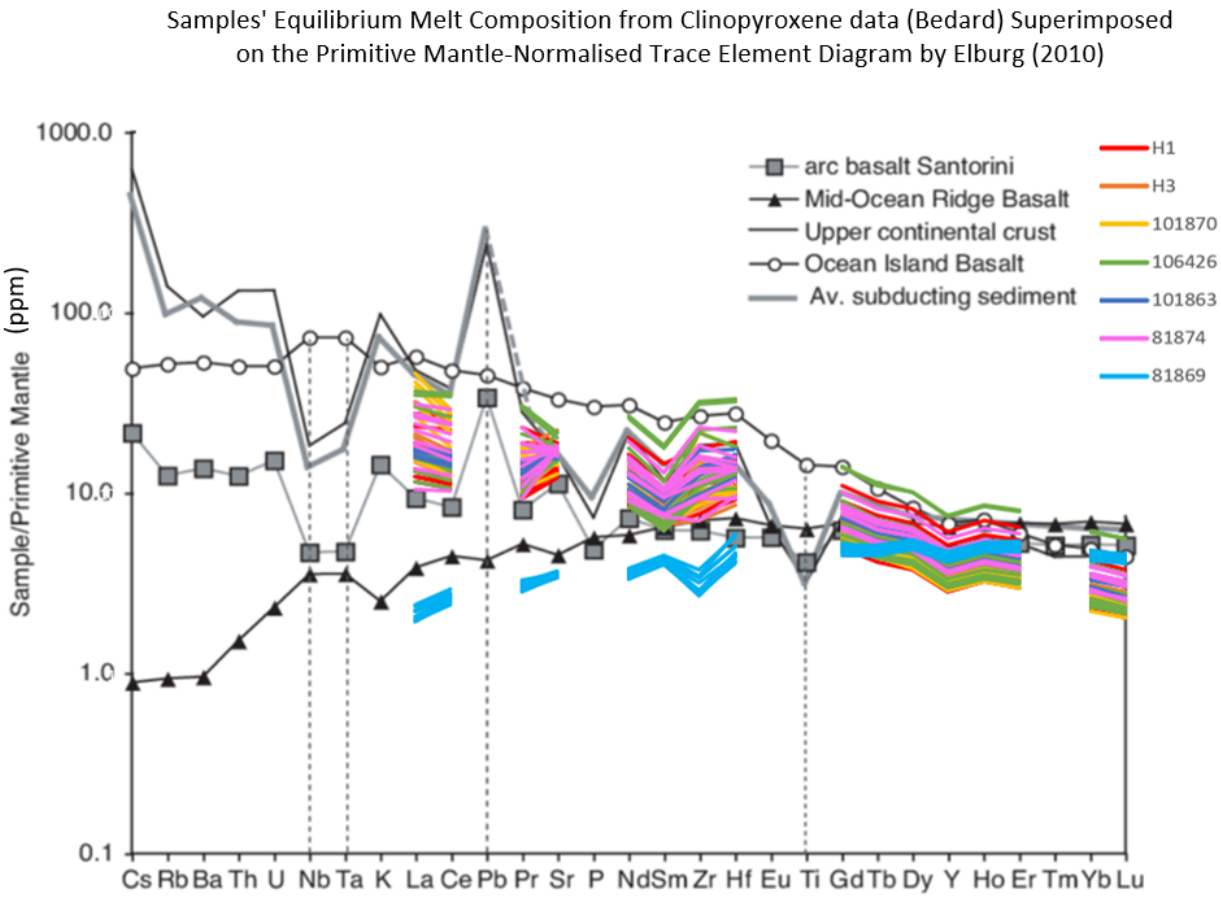

Figure 51: Primitive mantle-normalised trace element concentrations of samples H1 (red), H3 (orange), 101870 (yellow), 106426 (green), 101863 (dark blue), 81874 (pink) and 81869 (light blue) superimposed on the primitive mantle-normalised trace element concentration diagram from Elburg (2010) showing the trend of mid-ocean ridge basalt (triangles) and ocean island basalt (circles) (from Sun and McDonough (1989)), upper continental crust (black line) (from Rudnick and Gao (2003)), global average subducted material (grey line) (from Plank and Langmuir (1998)) and Santorini arc basalt (squares) (from Elburg & Smet (unpublished data)). Trace element concentrations for samples H1, H3, 101870, 106426, 101863, 81874 and 81869 were normalised to the primitive mantle using primitive mantle values given by McDonough and Sun (1995). The gradient and magnitude of sample 81869 best fits the trend for mid-ocean ridge basalt, and trace element data from samples H1, H3, 101870, 106426, 101863 and 81874 best fit the trend for ocean island basalts.

The gradient and magnitude of data plotted on primitive mantle-normalised diagrams of the trace element concentrations of parental melts calculated from clinopyroxene data for

samples H1, H3, 101870, 106426, 101863 and 81874 (see figs. 42 b), 43 b), 44 b), 45 b), 46 b) and 47 b)) produce a trend which coincides with what is expected from Ocean Island Basalt (OIB) material (see fig. 51). La/Sm equilibrium melt ratios (normalised to the primitive mantle (McDonough and Sun, 1995)), calculated from the clinopyroxene data collected in this study (Bédard, 2014), typically lie between 1.41 and 3.84 (with some higher values up to 6.12 in sample 101870), similar to the range of compositions observed in Hawaian basalts, 1.79 to 3.17 (from post-shield basaltic whole rock data downloaded from the GEOROC database (see full references from page 24)), but above those typically found in MORBs (La/Sm < 1 for N-MORB (Arevalo and McDonough, 2009)). Most samples therefore do appear to represent OIB material, and so are derived from the Hawaiian mantle plume.

Sample 81869, however, is an exception to this. Figure 48 b) shows that sample 81869 is depleted in trace elements, most markedly in light trace elements. La/Sm equilibrium melt ratios (normalised to the primitive mantle (McDonough and Sun, 1995)) for sample 81869, calculated from the clinopyroxene data (Bédard, 2014), lie between 0.46 and 0.57, which is distinct from the range of compositions observed in Hawaiian basalts, but fits within the La/Sm < 1 range for N-MORB (Arevalo and McDonough, 2009). Figure 48 b) also shows that sample 81869 mostly plots below the fields for basalt and trachyte from published post-shield volcanic whole rock lava data from GEOROC. Other graphs of trace element data, including figure 49, also clearly demonstrate the trace element depletion of sample 81869 relative to the other samples. This depleted trace element signature is typical of MORB, strongly suggesting that sample 81869 is a xenolith from the original oceanic crust beneath Hawaii.

The K_2O wt% values of plagioclase crystals in sample 81869 (see fig. 23) are also lower than those of other samples, consistent with the low potassium composition of MORB samples relative to the higher potassium composition expected of OIB samples (see fig. 51)(Elburg, 2010).

At this time, there is no trace element data for two of the samples studies, samples 81862 and H7, as a result, the origin of these samples is still uncertain. Studies have shown, however, that wehrlites are rare for MORB systems (Grove et al., 1992). The typical order of crystallisation revealed from Mid-ocean ridge (MOR) system drill cores is olivine-plagioclase-clinopyroxene, so MOR settings are commonly dominated by troctolites and gabbros, but

wehrlites are rare (Grove et al., 1992). Wehrlites are a common feature of many OIB systems, however, as in these settings plagioclase has a lower stability relative to clinopyroxene due to higher pressures and higher water content during magma storage (Bohrson and Clague, 1988). It has been therefore assumed that sample H7, a wehrlitic sample, is most likely of an OIB origin and related to the Hawaiian mantle plume, rather than the original Pacific crust. Sample 81862 is a dunite; as the TiO2 (wt%) values of this sample fits the array of other OIB samples like 101870 and H7 (see fig. 22), it has been assumed that it is also Hawaiian in nature. More work on samples H7 and 81862 would be required to assess their chemical heterogeneity in future.

5.2 Generation of intra- and inter-sample heterogeneity: what is the cause of chemical variability within and between samples.

5.2.1. The role of fractional crystallisation: do the xenoliths record primary mantle-related signatures?

Compositional element maps indicate that the xenoliths preserve a range of compositions, from variability between samples and variability within samples, both on the sample scale (like the compositional divide seen in sample 106426 (see fig. 18)) and on a crystal scale (like the compositional zoning of core-rim trends, e.g., sample H1 core 1-3 to rims 4-6 and 7-9 (see fig. 13)).

During crystallisation, it is expected that crystal phases precipitate before settling into cumulate piles due to their increased density relative to the remaining magma. The composition of the crystals forming cumulate piles would be expected to follow a simple model of fractional crystallisation. As a result, the simplest explanation for the formation of cumulate xenoliths is crystallisation from a mantle-derived magma that has undergone variable amounts of fractional crystallisation. However, various other processes can influence the composition of magmatic cumulates, producing non-primary signatures, including reactive porous flow and post-formation diffusive exchange. The possible influence of these factors on the Hualalai xenolith sample compositions must be evaluated before the results can be interpreted in terms of primary mantle signatures.

The magnitude of the modelled path of fractional crystallisation of a basaltic melt in figure 22 does not perfectly match the data array, with the model sitting above the data array. This, however, does not reduce the capacity of this model to be used to assess the role of fractional crystallisation in the chemical variability of the samples in this study. The gradient of the model's slope is more interesting than its absolute position, as the gradient of the model represents the path of fractional crystallisation which can be compared to the slopes of core-rim trends and array trends to see how much these trends can be accounted for by fractional crystallisation. Any difference between the slopes of these trends and the slope of the model indicates a mechanism other than fractional crystallisation of a basaltic melt at work. Figures 22, 24 and 25 show that, in general, the slopes of core-rim trends and sample array trends appear parallel to the model's gradient, so it can be concluded that much of the chemical variability seen in major and trace elements can be explained by fractional crystallisation.

There are a few possible exceptions to this, however:

Both the trend of the array and core-rim trends for sample 81874 do not fit that of the modelled slope in figure 22, being near vertical. In figure 22, the Mg# of 81874 barely changes, whilst TiO_2 increases dramatically. Usually, even assuming Ti is fully incompatible, Ti concentration would only be expected to increase this much with significant crystallisation of the magma, which would usually be accompanied with a decrease in Mg#. One possible explanation for this pattern could be diffusion and buffering between primitive crystals and more evolved melts percolating through the crystal framework.

The element map of 81874 (see fig. 20) shows that this sample is olivine rich. Primitive olivine crystals could have been surrounded by an evolved melt percolating through the crystal framework, causing the high Mg olivine crystals and low Mg evolved melt to try to equilibrate. Due to the high olivine crystal content of this sample relative to primitive melt (implied by the small proportion of plagioclase and clinopyroxene crystals in this sample relative to olivine crystals) the crystals would have a high buffering power. The evolving melt would have increased Ti concentration (and concentration of other incompatible elements), but due to buffering of the olivine crystals, olivine crystals exchanging Mg would prevent Mg decreasing in the evolving melt. As a result, Mg# remains consistently high in the melt (and therefore in the resultant clinopyroxene crystals) due to equilibration with the olivine

crystals through olivine buffering and diffusion, whilst TiO_2 increased due to the evolution of the melt (Lissenberg and Dick, 2008). Major elements like Mg and Fe are sensitive to buffering as they are very mobile, so diffusion of Mg can occur on much shorter timescales than trace elements (Costa et al., 2020). Trace elements are far less mobile, so this mechanism is unlikely to have affected the signatures of the trace element or isotopic data; the signatures of the trace and isotopic data for sample 81874 can still be expected to be primary. This is supported by the trace element trend of sample 81874 following the trend of the model of fractional crystallisation in figures 24 and 25.

Sample 106426 also invites further consideration as the major element map (figure 18) shows a sharp compositional divide between the top and bottom of the sample. Though major and trace element signatures do not indicate a deviation from the modelled path of fractional crystallisation across the compositional divide (suggesting a common parental melt between the two regions), Sr isotopic values of locations sampled in the two regions are distinct. This cannot be explained by fractional crystallisation.

Another sample which does not fit the trend of the modelled path of fractional crystallisation is 101870. The sample array and core-rim trends of sample 101870 are markedly steeper than the gradient of the model of the path of fractional crystallisation in figures 24 and 25, with most sampled data points for sample 101870 also lying at higher La/Sm and Ce/Y values than the bulk of data points from other samples, which lie around the modelled line.

Figures 24 and 25 also reveal that the core-rim trend for location 1-3 (core) to location 4-6 and 7-9 (rims) in sample H1 is too steep to be explained by fractional crystallisation. This trend is also in the opposite direction to the other core-rim trends for H1 and other samples, with the core (1-3) having a higher Ce and La concentration than the associated rims (4-6 and 7-9).

In conclusion, apart from these exceptions, most of the variability in the chemical composition of these samples can be explained by fractional crystallisation from basaltic magmas.

Therefore, aside from exceptions noted above, core-rim trends and sample array trends are mostly explained by fractional crystallisation from the same parent melt. As associated core

and rims are from the same parents melt (apart from H1 1-3), this suggests that the core-rim pattern is a primary signature, not formed by alteration, diffusion or melt-mush reactions. This is not always observed in other volcanic locations. Work on MORB and Galapagos samples found that rim compositions are often offset from core compositions (with respect to trace elements) due to mush processing (e.g., reactive flow)(Lissenberg *et al.*, 2013; Lissenberg and MacLeod, 2016; Gleeson et al., 2020).

5.2.2. Possible Connection to the Hualalai Trachytes

Despite the chemical composition of most sampled locations resembling that of erupted basaltic melts from Hualalai, some cumulates, including sample 101870, have the high Ce/Y and La/Sm values that fit published Hualalai trachytic lava data and the high Sr isotope values that are also characteristic of these trachytes (see fig. 50). This section aims to explore whether these cumulates are produced by the same processes that lead to trachyte formation (rather than basalt formation), or whether this sample could form from a mixture of basaltic and trachytic melts in the subvolcanic system.

Figure 49 c) is expected to be the most accurate differentiator of trachytic and basaltic melt. Figure 37 shows the trace element concentrations of basaltic and trachytic samples from published post-shield lava data, as found on GEOROC. The difference in slope from Zr to Sm between trachytes and basalts is markedly more significant than the differences in slope from Ce to Y and La to Sm between trachytes and basalts. From Zr to Sm, trachytic samples show a large decrease in concentration, which is not present in the basaltic samples. This ratio, therefore, should be a clear differentiator of the two groups. Figure 49 c) shows that the sampled data points of sample 101870 remains clearly distinct from the trachytic array; the absolute Zr concentrations for sample 101870 are far lower than those of trachytes, and only two sampled locations appear to reach trachytic Zr/Sm values, with one of those being only comparable to the lowest recorded Zr/Sm values for trachytes. Some of the data points of 101870 do lie clearly within the basaltic array, however, the tendency of some points to consistently frequent geochemical regions between both compositions in figure 49 do indicate that these crystals cannot have grown from melts similar to those erupted as post-shield basalts. It is unlikely, however, that there is a strong relationship between sample

101870 and the trachytic magmas due to the low concentration of Ce or La, which is inconsistent with crystallisation from these more evolved melts.

Moreover, the primitive mantle-normalised trace element concentration diagram, figure 44 b), showing the trace element concentrations of the parental melt for sample 101870, does not support a trachytic origin. The absolute concentrations of trace elements in this sample match that of the post-shield basaltic field far better than that of the post-shield trachytic field. The data for 101870 also lacks the sharp Sr anomaly typical of trachytic lavas. The steeper gradient of the trace element trends, shown in figure 49 a) and 49 b) by the higher Ce/Y and La/Sm values of samples 101870 relative to other samples, is not seen in the other samples and does not fit the basaltic trend. In this way, 101870 looks neither trachytic nor entirely basaltic in origin.

Finally, the Mg# values of sampled clinopyroxenes in sample 101870 are very high (see fig. 22). As seen in figure 7, trachytes are produced from evolved melts and have a characteristically low Mg#. The Mg# of sample 101870 is therefore inconsistent with crystallisation from a trachytic melt.

As such, the conclusions regarding the nature of 101870 remain inconclusive. Trace element ratios of sample 101870 indicate that its origin cannot be the same as that of the published post-shield basaltic lavas, however it appears that the anomalous trends of sample 101870 cannot be explained by a relationship with trachytic melts; as such, the signature of sample 101870 can neither have been produced by the same processes that lead to trachyte formation, nor formed from a mixture of basaltic and trachytic melts. It may be prudent to not consider this sample when assessing whether the heterogeneity of the cumulate samples in this study is greater than that of published basaltic data.

5.2.3. Mechanisms for Generating Intra-Sample Trace Element and Isotopic Heterogeneity: Diffusive Exchange and Melt-Mush Reaction

The trend of sample 101870 does not fit the trend of the modelled path of fractional crystallisation from a basaltic melt (see figs. 24 and 25), indicating that a mechanism other than fractional crystallisation must be invoked to explain the chemical composition of this sample. Different sampled locations of 101870 in figure 44 b) have trace element

concentration lines with different gradients (this is also shown by the vast range of Ce/Y values for sample 101870 in figure 49 a)). This range of variations in slope of trace element concentrations seen in figure 44 b) cannot be explained by fractional crystallisation alone.

Figure 16 shows that the borders between olivine and clinopyroxene crystals in sample 101870 do not form clear crystalline faces, rather undulating boundaries which could be dissolution fronts. This sample may have originated as an olivine framework dunite, through which percolated a melt, causing the dissolution of olivine crystals and the precipitation of clinopyroxene crystals. As a result, the possibility that the clinopyroxene melt may have been of an entirely different composition to that of the original olivine forming melt was considered. For reasons outlined above, 101870 could not represent a basaltic framework infiltrated by a trachytic melt, with interaction between these two melts creating the anomalous chemical signature of the clinopyroxene crystals. Two possible explanations for the anomalous chemical signature of sample 101870 include:

(i) A process operating within the crystal mush may have generated the anomalously trace element signatures seen in sample 101870.

(ii) The clinopyroxenes from this sample crystallised from mantle-derived melts that are unlike any previously measured from erupted basaltic lavas on Hualalai.

The petrographic evidence of reactive porous flow (specifically olivine dissolution and reaction in an initially olivine-rich mush system) could support hypothesis (i), as studies on other regions globally have hypothesised that this process can drive trace element ratio enrichment (Gleeson et al., 2020). Olivine dissolution and clinopyroxene precipitation through reactive porous flow could also fractionate trace elements, producing the steep gradients observed in the light REEs in fig. 44 b) (Gleeson et al., 2020).

If this suggestion is correct, this would mean that the trace element signature of sample 101870 is almost certainly not primary. Fractionation of Sr isotopes, however, is very difficult to achieve within a magmatic system, and the process of reactive porous flow which has affected the trace element signature would not be expected to affect the Sr isotope signature; this Sr isotope signature could remain primary and track primary heterogeneity.

As discussed above, however, 101870 Sr isotopic data could be different from other samples due to originating from a different melt composition (a non-basaltic melt).

5.2.4. Mechanisms for Generating Intra-Sample Trace Element and Isotopic Heterogeneity: Primary Melt Heterogeneity

Most major and trace element data collected can be explained by fractional crystallisation or other processes like reactive flow, but there are samples that display some variability in their trace element and isotopic signatures that cannot be generated by magmatic processes alone. Most notably among these is sample H1. Figures 24 and 25 reveal that the core-rim trend for location 1-3 (core) to location 4-6 and 7-9 (rims) in sample H1 is too steep to be explained by fractional crystallisation. This trend is also in the opposite direction to the other core-rim trends for H1 and other samples, with the core (1-3) having a higher Ce and La concentration than the associated rims (4-6 and 7-9). This can be explained by the core and rims originating from different parent melts. The primitive mantle-normalised trace element concentration diagram, figure 42 b), shows that trace element concentrations for H1 location 1-3 has a much steeper gradient than that of other sampled locations, and crosses the lines of other sampled locations. This cross-cutting suggests that H1 location 1-3 originates from a different parental melt composition, rather than the rim locations. Figure 50 reveals that H1 location 1-3 not only has significantly different element ratios to other H1 locations, but has a significantly different Sr isotope value. This isotopic difference between site 1-3 and other clinopyroxene sites in H1 also supports that core 1-3 and the other sampled clinopyroxene crystals have crystallised from two separate mantle melts, revealing multiple melt histories within this one sample.

Looking at the petrography of core 1-3 on the H1 element map (see fig. 13), the appearance of core 1-3 is distinct from any other core in the sample. Major element data shows that the Cr concentration is particularly high and Ti concentration is low for location 1-3 relative to the other sampled cores and rims of the sample. This major element data shows that this core is more primitive than other clinopyroxene crystals, and supports the suggestion from trace element data that this crystal core also has a different origin to other clinopyroxene crystals.

In conclusion, core 1-3 is likely to originate from a different parental melt from the surrounding rim and the other clinopyroxenes in this sample. Furthermore, as crystal scale analysis has revealed a different parent melt for H1 core 1-3, it is clear that this technique can reveal preserved crystal scale heterogeneity within samples.

The variation in $^{87}Sr/^{86}Sr$ isotopic values across the compositional divide in sample 106426 may also indicate the presence of different parental melts within that sample. The sharpness of the compositional divide in sample 106426 indicates that this compositional transition was not gradual and probably did not occur from the continual crystallisation of a single melt; these two compositional domains formed from the crystallisation of two different melts. The bottom of the sample appears to be formed from a more primitive, higher Mg# magma than the upper portion (fig. 22), which formed from a more evolved, lower Mg# melt, with the more evolved melt likely crystallising later. In figures 24 and 25, it appears that the sampled locations 79-81 and 82-84 from the upper domain (further up the x axes) remain on trend with the locations sampled in the lower domain (further down the x axes). Trace element contents in La/Sm vs La and Ce/Y vs Ce space, therefore, appear to lie along lines predicted by the fractional crystallisation model. Furthermore, the trace element concentration lines for locations 79-81 and 82-84 in sample 106426 on figure 45 b) appear parallel to the lines for the locations in the lower compositional domain. This consistency between all sampled locations across the compositional divide initially suggests that the upper or lower chemical domains did not deviate from the modelled path of fractional crystallisation, and that the melts forming both regions in sample 106426 formed from a common parent melt which underwent different amounts of fractional crystallisation before entering the 106426 system. However, the Sr isotopic data indicates that the magmas forming the two compositionally distinct regions may be unrelated (i.e., not from the same parent melt, and not simply related to one another by different degrees of fractional crystallisation). The $^{87}Sr/^{86}Sr$ isotopic value of sample 106426 location 79-81 (from the upper compositional region, see fig. 18) is consistently higher than the Sr isotopic values of the locations sampled from the lower compositional domain (see fig. 50). As fractional crystallisation cannot alter the Sr isotopic value, this indicates that two isotopically distinct parental magmas were potentially involved in the crystallisation of the two compositional

domains. The fact that there is little within the major and trace element data to indicate that different magmas generated the different compositional regions (discussed above) indicates that the compositional difference between the two parent melts is subtle. One possible explanation is that the magmas forming the two compositional domains became isotopically distinct from the mixing of a second melt (with different Sr values) with the initial parental melt, enough to cause a small isotopic shift, but not so much as to influence major or trace element signatures significantly.

5.3 Do Xenoliths Record More Heterogeneity than Erupted Basalts?

5.3.1. Isotopic Heterogeneity

Fractional crystallisation, which can explain much of the trace element chemical variability in samples H1 (apart from core 1-3), H3, 106426, 101863 and 81874, does not influence isotopic composition, so it can be assumed that any heterogeneity revealed in the $^{87}Sr/^{86}Sr$ data of these OIB samples from basaltic melts is primary (originating from the mantle), and not produced from secondary processes in the crust.

Figure 50 shows that the samples in this study (those considered to be OIB and derived from basaltic melts) have $^{87}Sr/^{86}Sr$ values which do not extend below published basaltic post-shield values. The lowest $^{87}Sr/^{86}Sr$ value collected in this study is 0.703585 (from sample 106426 location 49-52, see fig. 18), but the lowest published value is 0.70353. The $^{87}Sr/^{86}Sr$ isotope data of the samples, however, does extend well above the values of the published data. The highest $^{87}Sr/^{86}Sr$ value collected in this study is 0.703916 (from sample 81874 location 57-61, see fig. 20), whereas the highest value from the published basaltic data is 0.70364. The range of the data collected in this study is therefore 0.000331 and the range of the published data is 0.00011, so the data from this study also has a wider range of $^{87}Sr/^{86}Sr$ isotopic values than that of the published data.

The data collected in this study reveals a greater range of $^{87}Sr/^{86}Sr$ isotopic values than the published data for post-shield basaltic lavas, and so, following the assumption that this must be a primary signature, this finding supports the hypothesis that lower crustal cumulates

from Hualalai reveal greater chemical heterogeneity than that found in erupted Hualalai lavas.

This greater intra-sample $^{87}Sr/^{86}Sr$ heterogeneity could have two possible sources:

(i) It could reflect the true/greater heterogeneity of the mantle source beneath Hualalai.

The mantle source of the gabbroic and wehrlitic cumulate samples may be more chemically heterogeneous than what has been revealed from erupted post-shield basaltic lavas.

(ii) It could reflect a temporal change in the composition of the mantle source beneath Hualalai.

The erupted basalts sampled the mantle source during the post-shield stage only. The chemical variability of the samples analysed in this study, therefore, could reflect the changing chemical signatures of the mantle source, sampled over a longer time-period than the post-shield basaltic lavas. Studies have shown that isotopic signatures change between the shield and post-shield stages in some regions of Hawaii (Hanano *et al.*, 2010). If the samples analysed in this study picked up signatures from either side of an isotopic transition, then it may look like they are revealing greater chemical heterogeneity. This could explain why the variability seen between samples is generally greater than the variability within samples. In this scenario, the variation in composition between samples would result from differently aged xenoliths recording the changing isotopic melt composition under Hualalai over time. Conversely, the differences within samples would indicate the range of compositions within the melt at each given point in time.

As discussed above, sample H1 preserves $^{87}Sr/^{86}Sr$ heterogeneity from core 1-3, which originates from a different parental melt to the other clinopyroxenes. It is unlikely for one sample to be active over a long enough time-period to sample the chemical signatures on either side of a shield to post-shield transition. This implies that inter-sample heterogeneity at least reflects true source heterogeneity.

5.3.2. Trace Element Heterogeneity

All points sampled from of cumulates 81874, 101863 and H1 (ignoring location 1-3 due to it originating from a different parental melt) extend the isotopic heterogeneity above that of the published basaltic post-shield data, with locations from sample 81874 extending to the most radiogenic values (fig. 50). These plots, however, show that there is no correlation between the samples and sampled locations therein that extend the $^{87}Sr/^{86}Sr$ heterogeneity and which extend the trace element heterogeneity.

For example, 81874 locations 57-61, 28-36 and 49-54 were those chosen for $^{87}Sr/^{86}Sr$ isotopic analysis. Despite extending the range of $^{87}Sr/^{86}Sr$ above that of published values for post-shield basaltic lavas, figure 47 b) shows that locations 57-61 and 28-36 sit comfortably within the published basaltic array for trace element concentrations. Location 49-54 does extend to REE concentrations below than of the published basaltic array for some lighter REEs, but so do 106426 location 49-52 (fig. 45 b)) and H3 location 13-15 which sit within the published basaltic array for $^{87}Sr/^{86}Sr$ data. Another example: H1 locations 25-27 and 10-12 and 101863 location 109-111 all have $^{87}Sr/^{86}Sr$ values within uncertainty of eachother (fig. 50), however the H1 locations extent to REE concentrations below that of the published basaltic array, whereas the 101863 location remains well within the basaltic array.

The $^{87}Sr/^{86}Sr$ variability is likely to represent the heterogeneity in the mantle source beneath Hualalai, whether true or temporal. This isotopic heterogeneity, however, does not correlate to the trace element data of OIB samples which appear likely to show primary trace element signatures. This lack of correlation could be explained by:

(i) The $^{87}Sr/^{86}Sr$ heterogeneity being a subtle heterogeneity that is not detectable in the trace element signatures.

(ii) Trace element signatures may have been affected by an undetected mechanism which resulted in non-primary trace element signatures, but which did not affect $^{87}Sr/^{86}Sr$ isotopes.

$^{87}Sr/^{86}Sr$ isotopes are less likely than trace elements to undergo fractionation, so $^{87}Sr/^{86}Sr$ signatures are likely to remain primary. From sample 101870, some mechanisms have occurred in at least this sample which affect the trace element signature. Perhaps other mechanisms, or the same mechanism which affected 101870, has been at work more subtly

in the other samples to produce secondary trace element signatures, contrary to what was initially believed. As previously discussed, however, there is no indication in the trace element data that most of the signatures for samples H1, H3, 106426, 101863 and 81874 are non-primary.

6. Conclusion

Lower crustal cumulate samples of Hawaiian plume origin from Hualalai record primary sample- and crystal-scale compositional variation. These samples record greater trace element and isotopic heterogeneity than that which has been found from the analysis of corresponding published basaltic lavas (from published basaltic post-shield whole rock data downloaded from the GEOROC database (see full references from page 24). In line with Sarah Lambart et al.'s (2019) hypothesis for cumulates from MOR settings, it is hypothesised that this greater heterogeneity is expressed in lower crustal Hawaiian cumulates because the melts from which they formed experience less magma mixing than corresponding erupted basaltic lavas, and, therefore, less homogenisation of trace element and isotopic signatures. This suggests that homogenisation from magma mixing in the crust occurs at both MOR and OIB settings – at least under Hualalai, Hawaii. As a result, the data collected in this study suggests that previous studies on the Hawaiian mantle plume beneath Hualalai, conducted using basaltic lavas, may have underestimated its true heterogeneity. These findings, however, show that sampled regions with the most heterogeneous isotopic values do not correspond to regions with the most heterogeneous trace element values, suggesting that the isotopic $^{87}Sr/^{86}Sr$ heterogeneity is a subtle heterogeneity that is not detectable in the trace element signatures. Future work could explore the neodymium isotopic variations in these samples to assess whether these support the strontium isotopic data. Similar work could also be done on cumulates from other Hawaiian volcanoes, or other plume-generated volcanoes globally to explore whether cumulates in all plume settings reveal greater heterogeneity than corresponding lavas.

7. References

A. E. Ringwood (1962) 'A model for the upper mantle', *Journal of Geophysical Research*, 67(2), pp. 857–867.

Abouchami, W. *et al.* (2005) 'Lead isotopes reveal bilateral asymmetry and vertical continuity in the Hawaiian mantle plume', *Nature*, 434(7035), pp. 851–856. doi: 10.1038/nature03402.

Allegre, C. J. *et al.* (1980) 'Isotopic and chemical effects produced in a continuously differentiating convecting Earth mantle', *Philosophical Transactions of the Royal Society of London. Series A, Mathematical and Physical Sciences*, 297(1431), pp. 447–477. doi: 10.1098/rsta.1980.0225.

Anonymous (1980) 'Basaltic volcanism study project: Basaltic volcanism on the terrestrial planets', pp. 161–192.

Arevalo, R. J. and McDonough, W. F. (2009) 'Chemical variations and regional diversity observed in MORB', *Chemical Geology*, 271, pp. 70–85. doi: 10.1016/j.chemgeo.2009.12.013.

Batiza, R. (1984) 'Inverse relationship between Sr isotope diversity and rate of oceanic volcanism has implications for mantle heterogeneity', *Nature*, 309(5967), pp. 440–441. doi: 10.1038/309440a0.

Bédard, J. H. (2001) 'Parental magmas of the nain plutonic suite anorthosites and mafic cumulates: A trace element modelling approach', *Contributions to Mineralogy and Petrology*, 141(6), pp. 747–771. doi: 10.1007/s004100100268.

Bédard, J. H. (2006) 'Trace element partitioning in plagioclase feldspar', *Geochimica et Cosmochimica Acta*, 70(14), pp. 3717–3742. doi: 10.1016/j.gca.2006.05.003.

Bédard, J. H. (2014) 'Parameterizations of calcic clinopyroxene - Melt trace element partition coefficients', *Geochemistry, Geophysics, Geosystems*, 15(2), pp. 303–336. doi: 10.1002/2013GC005112.

Bohrson, W. A. and Clague, D. A. (1988) 'Origin of ultramafic xenoliths containing exsolved pyroxenes from Hualalai Volcano, Hawaii', *Contributions to Mineralogy and Petrology*, 100(2), pp. 139–155. doi: 10.1007/BF00373581.

Brandon, A. D. and Walker, R. J. (2005) 'The debate over core-mantle interaction', *Earth and Planetary Science Letters*, 232(3–4), pp. 211–225. doi: 10.1016/j.epsl.2005.01.034.

Burke, K., Steinberger, B., Torsvik, T. H. and Smethurst, M. A. (2008) 'Plume Generation Zones at the margins of Large Low Shear Velocity Provinces on the core-mantle boundary', *Earth and Planetary Science Letters*, 265(1–2), pp. 49–60. doi: 10.1016/j.epsl.2007.09.042.

Campbell, I. H. (2007) 'Testing the plume theory', *Chemical Geology*, 241(3–4), pp. 153–176. doi: 10.1016/j.chemgeo.2007.01.024.

Campbell, I. H. and Griffiths, R. W. (1990) 'Implications of mantle plume structure for the evolution of flood basalts', *Earth and Planetary Science Letters*, 99(1–2), pp. 79–93. doi: 10.1016/0012-821X(90)90072-6.

Campbell, I. H., Griffiths, R. W. and Hill, R. I. (1989) 'Melting in an Archaean mantle plume: Heads it's basalts, tails it's komatiites', *Nature*, 339(6227), pp. 697–699. doi: 10.1038/339697a0.

Campbell, J. F. and Erlandson, D. (1979) *OTEC-I anchor site survey*, *Haw Inst Geophys Report Hawaii*, 55p.

Cipriani, A., Brueckner, H. K., Bonatti, E. & Brunelli, D. (2004) Oceanic crust generated by elusive parents: Sr and Nd isotopes in basalt-peridotite pairs from the Mid-Atlantic Ridge, *Geology,* 32(8), pp. 657–660. doi: https://doi.org/10.1130/G20560.1

Chen, C. H., Presnall, D. C. and Stern, R. J. (1992) 'Petrogenesis of ultramafic xenoliths from the 1800 kaupulehu flow, hualalai volcano, Hawaii', *Journal of Petrology*, 33(1), pp. 163–202. doi: 10.1093/petrology/33.1.163.

Cherniak, D. J. (2003) 'REE diffusion in feldspar', *Chemical Geology*, 193(1–2), pp. 25–41. doi: 10.1016/S0009-2541(02)00246-2.

Clague, D. A. (1987) 'Hawaiian xenolith populations, magma supply rates, and development of magma chambers', *Bulletin of Volcanology*, 49(4), pp. 577–587. doi: 10.1007/BF01079963.

Clague, D. A. (1987) 'Hawaiian xenolith populations, magma supply rates, and development of magma chambers', *Bulletin of Volcanology*, 49, pp. 577–587. doi: 10.1007/BF01079963.

Clague, D. A. and Bohrson, W. A. (1991) 'Origin of xenoliths in the trachyte at Puu Waawaa,

Hualalai Volcano, Hawaii', *Contributions to Mineralogy and Petrology*, 108, pp. 439–452. doi: 10.1007/BF00303448.

Clague, D. A., Jackson, E. D. and Wright, T. L. (1980) 'Petrology of Hualalai Volcano, Hawaii: Implication for Mantle Composition', *Bull. Voleanol.,* 43(4), pp. 641–656. doi: 10.1007/BF02600363.

Clague, D. A. and Sherrod, D. R. (2014) 'Growth and Degradation of Hawaiian Volcanoes', *U.S. Geological Survey Professional Paper*, 1801, pp. 97–146.

Clague, D. and Dalrymple, G. B. (1987) 'The Hawaiian- Emperor volcanic chain. Part I. Geologic evolution.', *US Geological Survey Professional Paper*, pp. 5–54.

Costa, F., Shea, T. and Ubide, T. (2020) 'Diffusion chronometry and the timescales of magmatic processes', *Nature Reviews Earth & Environment*. Springer US, 1(April), pp. 201–214. Available at: http://dx.doi.org/10.1038/s43017-020-0038-x.

Cottaar, S. and Romanowicz, B. (2012) 'An unsually large ULVZ at the base of the mantle near Hawaii', *Earth and Planetary Science Letters*. Elsevier, 355–356, pp. 213–222. doi: 10.1016/j.epsl.2012.09.005.

Cousens, B. L., Clague, D. A. and Sharp, W. D. (2003) 'Chronology, chemistry, and origin of trachytes from Hualalai Volcano, Hawaii', *Geochemistry Geophysics Geosystems*, 4(9), pp. 1–27. doi: 10.1029/2003GC000560.

Davies, G. F. (1988) 'Role of the Lithosphere in Mantle Convection', *Journal of Geophysical Research*, 93(89), pp. 10,451-10,466.

Decker, R. (1987) 'Dynamics of Hawaiian volcanoes: an overview', *in Decker, R.W., Wright, T.L., and Stauffer, P.H., eds., Volcanism in Hawaii: U.S. Geological Survey Professional Paper 1350*, 2, pp. 997–1,018.

Dungan, M. A. and Rhodes, J. M. (1978) 'Contributions to Mineralogy and Residual Glasses and Melt Inclusions in Basalts From DSDP Legs 45 and 46 : Evidence for Magma Mixing Petrography of Aphyric Basalts', *Elements*, 431, pp. 417–431.

Eisele, J., Sharma, M., Galer, S., Blichert-Toft, J., Devey, C. W. and Hofmann, A. W. (2002) 'The role of sediment recycling in EM-1 inferred from Os, Pb, Hf, Nd, Sr isotope and trace element

systematics of the Pitcairn hotspot', *Earth and Planetary Science Letters*, 196(3–4), pp. 197–212. doi: 10.1016/S0012-821X(01)00601-X.

Elburg, M. A. (2010) 'Sources and processes in arc magmatism: The crucial role of water', *Geologica Belgica*, 13(3), pp. 119–134.

Farnetani, C. G. and Samuel, H. (2005) 'Beyond the thermal plume paradigm', *Geophysical Research Letters*, 32(7), pp. 1–4. doi: 10.1029/2005GL022360.

French, S. W. and Romanowicz, B. (2015) 'Broad plumes rooted at the base of the Earth's mantle beneath major hotspots', *Nature*, 525(7567), pp. 95–99. doi: 10.1038/nature14876.

Frey, F. A., Wise, W. S., Garcia, M. O., West, H., Kwon, S.-T. and Kennedy, A. (1990) 'Evolution and Mauna Kea Volcano, Hawaii: petrologic and geochemical constraints on postshield volcanism', *Journal of Geophysical Research*, 95(B2), pp. 1271–1300. doi: 10.1029/JB095iB02p01271.

Funkhouser, J. G., Barnes, L. and Naughton, J. J. (1968) 'The Determination of a Series of Ages of Hawaiian Volcanoes by the Potassium-Argon Method', *Pacific Science*, 22, pp. 369–372.

Gao, R., Lassiter, J. C., Barnes, J. D., Clague, D. and Bohrson, W. A. (2016) 'Geochemical investigation of Gabbroic Xenoliths from Hualalai Volcano: Implications for lower oceanic crust accretion and Hualalai Volcano magma storage system', *Earth and Planetary Science Letters*. Elsevier B.V., 442, pp. 162–172. doi: 10.1016/j.epsl.2016.02.043.

Garcia, M. O., Grooms, D. G. and Naughton, J. J. (1987) 'Petrology and geochronology of volcanic rocks from seamounts along and near the Hawaiian Ridge: Implications for propagation rate of the ridge', *Lithos*. Elsevier Science Publishers B.V., 20(4), pp. 323–336. doi: 10.1016/S0024-4937(87)80005-1.

Garnero, E. J. and McNamara, A. K. (2008) 'Structure and dynamics of earth's lower mantle', *Science*, 320(5876), pp. 626–628. doi: 10.1126/science.1148028.

Garnero, E. J., Mcnamara, A. K. and Shim, S. (2016) 'Continent-sized anomalous zones with low seismic velocity at the base of Earth's mantle', *Nature Publishing Group*. Nature Publishing Group, 9(July), pp. 481–489. doi: 10.1038/ngeo2733.

Giuliani, A., Jackson, M. G., Fitzpayne, A. and Dalton, H. (2020) 'Remnants of early Earth

differentiation in the deepest mantle-derived lavas', *Proceedings of the National Academy of Sciences of the United States of America*, 118(1), pp. 1–9. doi: 10.1073/pnas.2015211118.

Gleeson, M. L. M., Gibson, S. A. and Stock, M. J. (2020) 'Upper Mantle Mush Zones beneath Low Melt Flux Ocean Island Volcanoes: Insights from Isla Floreana, Galápagos', *Journal of Petrology*, 61(12), pp. 1–26. doi: 10.1093/petrology/egaa094.

Gleeson, M., Gibson, S., Stock, M. and EIMF (2022) 'Constraints on the behaviour and content of volatiles in Galapagos magmas from melt inclusions and nominally anhydrous minerals', *Geochimica et Cosmochimica Acta*, 319, pp. 168-190

Gleeson, M., Lissenberg, C. J. and Lecoeuche, C. (no date) 'Unpublished Data'.

Griffiths, R. W. and Campbell, I. H. (1990) 'Stirring and structure in mantle starting plumes', *Earth and Planetary Science Letters*, 99(1–2), pp. 66–78. doi: 10.1016/0012-821X(90)90071-5.

Grove, T. L., Kinzler, R. J. and Bryan, W. (1992) 'Fractionation of mid-ocean ridge basalt (MORB)', *Washington DC American Geophysical Union Geophysical Monograph Series*, 71, pp. 281–310.

Gualda, G. A. R., Ghiorso, M. S., Lemons, R. V. and Carley, T. L. (2012) 'Rhyolite-MELTS: A modified calibration of MELTS optimized for silica-rich, fluid-bearing magmatic systems', *Journal of Petrology*, 53(5), pp. 875–890. doi: 10.1093/petrology/egr080.

Guillou, H., Garcia, M. O. and Turpin, L. (1997) 'Unspiked K-Ar dating of young volcanic rocks from Loihi and Pitcairn hot spot seamounts', *Journal of Volcanology and Geothermal Research*, 78(3–4), pp. 239–249. doi: 10.1016/S0377-0273(97)00012-7.

Hamilton, E. I. (1965) 'Distribution of some trace elements and the isotopic composition of strontium in Hawaiian lavas', *NATURE*, 206, pp. 251–253. doi: 10.1038/206251a0.

Hanan, B. B. and Graham, D. W. (1996) 'Lead and helium isotope evidence from oceanic basalts for a common deep source of mantle plumes', *Science*, 272(5264), pp. 991–995. doi: 10.1126/science.272.5264.991.

Hanano, D., Weis, D., Scoates, J. S., Aciego, S. and DePaolo, D. J. (2010) 'Horizontal and vertical zoning of heterogeneities in the Hawaiian mantle plume from the geochemistry of

consecutive postshield volcano pairs: Kohala-Mahukona and Mauna Kea–Hualalai', *Geochemistry Geophysics Geosystems*, 11(1), pp. 1–22. doi: 10.1029/2009GC002782.

Harold T. Stearns (1946) 'Geology of the Hawaiian Islands.', *Division of Hydrography*, Bulletin 8, pp. 1–112.

Harpp, K. S. and Weis, D. (2020) 'Insights Into the Origins and Compositions of Mantle Plumes: A Comparison of Galápagos and Hawai'i', *Geochemistry, Geophysics, Geosystems*, 21(9). doi: 10.1029/2019GC008887.

Hart, S. R. (1988) 'Heterogeneous mantle domains: signatures, genesis and mixing chronologies', *Earth and Planetary Science Letters*, 90(3), pp. 273–296. doi: 10.1016/0012-821X(88)90131-8.

Hart, S. R., Hauri, E. H., Oschmann, L. A. and Whitehead, J. A. (1992) 'Mantle plumes and entrainment: Isotopic evidence', *Science*, 256(5056), pp. 517–520. doi: 10.1126/science.256.5056.517.

Harris, P. G. (1957). Zone refining and the origin of potassic bas- alts. Geochimica et Cosmochimica Acta 12, 195–208.

Hauri, E. H. (1996) 'Major-element variability in the Hawaiian mantle plume', *Nature*, 382(6590), pp. 415–419. doi: 10.1038/382415a0.

Hill, E., Blundy, J. D. and Wood, B. J. (2011) 'Clinopyroxene-melt trace element partitioning and the development of a predictive model for HFSE and Sc', *Contributions to Mineralogy and Petrology*, 161(3), pp. 423–438. doi: 10.1007/s00410-010-0540-0.

Hill, E., Blundy, J. D. and Wood, B. J. (2012) 'Erratum to: Clinopyroxene-melt trace element partitioning and the development of a predictive model for HFSE and Sc', *Contributions to Mineralogy and Petrology*, 163(3), pp. 563–565. doi: 10.1007/s00410-011-0716-2.

Hofmann, A. W. (1997) 'Mantle geochemistry: the message from oceanic volcanism', *Nature*, pp. 219–229. doi: 10.1038/385219a0.

Hofmann, A. W. and White, W. M. (1982) 'Mantle plumes from ancient oceanic crust', *Earth and Planetary Science Letters*, 57(2), pp. 421–436. doi: 10.1016/0012-821X(82)90161-3.

Horwitz, E. P., Chiarizia, R. and Dietz, M. (1992) 'A novel strontium-selective extraction

chromatographic resin', *Solvent Extraction and Ion Exchange*, 10(2), pp. 313–336.

Huang, S., Frey, F. A., Blichert-Toft, J., Fodor, R. V., Bauer, G. R. and Xu, G. (2005) 'Enriched components in the Hawaiian plume: Evidence from Kahoolawe volcano, Hawaii', *Geochemistry, Geophysics, Geosystems*, 6(11). doi: 10.1029/2005GC001012.

Huang, S. and Frey, F. A. (2005) 'Recycled oceanic crust in the Hawaiian plume: Evidence from temporal geochemical variations within the Koolau shield', *Contributions to Mineralogy and Petrology*, 149(5), pp. 556–575. doi: 10.1007/s00410-005-0664-9.

Ishii, M. and Tromp, J. (1999) 'Normal-Mode and Free-Air Gravity Constraints on Lateral Variations in Velocity and Density of Earth's Mantle', *Science*, 285(August), pp. 1231–1237.

Jackson, E. D., Shaw, H. R. and Bargar, K. E. (1975) 'Calculated Geochronology and Stress Field Orientations Along the Hawaiian Chain', *Earth and Planetary Science Letters*, 26, pp. 145–155.

Jackson, E. D., Clague, D. A., Engleman, E., Friesen, W. B. and Norton, D. (1981) 'Xenoliths in the alkalic basalt flows from Hualalai volcano, Hawaii', *U.S. Geological Survey Open-File Report*, (81–1031), pp. 1–32. Available at: http://pubs.usgs.gov/of/1981/1031/report.pdf.

Jackson, M. G., Becker, T. W. and Konter, J. G. (2018) 'Geochemistry and Distribution of Recycled Domains in the Mantle Inferred From Nd and Pb Isotopes in Oceanic Hot Spots: Implications for Storage in the Large Low Shear Wave Velocity Provinces', *Geochemistry, Geophysics, Geosystems*, 19(9), pp. 3496–3519. doi: 10.1029/2018GC007552.

Jochum, K. P., Enzweiler, J., Mertz-Kraus, R. and Wang, X. (2010) 'GGR Biennial Review: Reference Materials in Geoanalytical and Environmental Research - Review for 2008 and 2009', *Geostandards and Geoanalytical Research*, 34(4), pp. 353–385. doi: 10.1111/j.1751-908X.2010.00931.x.

Jochum, K. P., Weis, U., Stoll, B., Kuzmin, D., Yang, Q., Raczek, I., Jacob, D. E., Stracke, A., Birbaum, K., Frick, D. A., Günther, D., and Enzweiler, J. (2011) 'Determination of reference values for NIST SRM 610-617 glasses following ISO guidelines', *Geostandards and Geoanalytical Research*, 35(4), pp. 397–429. doi: 10.1111/j.1751-908X.2011.00120.x.

Keller, R. A., Duncan, R. A. and Fisk, M. R. (1995) 'Geochemistry and 40Ar/39Ar Geochronology of Basalts from ODP Leg 145 (North Pacific Transect)', *Proceedings of the*

Ocean Drilling Program, 145 Scientific Results, 145. doi: 10.2973/odp.proc.sr.145.131.1995.

Koppers, A. A. P., Becker, T., Jackson, M. G., Konrad, K., Müller, D., Romanowicz, B., Steinberger, B. and Whittaker, J. M.(2021) 'Mantle plumes and their role in Earth processes', *Nature Reviews Earth and Environment*. Springer US, 2(6), pp. 382–401. doi: 10.1038/s43017-021-00168-6.

Kumagai, I., Davaille, A., Kurita, K. and Stutzmann, E. (2008) 'Mantle plumes: Thin, fat, successful, or failing? Constraints to explain hot spot volcanism through time and space', *Geophysical Research Letters*, 35(16), pp. 1–5. doi: 10.1029/2008GL035079.

Lambart, S., Koornneef, J. M., Millet, M. A., Davies, G. R., Cook, M., Lissenberg, C. J. (2019) 'Highly heterogeneous depleted mantle recorded in the lower oceanic crust', *Nature Geoscience*. Springer US, 12(6), pp. 482–486. doi: 10.1038/s41561-019-0368-9.

Lessing, P. and Catanzero, E. J. (1964) '$^{87}Sr/^{86}Sr$ Ratios in Hawaiian Lavas', *Journal of Geophysical Research*, 69(8), pp. 1599–1601. doi: 10.1029/JZ069i008p01599.

Lessing, P., Decker, W. and Reynolds, R. C. (1963) 'Potassium and Rubidium Distribution in Hawaiian Lavas', *Journal of Geophysical Research*, 68(20), pp. 5851–5855. doi: 10.1029/JZ068i020p05851.

Lin, S. C. and Van Keken, P. E. (2005) 'Multiple volcanic episodes of flood basalts caused by thermochemical mantle plumes', *Nature*, 436(7048), pp. 250–252. doi: 10.1038/nature03697.

Lissenberg, C. J., MacLeod, C. J., Howard, K. A. and Godard, M. (2013) 'Pervasive reactive melt migration through fast-spreading lower oceanic crust (Hess Deep, equatorial Pacific Ocean)', *Earth and Planetary Science Letters*. Elsevier, 361, pp. 436–447. doi: 10.1016/j.epsl.2012.11.012.

Lissenberg, C. J. and Dick, H. J. B. (2008) 'Melt-rock reaction in the lower oceanic crust and its implications for the genesis of mid-ocean ridge basalt', *Earth and Planetary Science Letters*, 271(1–4), pp. 311–325. doi: 10.1016/j.epsl.2008.04.023.

Lissenberg, C. J. and MacLeod, C. J. (2016) 'A reactive porous flow control on mid-ocean ridge magmatic evolution', *Journal of Petrology*, 57(11–12), pp. 2195–2220. doi:

10.1093/petrology/egw074.

Loocke, M. P. (2016) *The role of the axial melt lens in crustal accretion at fast-spreading mid-ocean ridges.* PhD Thesis, Cardiff (Wales): Cardiff University.

Lubbers, J., Kent, A. J. R. and Russo, C. J. (2021) *LaserTRAM-DB : A Time Resolved Analysis Module for the complete reduction of Laser Ablation Inductively Coupled Plasma Mass Spectrometry data This paper is a non peer-reviewed preprint submitted to EarthArXiv . Future version of this paper may contain sli*. doi: 10.31223/X5QG95.

Macdonald, G. A. (1968) 'Composition and origin of Hawaiian lavas', *Geological Society of America Memoir*, 116, pp. 477–522. doi: 10.1130/MEM116-p477.

Maxim D. Ballmer, Lina Schumacher, Vedran Lekic, Christine Thomas, and G. I. (2016) 'Compositional layering within the large low shear-wave velocity provinces in the lower mantle', *Geochemistry Geophysics Geosystems*, 17(12), pp. 5056–5077.

McDonough, W. F. and Sun, S. s. (1995) 'The composition of the Earth', *Chemical Geology*, 120(3–4), pp. 223–253. doi: 10.1016/0009-2541(94)00140-4.

McKenzie, D. and O'Nions, R. K. (1983) 'Mantle reservoirs and ocean island basalts', *Nature*, 301(5897), pp. 229–231. doi: 10.1038/301229a0.

McNamara, A. K., Garnero, E. J. and Rost, S. (2010) 'Tracking deep mantle reservoirs with ultra-low velocity zones', *Earth and Planetary Science Letters*. Elsevier B.V., 299(1–2), pp. 1–9. doi: 10.1016/j.epsl.2010.07.042.

Montelli, R., Nolet, G., Dahlen, F. A., Masters, G., Engdahl, E. R. and Hung, S.-H. (2004) 'Finite-Frequency Tomography Reveals a Variety of Plumes in the Mantle', *Science*, 303(5656), pp. 338–343. doi: 10.1126/science.1092485.

Moore, J. G. and Clague, D. (1987) 'Coastal lava flows from Mauna Loa and Hualalai volcanoes, Kona, Hawaii', *Bulletin of Volcanology*, 49, pp. 752–764. doi: 10.1007/BF01079826.

Moore, J. G., Clague, D. A. and Normark, W. R. (1982) 'Diverse basalt types from Loihi seamount, Hawaii.', *Geology*, 10(2), pp. 88–92. doi: 10.1130/0091-7613(1982)10<88:DBTFLS>2.0.CO;2.

Moore, R. B., Clague, D., Rubin, M. and Bohrson, W. A. (1987) 'Hualalai-Volcano : a preliminary summary of geologic , petrologic , geophysical data', *US Geological Survey Profressional Paper*, 1350, pp. 571–585.

Morgan, W. J. (1971) 'Convection plumes in the lower mantle', *Nature*, 230(5288), pp. 42–43. doi: 10.1038/230042a0.

Morgan, W. J. (1972) 'Plate motions and deep mantle convection', *Memoir of the Geological Society of America*, 132(3), pp. 7–22. doi: 10.1130/MEM132-p7.

Nobre Silva, I. G., Weis, D. and Scoates, J. S. (2013) 'Isotopic systematics of the early Mauna Kea shield phase and insight into the deep mantle beneath the Pacific Ocean', *Geochemistry, Geophysics, Geosystems*, 14(3), pp. 659–676. doi: 10.1002/ggge.20047.

Norman, M. D. and Garcia, M. O. (1999) 'Primitive magmas and source characteristics of the Hawaiian plume : petrology and geochemistry of shield picrites', *Earth and Planetary Science Letters*, 168, pp. 27–44. doi: 10.1016/S0012-821X(99)00043-6.

O'Nions, R. K., Hamilton, P. J. and Evensen, N. M. (1977) 'Variations in $^{143}Nd/^{144}Nd$ and $^{87}Sr/^{S6}Sr$ ratios in oceanic basalts', *Earth and Planetary Science Letters*, 34, pp. 13–22. doi: 10.1016/0012-821X(77)90100-5.

Olson, P. (1990) 'Hot spots, swells and mantle plumes', *Magma Transport and Storage*, pp. 33–51.

Van Orman, J., Grove, T. and Shimizu, N. (2001) 'Rare earth element diffusion in diopside: Influence of temperature, pressure, and ionic radius, and an elastic model fordiffusion in silicates', *Contributions to Mineralogy and Petrology*, 141(6), pp. 687–703. doi: 10.1007/s004100100269.

Peterson, D.W., and Moore, R. B. (1987) 'Geologic history and evolution of geologic concepts, Island of Hawaii', *chap. 7 of Decker, R.W., Wright, T.L., and Stauffer, P.H., eds., Volcanism in Hawaii: U.S. Geological Survey Professional Paper 1350*, 1, pp. 149–189. Available at: http://pubs.usgs.gov/pp/1987/1350/.

Pickett, D. A. and Murrell, M. T. (1997) 'Observations of 231 Pa / 235U disequilibrium in volcanic rocks', *Earth and Planetary Science Letters*, 148, pp. 259–271. doi: 10.1016/S0012-

821X(97)00037-X.

Piggot, C. S. (1931) ‘Radium in rocks: iii. The radium content of Hawaiian lavas', *The American Journal of Science 5th Series*, 22, pp. 1–8. doi: 10.2475/ajs.s5-22.127.1.

Plank, T. and Langmuir, C. H. (1998) ‘The chemical composition of subducting sediment and its consequences for the crust and mantle’, *Chemical Geology*, 145(3–4), pp. 325–394. doi: 10.1016/S0009-2541(97)00150-2.

Powell, J. L., Faure, G. and Hurley, P. M. (1965) ‘Strontium 87 Abundance in a Suite of Hawaiian Volcanic Rocks of Varying Silica Content’, *Journal of Geophysical Research*, 70(6), pp. 1509–1513. doi: 10.1029/JZ070i006p01509.

Rhodes, J. M., Dungan, M. A., Blanchard, D. P. and Long, P. E. (1979) ‘Magma mixing at mid-ocean ridges: Evidence from basalts drilled near 22° N on the Mid-Atlantic Ridge’, *Tectonophysics*, 55(1–2), pp. 35–61. doi: 10.1016/0040-1951(79)90334-2.

Richards, M. A., Duncan, R. A. and Courtillot, V. E. (1989) ‘Flood basalts and hot-spot tracks: Plume heads and tails’, *Science*, 246(4926), pp. 103–107. doi: 10.1126/science.246.4926.103.

Rudnick, R. L. and Gao, S. (2003) ‘Composition of the Continental Crust. In Rudnick, R.L. (Eds), The Crust’, *Treatise on geochemistry*, 3, pp. 1–64.

Ryan, M. P., Koyanagi, R. K. and Fiske, R. S. (1981) ‘Modeling the three-dimensional structure of macroscopic transport systems: application to Kilauea volcano, Hawaii.’, *Journal of Geophysical Research*, 86(B8), pp. 7111–7129. doi: 10.1029/JB086iB08p07111.

Samuel, H. and Bercovici, D. (2006) ‘Oscillating and stagnating plumes in the Earth’s lower mantle’, *Earth and Planetary Science Letters*, 248(1–2), pp. 90–105. doi: 10.1016/j.epsl.2006.04.037.

Schilling, J.-G. (1973) ‘Iceland mantle plume: geochemical evidence along Reykjanes Ridge’, *Nature*, 242(5400), pp. 565–571. Available at: https://www.nature.com/articles/242565a0.

Schilling, J.-G. and Winchester, J. W. (1969) ‘Rare Earth Contribution to the Origin of Hawaiian Lavas’, *Contr. Mineral. and Petrol.*, 23, pp. 27–37. doi: 10.1007/BF00371330.

Shannon, R. D. (1976) ‘Revised Effective Ionic Radii and Systematic Studies of Interatomie Distances in Halides and Chaleogenides’, *Acta Crystallographica*, 32, pp. 751–767.

Sharp, W. D. and Clague, D. A. (2006) '50-Ma Initiation of Hawaiian-Emperor Bend Records Major Change in Pacific Plate Motion', *Science*, 313(5791), pp. 1281–1284.

Shea, T., Leonhardi, T., Giachetti, T., Lindoo, A., Larsen, J., Sinton, J. and Parsons, E. (2017) 'Dynamics of an unusual cone-building trachyte eruption at Pu'u Wa'awa'a , Hualālai volcano , Hawai'i', *Bulletin of Volcanology*. Bulletin of Volcanology, 79(26), pp. 1–24. doi: 10.1007/s00445-017-1106-z.

Sims, K. W. W., Depaolo, D. J., Murrell, M. T., Baldridge, W. S., Goldstein, J. S. and Clague, D. A. (1995) 'Mechanisms of Magma Generation Beneath Hawaii and Mid-Ocean Ridges: Uranium/Thorium and Samarium/Neodymium Isotopic Evidence', *Science*, 276, pp. 508–512. doi: 10.1126/science.267.5197.508.

Sims, K. W. W., DePaolo, D. J., Murrell, M. T., Baldridge, W. S., Goldstein, S., Clague, D. and Jull, M. (1999) 'Porosity of the melting zone and variations in the solid mantle upwelling rate beneath Hawaii: Inferences from 238U-230Th-226Ra and 235U-231Pa disequilibria', *Geochimica et Cosmochimica Acta*, 63(23), pp. 4119–4138.

Sims, K. W. W. and Depaolo, D. J. (1997) 'Inferences about mantle magma sources from incompatible element concentration ratios in oceanic basalts', *Geochimica et Cosmochimica Acta*, 61(4), pp. 765–784. doi: 10.1016/S0016-7037(96)00372-9.

Sleep, N. H. (1990) 'Hotspots and mantle plumes: some phenomenology', *Journal of Geophysical Research*, 95(B5), pp. 6715–6736. doi: 10.1029/JB095iB05p06715.

Sobolev, A. V and Nikogosian, I. (1994) 'Petrology of long-lived mantle plume magmatism : Hawaii , Pacific and Reunion Island , Indian Ocean', 2(2), pp. 111–144.

Somayajulu, B. L. K., Tatsumoto, M., Rosholt, J. N. and Knight, R. J. (1966) 'Disequilibrium of the ^{238}U series in basalt', *Earth and Planetary Science Letters I*, pp. 387–391.

Stracke, A., Salters, V. J. M. and Sims, K. W. W. (1999) 'Assessing the presence of garnet-pyroxenite in the mantle sources of basalts through combined hafnium-neodymiumthorium isotope systematics', *Geochemistry Geophysics Geosystems*, 1(1), pp. 1–13. doi: 10.1029/1999GC000013.

Sun, C., Graff, M. and Liang, Y. (2017) 'Trace element partitioning between plagioclase and

silicate melt: The importance of temperature and plagioclase composition, with implications for terrestrial and lunar magmatism', *Geochimica et Cosmochimica Acta*. Elsevier Ltd, 206, pp. 273–295. doi: 10.1016/j.gca.2017.03.003.

Sun, C. and Liang, Y. (2012) 'Distribution of REE between clinopyroxene and basaltic melt along a mantle adiabat: Effects of major element composition, water, and temperature', *Contributions to Mineralogy and Petrology*, 163(5), pp. 807–823. doi: 10.1007/s00410-011-0700-x.

Sun, S. S. and McDonough, W. F. (1989) 'Chemical and isotopic systematics of oceanic basalts: Implications for mantle composition and processes', *Geological Society Special Publication*, 42(1), pp. 313–345. doi: 10.1144/GSL.SP.1989.042.01.19.

Tanaka, E., Nakamura, R. and Takahashi, E. (2002) 'Geochemical Evolution of Koolau Volcano, Hawaii', *Geophysical Monograph Series*, 128, pp. 311–332.

Tanaka, R., Makishima, A. and Nakamura, E. (2008) 'Hawaiian double volcanic chain triggered by an episodic involvement of recycled material: Constraints from temporal Sr-Nd-Hf-Pb isotopic trend of the Loa-type volcanoes', *Earth and Planetary Science Letters*. Elsevier B.V., 265(3–4), pp. 450–465. doi: 10.1016/j.epsl.2007.10.035.

Tanaka, R. and Nakamura, E. (2005) 'Boron isotopic constraints on the source of Hawaiian shield lavas', *Geochimica et Cosmochimica Acta*, 69(13), pp. 3385–3399. doi: 10.1016/j.gca.2005.03.009.

Tatsumoto, M. (1966) 'Isotopic Composition of Lead in Volcanic Rocks from Hawaii , Iwo Jima , and Japan', *Journal of Geophysical Research*, 71(6), pp. 1721–1733.

Tatsumoto, M. (1978) 'Isotopic composition of lead in oceanic basalt and its implication to mantle evolution', *Earth and Planetary Science Letters*, 38(1), pp. 63–87. Available at: https://www.sciencedirect.com/science/article/pii/0012821X78901267?via%3Dihub.

Thorne, M. S., Garnero, E. J. and Grand, S. P. (2004) 'Geographic correlation between hot spots and deep mantle lateral shear-wave velocity gradients', *Physics of the Earth and Planetary Interiors*, 146(1–2), pp. 47–63. doi: 10.1016/j.pepi.2003.09.026.

Wang, X., Hou, T., Wang, M., Zhang, C., Zhang, Z., Pan, R., Marxer, F. and Zhang, H. (2021) 'A

new clinopyroxene thermobarometer for mafic to intermediate magmatic systems', *European Journal of Mineralogy*, 33(5), pp. 621-637.

Washington, H. S. and Keyes, M. G. (1928) 'Petrology of the Hawaiian islands. IV. Maui', *American Journal of Science 5th Series*, 15, pp. 199–220.

Washington, H. S. (1923) 'Petrology of the Hawaiian islands. II. Hualalai and Mauna Loa', *American Journal of Science 5th Series*, 6, pp. 100–126.

Weis, D., Garcia, M. O., Rhodes, J. M. and Jellinek, M. (2011) 'Role of the deep mantle in generating the compositional asymmetry of the Hawaiian mantle plume', *Nature Geoscience*, 4(12), pp. 831–838. doi: 10.1038/ngeo1328.

White, W. M. (2010) 'Oceanic Island basalts and mantle plumes: The geochemical perspective', *Annual Review of Earth and Planetary Sciences*, 38, pp. 133–160. doi: 10.1146/annurev-earth-040809-152450.

Whitehead, J. A. and Luther, D. S. (1975) 'Dynamics of laboratory diapir and plume models', *Journal of Geophysical Research*, 80(5), pp. 705–717. doi: 10.1029/jb080i005p00705.

Wieser, P. E., Edmonds, M., Gansecki, C., Maclennan, J., Jenner, F. E., Kunz, B., Antoshechkina, P., Trusdell, F., Lee, R. L. and EIMF (2022) 'Explosive Activity on Kīlauea's Lower East Rift Zone Fueled by a Volatile-Rich, Dacitic Melt', *Geochemistry, Geophysics, Geosystems*, 23(2), pp. 1–24. doi: 10.1029/2021GC010046.

Wieser, P., Petrelli, M., Lubbers, J., Wieser, E., Ozaydin, S., Kent, A. and Till, C. (2022) 'Thermobar: An open-source Python3 tool for thermobarometry and hygrometry', *Volcanica*, 5(2), pp. 349-384. doi: 10.30909/vol.05.02.349384

Willbold, M. and Stracke, A. (2006) 'Trace element composition of mantle end-members: Implications for recycling of oceanic and upper and lower continental crust', *Geochemistry, Geophysics, Geosystems*, 7(4), pp. 1–30. doi: 10.1029/2005GC001005.

Willbold, M. and Stracke, A. (2010) 'Formation of enriched mantle components by recycling of upper and lower continental crust', *Chemical Geology*. Elsevier B.V., 276(3–4), pp. 188–197. doi: 10.1016/j.chemgeo.2010.06.005.

Williams, C. D., Mukhopadhyay, S., Rudolph, M. L. and Romanowicz, B. (2019) 'Primitive

Helium Is Sourced From Seismically Slow Regions in the Lowermost Mantle', *Geochemistry, Geophysics, Geosystems*, 20(8), pp. 4130–4145. doi: 10.1029/2019GC008437.

Williams, Q. and Garnero, E. J. (1996) 'Seismic evidence for partial melt at the base of earth's mantle', *Science*, 273(5281), pp. 1528–1530. doi: 10.1126/science.273.5281.1528.

Williams, Q., Revenaugh, J. and Garnero, E. (1998) 'A correlation between ultra-low basal velocities in the mantle and hot spots', *Science*, 281(5376), pp. 546–549. doi: 10.1126/science.281.5376.546.

Williamson, N. M. B., Weis, D., Scoates, D. W., Pelletier, H. and Garcia, M. O. (2019) 'Tracking the Geochemical Transition Between the Kea-Dominated Northwest Hawaiian Ridge and the Bilateral Loa-Kea Trends of the Hawaiian Islands', *Geochemistry Geophysics Geosystems*, 20, pp. 4354–4369. doi: 10.1029/2019GC008451.

Wolfe, E. and Morris, J. (1996) *Geologic map of the Island of Hawaii*, *U.S. Geological Survey Miscellaneous Investigations Series Map I–2524–A*. doi: 10.3133/i2524A.

Yang, J., Wang, C., ZHang, J. and Jin, J. Z. (2023) 'Genesis of Hawaiian lavas by crystallization of picritic magma in the deep mantle', *Nature Communications*, 14(1382), pp. 1-8.

Zhang, W. and Hu, Z. (2020) 'Estimation of Isotopic Reference Values for Pure Materials and Geological Reference Materials', Atomic Spectroscopy, 41(3), pp. 93-102. doi: 10.46770/AS.2020.03.001

Zindler, A. and Hart, S. (1986) 'Chemical geodynamics.', *Annual review of Earth and planetary sciences. Vol. 14*, (c), pp. 493–571. doi: 10.1146/annurev.ea.14.050186.002425.

8. Appendices

Appendices can be found in the adjoining Excel document 'Appendices_LECOEUCHE_Camille_0922'.

8.1 SEM Clinopyroxenes

The sheet named ‘1. SEM Clinopyroxenes’ in the appendices displays the major element data collected for sampled clinopyroxene crystals, and the calculated Mg# value for each sampled area.

8.2 SEM Plagioclase

The sheet named ‘2. SEM Plagioclase’ in the appendices displays the major element data collected for sampled plagioclase crystals, and the calculated anorthite content for each sampled area.

8.3 SEM Standards

The sheet named ‘3. SEM Standards’ in the appendices displays the major element data collected for sampled standards. An average value and standard deviation was calculated for each standard in each run.

8.4 SEM Precision & Accuracy

The sheet named ‘4. SEM Prec. & Acc.’ in the appendices displays the calculated precision and accuracy of the average values of a given standard for a given run.

8.5 Diopside &Plagioclase Precision & Accuracy

The sheet named ‘5. P&A Diop&Plag’ in the appendices displays the calculated percentage precision and accuracy of the average values of the Astimex Diopside and Plagioclase standards for each given run.

8.6 Laser Ablation Clinopyroxene

The sheet named ‘6. LA Clinopyroxene’ in the appendices displays the trace element data from sampled clinopyroxene locations. Trace element concentrations have also been normalised to the primitive mantle (McDonough and Sun, 1995).

8.7 Laser Ablation Clinopyroxene Normalised

The sheet named ‘7. LA CPX Ratios’ in the appendices displays the mantle normalised trace element data (McDonough and Sun, 1995) from sampled clinopyroxene locations. Trace element ratios (Ce/Y and La/Sm) have also been calculated.

8.8 Laser Ablation Clinopyroxene Precision & Accuracy

The sheet named ‘8. La (CPX) P&A’ in the appendices displays the calculated precision and accuracy of trace element data from analysed standards (USGS glass standards GSD-1G (Jochum *et al.*, 2011), BHVO-2G and BCR-2G (Jochum *et al.*, 2010), MPI-DING reference glasses KL2-G, StHs6/80-G, T1-G, and ATHO-G (Jochum *et al.*, 2011) and NIST SRM glasses NIST SRM 610 and NIST SRM 612 (Jochum *et al.*, 2011)). Data reduction was done in LaserTRAM-DB (Lubbers, Kent and Russo, 2021) using ^{43}Ca (from EDS analysis) as the internal reference standard, and USGS glass standard BCR-2G (Jochum *et al.*, 2010) as the standard reference material. This data reduction was used for clinopyroxene data.

8.9 NIST SRM 612 Precision & Accuracy

The sheet named ‘9. NIST SRM 612 P&A’ in the appendices displays the calculated percentage precision and accuracy of trace element data from analysed standard NIST SRM 612 (Jochum *et al.*, 2011) for laser ablation data reduction in LaserTRAM-DB (Lubbers, Kent and Russo, 2021) using ^{43}Ca (from EDS analysis) as the internal reference standard, and USGS glass standard BCR-2G (Jochum *et al.*, 2010) as the standard reference material. This data reduction was used for clinopyroxene data.

8.10 Laser Ablation Plagioclase

The sheet named ‘10. LA Plagioclase’ in the appendices displays the trace element data from sampled plagioclase locations. Trace element concentrations have also been normalised to the primitive mantle (McDonough and Sun, 1995).

8.11 Laser Ablation Plagioclase Normalised

The sheet named ‘11. LA PLG Norm.’ in the appendices displays the mantle normalised (McDonough and Sun, 1995) trace element data from sampled plagioclase locations. Data

for elements highlighted in red were not used for the run 'November Run3' (including sample 101863 locations 9, 10, 11 and 12 and sample 81869 locations 1 and 2).

8.12 Laser Ablation Plagioclase Precision & Accuracy

The sheet named '12. LA (PLG) P&A' in the appendices displays the calculated precision and accuracy of trace element data from analysed standards (USGS glass standards GSD-1G (Jochum *et al.*, 2011), BHVO-2G and BCR-2G (Jochum *et al.*, 2010), MPI-DING reference glasses KL2-G, StHs6/80-G, T1-G, and ATHO-G (Jochum *et al.*, 2011) and NIST SRM glasses NIST SRM 610 and NIST SRM 612 (Jochum *et al.*, 2011)). Data reduction was done in LaserTRAM-DB (Lubbers, Kent and Russo, 2021) using ^{43}Ca (from EDS analysis) as the internal reference standard, and NIST SRM 612 (Jochum *et al.*, 2011) as the standard reference material. This data reduction was used for plagioclase data.

8.13 BCR-2G Precision & Accuracy

The sheet named '13. BCR-2G P&A' in the appendices displays the calculated percentage precision and accuracy of trace element data from analysed USGS glass standard BCR-2G (Jochum *et al.*, 2010) for laser ablation data reduction in LaserTRAM-DB (Lubbers, Kent and Russo, 2021) using ^{43}Ca (from EDS analysis) as the internal reference standard, and USGS glass standard BCR-2G (Jochum *et al.*, 2010) as the standard reference material. This data reduction was used for plagioclase data.

8.14 Temperature & Pressure

The sheet named '14. T & P' in the appendices displays the calculated temperatures and pressures of crystal formation for each sampled location (Gleeson, Lissenberg and Lecoeuche, Unpublished Data).

8.15 Clinopyroxene Bedard Partition Coefficient

The sheet named '15. CPX Bedard Partition Coef.' in the appendices displays the partition coefficients calculated for clinopyroxene data using work by Bédard (2014).

8.16 Clinopyroxene Bedard Cmelt

The sheet named ‘16. CPX Bedard Cmelt’ in the appendices displays the equilibrium melt compositions corresponding to each sampled location calculated from clinopyroxene data using the partition coefficients calculated using work by Bédard (2014).

8.17 Clinopyroxene Sun Partition Coefficient

The sheet named ‘17. CPX Sun Partition Coef.’ in the appendices displays the partition coefficients calculated for clinopyroxene data using work done by Sun and Liang (2012), Hill, Blundy and Wood (2011, 2012) and Shannon (1976).

8.18 Clinopyroxene Sun Cmelt

The sheet named ‘18. CPX Sun Cmelt’ in the appendices displays the equilibrium melt compositions corresponding to each sampled location calculated from clinopyroxene data using the partition coefficients calculated using work done by Sun and Liang (2012), Hill, Blundy and Wood (2011, 2012) and Shannon (1976).

8.19 Plagioclase Bedard Partition Coefficient

The sheet named ‘19. PLG Bedard Partition Coef.’ in the appendices displays the partition coefficients calculated for plagioclase data using work by Bédard (2006).

8.20 Plagioclase Bedard Cmelt

The sheet named ‘20. PLG Bedard Cmelt’ in the appendices displays the equilibrium melt compositions corresponding to each sampled location calculated from plagioclase data using the partition coefficients calculated using work by Bédard (2006). Data for elements highlighted in red were not used for the run ‘November Run3’ (including sample 101863 locations 9, 10, 11 and 12 and sample 81869 locations 1 and 2).

8.21 Plagioclase Sun Partition Coefficient

The sheet named ‘21. PLG Sun Partition Coef.’ in the appendices displays the partition coefficients calculated for plagioclase data using work done by Shannon (1976) and Sun, Graff and Liang (2017).

8.22 Plagioclase Sun Cmelt

The sheet named '22. PLG Sun Cmelt' in the appendices displays the equilibrium melt compositions corresponding to each sampled location calculated from plagioclase data using the partition coefficients calculated using work done by Shannon (1976) and Sun, Graff and Liang (2017). Data for elements highlighted in red were not used for the run 'November Run3' (including sample 101863 locations 9, 10, 11 and 12 and sample 81869 locations 1 and 2).

8.23 Sr Isotopic Data

The sheet named '23. Sr' in the appendices displays $^{87}Sr/^{86}Sr$ isotopic data for sampled locations and the internal precision of each data point (2se).

8.24 Major Element model

The sheet named '24. Major Element Model' in the appendices displays the MELTS (Gualda *et al.*, 2012) clinopyroxene output used to make the modelled major element path of fractional crystallisation or clinopyroxene crystals (solid line of descent) at 0.5 wt% H_2O and 5kbar.

8.25 Trace Element Model Solid Line of Descent

The sheet named '25. Trace Element Model SLD' in the appendices displays the data calculated using the MELTS (Gualda *et al.*, 2012) output which was then used to make the modelled trace element path of fractional crystallisation of clinopyroxene crystals (solid line of descent) at 0.5 wt% H_2O and 5kbar.

8.26 Trace Element Model Liquid Line of Descent

The sheet named '26. Trace Element Model LLD' in the appendices displays the data calculated using the MELTS (Gualda *et al.*, 2012) output which was then used to make the modelled trace element path of fractional crystallisation of equilibrium melts (liquid line of descent) at 0.5 wt% H_2O and 5kbar.

8.27 GEOROC Data

The sheet named '27. GEOROC' in the appendices displays the published volcanic whole rock (VWR) data from Hualalai downloaded from the GEOROC database (https://georoc.eu/) on 6 October 2021, using the following parameters: geographical location = Hualalai; Hawaii: rock type = volcanic. The basaltic and trachytic post-shield data and shield picrite data found on GEOROC used in this project was compiled from published data (Washington, 1923; Washington and Keyes, 1928; Piggot, 1931; Lessing et al., 1963; Lessing and Catanzero, 1964; Powell et al., 1965; Hamilton, 1965; Somayajulu et al., 1966; Tatsumoto, 1966; Macdonald, 1968; Funkhouser et al., 1968; Schilling and Winchester, 1969; O'Nions et al., 1977; Anonymous, 1980; Clague et al., 1980; Moore and Clague, 1987; Moore et al., 1987; Clague, 1987; Clague and Bohrson, 1991; Sobolev and Nikogosian, 1994; Sims et al., 1995; Pickett and Murrell, 1997; Sims and Depaolo, 1997; Norman and Garcia, 1999; Sims et al., 1999; Stracke et al., 1999; Cousens et al., 2003; Hanano et al., 2010; Shea et al., 2017). Trace element data was normalised to the primitive mantle (McDonough and Sun, 1995).

8.28 Zone Refining Trend

The sheet named '28. Zone Refining Trend' in the appendices displays the calculated data for the zone refining trend used to model the direction of crystal dissolution-reaction using the equation from Harris (1957):

$$\frac{C_L}{C_0} = \frac{1}{D} - \left(\frac{1}{D} - 1\right) e^{(-DI)}$$

where C_L represents the concentration of an element in the liquid after zone refining, C_0 represents the initial concentration of the element in the liquid, D is the partition coefficient, and I is the number of reactive flow cycles modelled (Johan, 2016). The initial concentration of each element was taken from the trace element composition of sample 02AHU-4 (from Hanano et al. (2010)), normalised to the primitive mantle. The D values used were the bulk partition coefficients of the total cumulate for each element at 1201°C calculated using Bedard (2001). I was varied from 0 to 2.38 in increments of 0.01.